The Dissertation Committee for Eric James Titus Certifies that this is the approved version of the following dissertation:

Sub-Diffraction Limited Imaging of Plasmonic Nanostructures

Committee:

Katherine A. Willets, Supervisor

Brian A. Korgel

Xiaoqin Li

C. Buddie Mullins

David A. Vanden Bout

Sub-Diffraction Limited Imaging of Plasmonic Nanostructures

by

Eric James Titus, B.S.

Dissertation

Presented to the Faculty of the Graduate School of

The University of Texas at Austin

in Partial Fulfillment

of the Requirements

for the Degree of

Doctor of Philosophy

The University of Texas at Austin

August 2014

Acknowledgements

First, I would like to acknowledge my family, especially my parents, Jim and Kathy, for all of their support through the years. You both started me on this path many years ago through all of the science books and activities as a kid, and followed-through by taking any opportunity that you could to nurture my interest in science and support my academic pursuits. Thank you.

I also want to thank Professor Kallie Willets for all of her guidance through the past 5 years. I've really enjoyed the research that I've done with you in the lab, and the quality and style of your mentoring has contributed significantly to my enjoyment of science, as well as my growth as a scientist. I would also like to give special thanks to Dr. Ifat Kaplan-Ashiri for mentoring me through my early years in the group. Additionally, I want to thank the entire "Hole in the Wall crew", from both the Willets lab and others, that helped keep me sane over the past several years.

Finally, I want to extend a special thank you to Karole Blythe for her companionship and support in both life and in research during this process. I am so happy to be able to share this time with you.

Sub-Diffraction Limited Imaging of Plasmonic Nanostructures

Eric James Titus, PhD

The University of Texas at Austin, 2014

Supervisor: Katherine A. Willets

This thesis is focused on understanding the interactions between molecules and surface-enhanced Raman scattering (SERS) substrates that are typically unresolved due to the diffraction limit of light. Towards this end, we have developed and tested several different sub-diffraction-limited imaging techniques in order to observe these interactions. First, we utilize an isotope-edited bianalyte approach combined with super-resolution imaging *via* Gaussian point-spread function fitting to elucidate the role of Raman reporter molecules on the location of the SERS emission centroids. By using low concentrations of two different analyte molecules, we find that the location of the SERS emission centroid depends on the number and positions of the molecules present on the SERS substrate.

It is also known that SERS enhancement partially results from the molecule coupling its emission into the far-field through the plasmonic nanostructure. This results in a particle-dictated, dipole-like emission pattern, which cannot be accurately modeled as a Gaussian, so we tested the applicability of super-resolution imaging using a dipole-emission fitting model to this data. To test this model, we first fit gold nanorod (AuNR) luminescence images, as AuNR luminescence is primarily coupled out through the longitudinal dipole plasmon mode. This study showed that a three-dimensional dipole model is necessary to fit the AuNR emission, with the model providing accurate orientation and emission wavelength parameters for the nanostructure, as confirmed using correlated AFM and spectroscopy. The dipole fitting technique was next applied to single- and multiple-molecule SERS emission from silver nanoparticle dimers. We again

found that a three-dimensional dipole PSF was necessary to accurately model the emission and orientation parameters of the dimer, but that at the single molecule level, the movement of the molecule causes increased uncertainty in the orientation parameters determined by the fit.

Finally, we describe progress towards using a combined atomic force/optical microscope system in order to position a carbon nanotube analyte at known locations on the nanoparticle substrate. This would allow for the simultaneous mapping of nanoparticle topography and exact locations of plasmonic enhancement around the nanostructure, but consistently low signal-to-noise kept this technique from being viable.

Table of Contents

List of Tables

List of Figures

Chapter 1: Introduction

1.1 Plasmons and Surface-enhanced Raman scattering (SERS)

Noble metal nanostructures have been long studied by many researchers due to their ability interact with and focus light.[1–4] This property is due to excitations of plasmon resonances, which are collective oscillations of surface conduction electrons, and can be excited at optical frequencies in structures with a negative real and small positive imaginary dielectric function, as shown in Figure 1.1 below for a noble metal nanoparticle.[1] When this resonance occurs on a nanoparticle or nanoparticle aggregate, this is referred to as a localized surface plasmon resonance (LSPR). The scattering strength and resonance frequency of the LSPR is dependent on the size, shape and material of the nanoparticle.

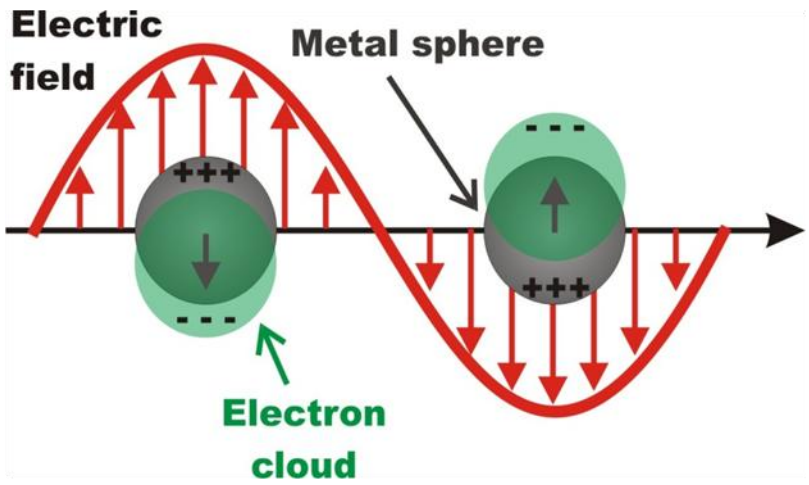

Figure 1.1. Diagram showing the electric field component of light exciting a localized surface plasmon (LSPR) on a single nanoparticle.

The LSPR causes the nanoparticle to scatter light efficiently at its resonance frequency, and also causes strongly enhanced electric fields at the nanoparticle surface.[3,5] These fields are evanescent in nature, and can be several orders of magnitude larger than

the electric field of the incident light. These properties can be taken advantage of in surface-enhanced spectroscopy techniques such as surface-enhanced Raman scattering (SERS). In SERS, molecules are adsorbed on to a nanostructured surface, such as a plasmonic nanoparticle, where the LSPR enhanced electric fields at the nanoparticle surface can provide enhanced optical excitation to the molecule.[4,6] Additionally, due to the strong scattering of the nanoparticle, Raman scattered light from the molecule can be further enhanced by coupling to LSPR modes of the nanoparticle.[7–9] Because of these unique optical properties, noble metal nanoparticles are now being investigated for uses in fields such as biosensing,[1,2] photothermal therapy,[10,11] and surface enhanced spectroscopies like SERS.[4,12]

1.2 Single-molecule surface-enhanced Raman scattering (SM-SERS)

For certain types of plasmonic nanostructures, *e.g.* silver nanoparticle (AgNP) aggregates, LSPR enhancement of Raman scattering can even be high enough to observe SERS from single molecules. Single-molecule SERS (SM-SERS) sensitivity was first reported in 1997, and has been primarily observed in silver colloidal nanoparticles, aggregated with a reporter dye such as Rhodamine 6G (R6G).[13–18] Through these initial studies, the strongest SERS enhancements were believed to originate from molecules in the junctions between nanoparticles in these aggregates, and these regions are known as SERS "hot spots", which are thought to be 1-10 nm in size.[8,19–21] Example atomic force microscopy (AFM) images of SM-SERS active silver nanoparticle aggregates can be seen below in Figure 1.2. Since the discovery of SM-SERS, there have been many efforts in the field to characterize the nature of these "hot spots" in order to expand this SM-SERS sensitivity to other systems of analytes and plasmonic nanostructures.

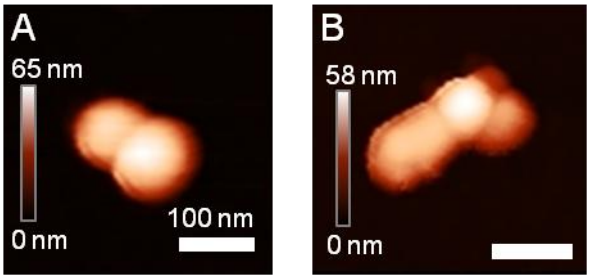

Figure 1.2. AFM images showing typical SM-SERS active colloidal silver aggregates. The particles shown have been aggregated with NaCl and R6G dye.

When undertaking research in the field of SM-SERS, one important aspect of any study is to confirm that SERS signals are indeed originating from single-molecules.[14,15] In order to do this, several different fundamental aspects of SERS can be used. One characteristic of SM-SERS (as well as SM-fluorescence) is the way that SM signals "turn-off" in a single step. An example of this behavior can be seen below in Figure 1.3. In this figure, a plot of integrated optical intensity of a SERS aggregate is shown, plotted against the image frame number (time). In this example, we can see that the SERS emission stops in a single digital step, possibly due to the molecule leaving the "hot spot".[13,16] The intensity *vs.* time plot in Figure 1.3 also shows the strong intensity fluctuations that are also characteristic of SM-SERS. Again, due to the small size of the "hot spot", movement of the molecule on the surface of the nanoparticle can cause these intensity fluctuations.

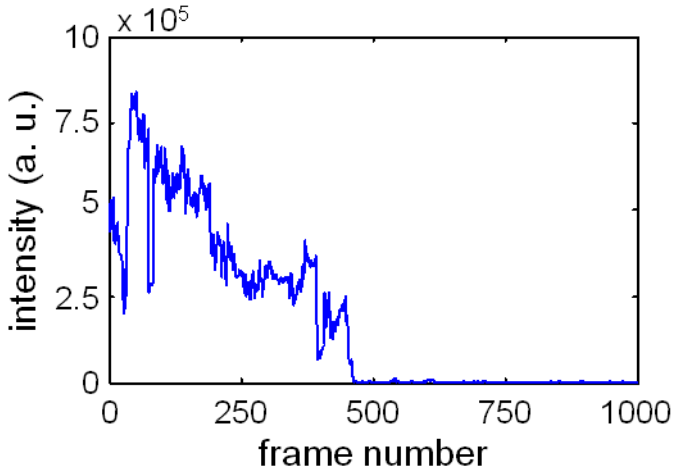

Figure 1.3. Integrated intensity vs. frame number, showing the intensity fluctuations present in SM-SERS, as well as a digital step from "on" to "off".

While SERS intensity fluctuations and digital on-off steps in intensity can provide strong evidence for SM-SERS, the isotope-edited bianalyte approach, developed by the Van Duyne group, has been generally accepted as the strongest proof of SM-SERS.[14,22] In this technique, equal amounts of two rhodamine 6G isotopologues are used, which can be distinguished based on certain Raman peak differences in their spectra, as shown in Figure 1.4. These dyes will have equal scattering cross-sections and probabilities of adsorbtion on to the nanoparticle structures, making them equally likely to adsorb to a SERS-active nanoparticle aggregate. By using a concentration of roughly one dye/nanoparticle, when only one species is observed in the emission from a nanoparticle aggregate, it is most probable that the emission is due to SERS from a single molecule.[14] This isotope-edited bianalyte approach is used to confirm the presence of SM-SERS in Chapters 3 and 5 of this work.

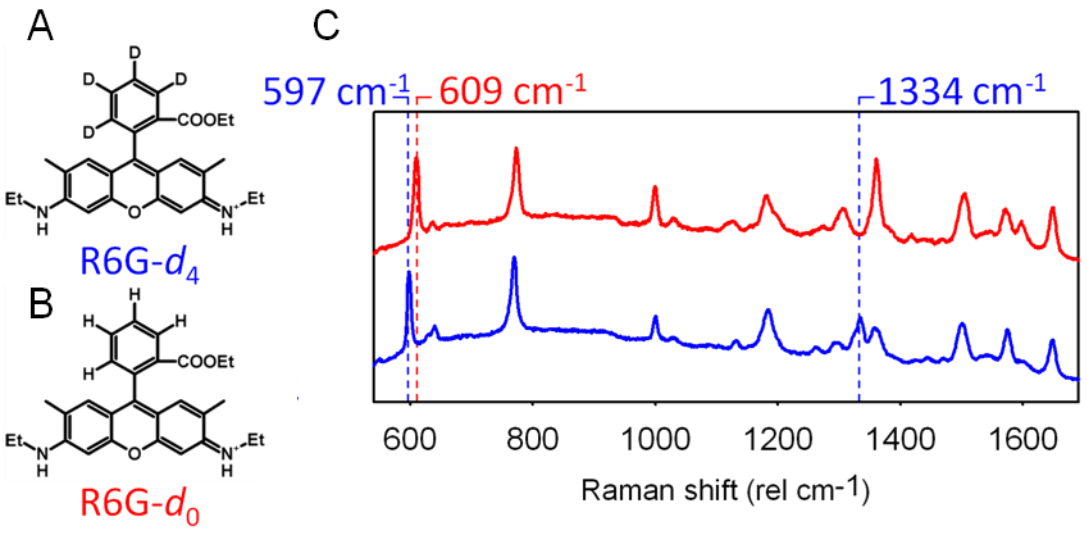

Figure 1.4. Molecular structures showing (A) R6G-*d4* and (B) R6G-*d0*. (C) Color coded SERS spectra of R6G-*d4* and R6G-*d0* with isotopologue marker modes indicated, taken on a Ag film-over-nanospheres (AgFONS). Adapted with permission from Titus, E. J.; Weber, M. L.; Stranahan, S. M.; Willets, K. A. Super-Resolution SERS Imaging beyond the Single-Molecule Limit: An Isotope-Edited Approach. *Nano Lett.* **2012**, *6*, 5103-5110. Copyright 2012 American Chemical Society.

1.3 Diffraction-limited imaging

One of the major problems in characterizing SM-SERS "hot spots" is due to the diffraction limit of light, which limits the optical resolution of optical microscopy systems to roughly half the wavelength of the imaged light. This means that when we use visible light to excite and study SM-SERS, our resolution is limited to roughly 200 nm, which is significantly larger than the size of a 1-10 nm "hot spot". This limit makes it difficult to extract spatial information about the nature of the "hot spot" with optical microscopy. To illustrate this, Figure 1.5 shows a size comparison of a diffraction-limited SM-SERS emission spot and the AFM image (not subject to the diffraction limit) of the SM-SERS active aggregate.

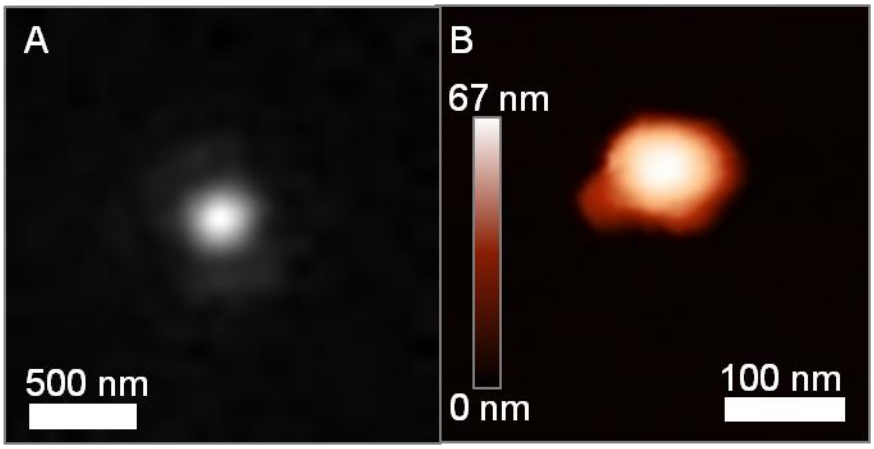

Figure 1.5. Diffraction-limited optical image (A) of SM-SERS emission from a nanoparticle aggregate, compared to its structure as determined *via* AFM (B).

1.4 Super-resolution imaging of SM-SERS "hot spots"

One technique that has recently been used to overcome the diffraction limit is super-resolution microscopy.[23–25] In this method, diffraction-limited images of point emitters, *e.g.* single fluorophores, are collected and then fit using a model point-spread function. For this purpose, a 2-dimensional Gaussian function is typically used, and has been shown to give a spatial resolution of <5 nm for well-isolated emitters.[25–27] The 2-dimensional Gaussian equation that is typically used is shown below in Equation 1.1.

$$I(x,y) = z_0 + I_0 e^{\left[-\frac{1}{2}\left[\left(\frac{x-x_0}{s_x}\right)^2 + \left(\frac{y-y_0}{s_y}\right)^2\right]\right]} \qquad (1.1)$$

In this equation, the spatially dependent intensity of the diffraction-limited spot, *I(x,y,)* is dependent on the background intensity, z_0; the peak emission intensity of the spot, I_0; the centroid positions x_0 and y_0; and the width of the emission spot in both dimensions, s_x and s_y. After fitting each diffraction-limited spot with Equation 1.1, the centroid positions for

each emission spot are extracted to give the diffraction-limited localization of the emission.

While super-resolution imaging was originally developed for single-molecule fluorescence, it has been recently applied to plasmonic nanostructures to track nanoparticle motion,[28–32] study ligand binding,[33,34] follow catalytic processes in real time,[35] and map SERS "hot spots".[13,36–38] In the SERS "hot spot" mapping studies, super-resolution imaging was used to localize and track the SM-SERS emission centroid in samples comprised of aggregated AgNPs and R6G dye molecules.[13,39] The data collected using this technique was then correlated to nanoparticle structure using scanning electron microscopy (SEM) to compare SERS centroid movements to the AgNP aggregate structure, as shown below in Figure 1.6.[36,37] In this figure, the SERS centroid position and intensity is compared to the AgNP aggregate structure. The super-resolution SERS optical data is represented using a spatial intensity map, in which the SERS centroids are binned spatially and are colored based on the average emission intensity captured within each bin.[13] When this optical data is overlaid with the SEM data of the same aggregate, it can be seen that the trajectory of the SERS centroid matches the orientation of one of the aggregate junction regions very closely, which agrees with previous experimental and theoretical data indicating that the strongest SERS enhancements occur at the junction regions in these aggregates.[36]

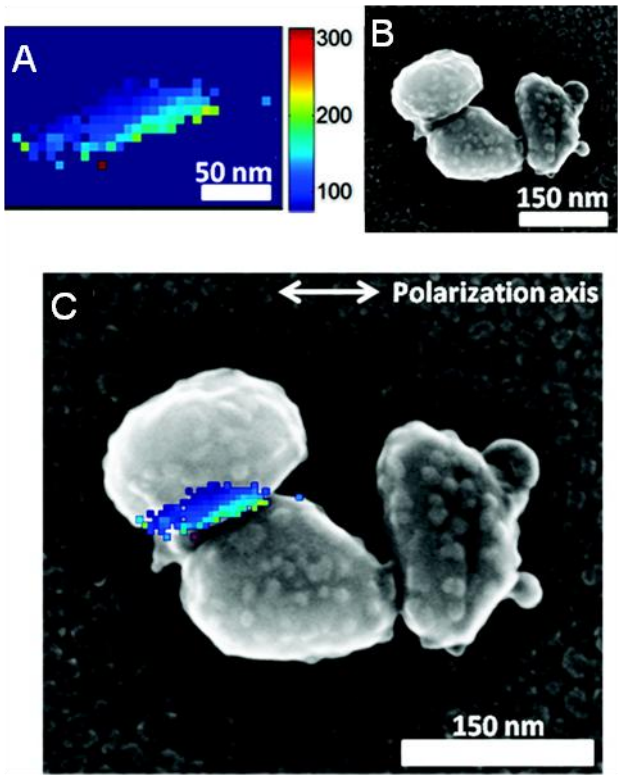

Figure 1.6. (A) SERS spatial intensity map and (B) SEM image of a silver colloid trimer. (C) Overlay of the spatial intensity map and SEM image. Adapted with permission from Weber M. L. and Willets, K. A. Correlated Super-Resolution Optical and Structural Studies of Surface-Enhanced Raman Scattering Hot Spots in Silver Colloid Aggregates. *J. Phys. Chem. Lett.* **2011**, *2*, 1766-1770. Copyright 2011 American Chemical Society.

While the data shown above in Figure 1.6 indicates that the SERS centroid conforms closely to the shape and intensity profile expected of a SM-SERS "hot spot", it should be noted that this data represents a qualitative overlay of the super-resolution data with the SEM data.[36] Additionally, this data does not give any information on the source of the centroid motion, *i.e.* is this motion due to translation or rotation of the molecule or due to changes in the nanoparticle? The source of this emission is important to consider when using this technique to map the size and shape of "hot spots" on these structures. There have been several other studies on SM-SERS "hot spots" in these types of

aggregates that indicate that the polarization of the SERS emission from these structures can be strongly influenced by the aggregate geometry, indicating that the aggregate shape may also influence the emission centroid; there is also previous theoretical work in the field indicating that the SERS molecule should indeed have an effect on centroid position.[7,40–42]

1.5 Scope of this work

The overall goal of the research presented in this document is to develop and refine new tools to image plasmonic nanostructures below the diffraction limit, with a focus on techniques that can be used to map and understand the AgNP aggregates that enable SM-SERS. In Chapter 3, we start by using super-resolution imaging combined with the bianalyte approach in order to elucidate the role that the position of the molecule plays in dictating the centroid position of SM-SERS emission. Next, in Chapters 4-5, we develop the use of a dipole-emission PSF for use in super-resolution imaging of plasmonic emission. The dipole-emission PSF is one that has been used extensively in the field of single-molecule fluorescence, and cannot only provide a more accurate fit when used in super-resolution studies, but can also yield sub-diffraction-limited information about the orientation of the nanostructure under investigation. This technique is first developed in Chapter 4, where it is used to fit the plasmon-mediated luminescence of gold nanorods. We continue by applying this same technique to SERS active AgNP aggregates to further understand coupling between Raman active dyes and the plasmon modes of the enhancing aggregates (Chapter 5). Finally, in Chapter 6, we describe work towards mapping the size and strength of SERS enhancement regions around AgNP aggregates using a scanning probe. In this work, a carbon nanotube is attached to an atomic force microscope (AFM) probe and scanned over AgNP aggregates while the system is illuminated with an attached total internal reflection microscope.

1.6 References

(1) Willets, K. A.; Van Duyne, R. P. Localized Surface Plasmon Resonance Spectroscopy and Sensing. *Annu. Rev. Phys. Chem.* **2007**, *58*, 267–297.

(2) Haes, A. J.; Haynes, C. L.; McFarland, A. D.; Schatz, G. C.; Van Duyne, R. P.; Zou, S. Plasmonic Materials for Surface-Enhanced Sensing and Spectroscopy. *MRS Bull.* **2005**, *30*, 368–375.

(3) Halas, N. J.; Lal, S.; Chang, W.-S.; Link, S.; Nordlander, P. Plasmons in Strongly Coupled Metallic Nanostructures. *Chem. Rev.* **2011**, *111*, 3913–3961.

(4) Stiles, P. L.; Dieringer, J. A.; Shah, N. C.; Van Duyne, R. P. Surface-Enhanced Raman Spectroscopy. *Annu. Rev. Anal. Chem.* **2008**, *1*, 601–626.

(5) Hao, E.; Schatz, G. C. Electromagnetic Fields around Silver Nanoparticles and Dimers. *J. Chem. Phys.* **2004**, *120*, 357–366.

(6) Aroca, R. F. Plasmon Enhanced Spectroscopy. *Phys. Chem. Chem. Phys.* **2013**, *15*, 5355–5363.

(7) Ausman, L. K.; Schatz, G. C. On the Importance of Incorporating Dipole Reradiation in the Modeling of Surface Enhanced Raman Scattering from Spheres. *J. Chem. Phys.* **2009**, *131*, 084708–084708–10.

(8) McMahon, J. M.; Li, S.; Ausman, L. K.; Schatz, G. C. Modeling the Effect of Small Gaps in Surface-Enhanced Raman Spectroscopy. *J. Phys. Chem. C* **2012**, *116*, 1627–1637.

(9) Kerker, M.; Wang, D.-S.; Chew, H. Surface Enhanced Raman Scattering (SERS) by Molecules Adsorbed at Spherical Particles: Errata. *Appl. Opt.* **1980**, *19*, 4159–4174.

(10) Jain, P. K.; Huang, X.; El-Sayed, I. H.; El-Sayed, M. A. Noble Metals on the Nanoscale: Optical and Photothermal Properties and Some Applications in Imaging, Sensing, Biology, and Medicine. *Acc. Chem. Res.* **2008**, *41*, 1578–1586.

(11) Lal, S.; Clare, S. E.; Halas, N. J. Nanoshell-Enabled Photothermal Cancer Therapy: Impending Clinical Impact. *Acc. Chem. Res.* **2008**, *41*, 1842–1851.

(12) Golightly, R. S.; Doering, W. E.; Natan, M. J. Surface-Enhanced Raman Spectroscopy and Homeland Security: A Perfect Match? *ACS Nano* **2009**, *3*, 2859–2869.

(13) Stranahan, S. M.; Willets, K. A. Super-Resolution Optical Imaging of Single-Molecule SERS Hot Spots. *Nano Lett.* **2010**, *10*, 3777–3784.

(14) Dieringer, J. A.; Lettan, R. B.; Scheidt, K. A.; Van Duyne, R. P. A Frequency Domain Existence Proof of Single-Molecule Surface-Enhanced Raman Spectroscopy. *J. Am. Chem. Soc.* **2007**, *129*, 16249–16256.

(15) Le Ru, E. C.; Meyer, M.; Etchegoin, P. G. Proof of Single-Molecule Sensitivity in Surface Enhanced Raman Scattering (SERS) by Means of a Two-Analyte Technique. *J. Phys. Chem. B* **2006**, *110*, 1944–1948.

(16) Michaels, A. M.; Nirmal, M.; Brus, L. E. Surface Enhanced Raman Spectroscopy of Individual Rhodamine 6G Molecules on Large Ag Nanocrystals. *J. Am. Chem. Soc.* **1999**, *121*, 9932–9939.

(17) Kneipp, K.; Wang, Y.; Kneipp, H.; Perelman, L. T.; Itzkan, I.; Dasari, R. R.; Feld, M. S. Single Molecule Detection Using Surface-Enhanced Raman Scattering (SERS). *Phys. Rev. Lett.* **1997**, *78*, 1667–1670.

(18) Nie, S.; Emory, S. R. Probing Single Molecules and Single Nanoparticles by Surface-Enhanced Raman Scattering. *Science* **1997**, *275*, 1102–1106.

(19) Camden, J. P.; Dieringer, J. A.; Wang, Y.; Masiello, D. J.; Marks, L. D.; Schatz, G. C.; Van Duyne, R. P. Probing the Structure of Single-Molecule Surface-Enhanced Raman Scattering Hot Spots. *J. Am. Chem. Soc.* **2008**, *130*, 12616–12617.

(20) Wustholz, K. L.; Henry, A.-I.; McMahon, J. M.; Freeman, R. G.; Valley, N.; Piotti, M. E.; Natan, M. J.; Schatz, G. C.; Duyne, R. P. V. Structure−Activity Relationships in Gold Nanoparticle Dimers and Trimers for Surface-Enhanced Raman Spectroscopy. *J. Am. Chem. Soc.* **2010**, *132*, 10903–10910.

(21) Michaels, A. M.; Jiang; Brus, L. Ag Nanocrystal Junctions as the Site for Surface-Enhanced Raman Scattering of Single Rhodamine 6G Molecules. *J. Phys. Chem. B* **2000**, *104*, 11965–11971.

(22) Kleinman, S. L.; Ringe, E.; Valley, N.; Wustholz, K. L.; Phillips, E.; Scheidt, K. A.; Schatz, G. C.; Van Duyne, R. P. Single-Molecule Surface-Enhanced Raman Spectroscopy of Crystal Violet Isotopologues: Theory and Experiment. *J. Am. Chem. Soc.* **2011**, *133*, 4115–4122.

(23) Gordon, M. P.; Ha, T.; Selvin, P. R. Single-Molecule High-Resolution Imaging with Photobleaching. *Proc. Natl. Acad. Sci. U. S. A.* **2004**, *101*, 6462–6465.

(24) Wang, Y.; Fruhwirth, G.; Cai, E.; Ng, T.; Selvin, P. R. 3D Super-Resolution Imaging with Blinking Quantum Dots. *Nano Lett.* **2013**.

(25) Yildiz, A.; Forkey, J. N.; McKinney, S. A.; Ha, T.; Goldman, Y. E.; Selvin, P. R. Myosin V Walks Hand-Over-Hand: Single Fluorophore Imaging with 1.5-Nm Localization. *Science* **2003**, *300*, 2061–2065.

(26) Rust, M. J.; Bates, M.; Zhuang, X. Sub-Diffraction-Limit Imaging by Stochastic Optical Reconstruction Microscopy (STORM). *Nat. Methods* **2006**, *3*, 793–796.

(27) Betzig, E.; Patterson, G. H.; Sougrat, R.; Lindwasser, O. W.; Olenych, S.; Bonifacino, J. S.; Davidson, M. W.; Lippincott-Schwartz, J.; Hess, H. F. Imaging Intracellular Fluorescent Proteins at Nanometer Resolution. *Science* **2006**, *313*, 1642–1645.

(28) Sagle, L. B.; Ruvuna, L. K.; Bingham, J. M.; Liu, C.; Cremer, P. S.; Van Duyne, R. P. Single Plasmonic Nanoparticle Tracking Studies of Solid Supported Bilayers with Ganglioside Lipids. *J. Am. Chem. Soc.* **2012**, *134*, 15832–15839.

(29) Gu, Y.; Sun, W.; Wang, G.; Fang, N. Single Particle Orientation and Rotation Tracking Discloses Distinctive Rotational Dynamics of Drug Delivery Vectors on Live Cell Membranes. *J. Am. Chem. Soc.* **2011**, *133*, 5720–5723.

(30) Gu, Y.; Wang, G.; Fang, N. Simultaneous Single-Particle Superlocalization and Rotational Tracking. *ACS Nano* **2013**, *7*, 1658–1665.

(31) Gu, Y.; Di, X.; Sun, W.; Wang, G.; Fang, N. Three-Dimensional Super-Localization and Tracking of Single Gold Nanoparticles in Cells. *Anal. Chem.* **2012**, *84*, 4111–4117.

(32) Marchuk, K.; Ha, J. W.; Fang, N. Three-Dimensional High-Resolution Rotational Tracking with Superlocalization Reveals Conformations of Surface-Bound Anisotropic Nanoparticles. *Nano Lett.* **2013**, *13*, 1245–1250.

(33) Blythe, K. L.; Mayer, K. M.; Weber, M. L.; Willets, K. A. Ground State Depletion Microscopy for Imaging Interactions between Gold Nanowires and Fluorophore-Labeled Ligands. *Phys. Chem. Chem. Phys.* **2013**, *15*, 4136–4145.

(34) Lin, H.; Centeno, S. P.; Su, L.; Kenens, B.; Rocha, S.; Sliwa, M.; Hofkens, J.; Uji-i, H. Mapping of Surface-Enhanced Fluorescence on Metal Nanoparticles Using Super-Resolution Photoactivation Localization Microscopy. *ChemPhysChem* **2012**, *13*, 973–981.

(35) Zhou, X.; Andoy, N. M.; Liu, G.; Choudhary, E.; Han, K.-S.; Shen, H.; Chen, P. Quantitative Super-Resolution Imaging Uncovers Reactivity Patterns on Single Nanocatalysts. *Nat. Nanotechnol.* **2012**, *7*, 237–241.

(36) Weber, M. L.; Willets, K. A. Correlated Super-Resolution Optical and Structural Studies of Surface-Enhanced Raman Scattering Hot Spots in Silver Colloid Aggregates. *J. Phys. Chem. Lett.* **2011**, *2*, 1766–1770.

(37) Weber, M. L.; Litz, J. P.; Masiello, D. J.; Willets, K. A. Super-Resolution Imaging Reveals a Difference between SERS and Luminescence Centroids. *ACS Nano* **2012**, *6*, 1839–1848.

(38) Titus, E. J.; Weber, M. L.; Stranahan, S. M.; Willets, K. A. Super-Resolution SERS Imaging beyond the Single-Molecule Limit: An Isotope-Edited Approach. *Nano Lett.* **2012**, *12*, 5103–5110.

(39) Willets, K. A.; Stranahan, S. M.; Weber, M. L. Shedding Light on Surface-Enhanced Raman Scattering Hot Spots through Single-Molecule Super-Resolution Imaging. *J. Phys. Chem. Lett.* **2012**, *3*, 1286–1294.

(40) Shegai, T.; Li, Z.; Dadosh, T.; Zhang, Z.; Xu, H.; Haran, G. Managing Light Polarization via Plasmon–Molecule Interactions Within an Asymmetric Metal Nanoparticle Trimer. *Proc. Natl. Acad. Sci.* **2008**, *105*, 16448–16453.

(41) Li, Z.; Shegai, T.; Haran, G.; Xu, H. Multiple-Particle Nanoantennas for Enormous Enhancement and Polarization Control of Light Emission. *ACS Nano* **2009**, *3*, 637–642.

(42) Shegai, T.; Brian, B.; Miljković, V. D.; Käll, M. Angular Distribution of Surface-Enhanced Raman Scattering from Individual Au Nanoparticle Aggregates. *ACS Nano* **2011**, *5*, 2036–2041.

Chapter 2: Methods

2.1 Sample preparation

Silver nanoparticle preparation

For all studies using colloidal silver nanoparticles, the Lee and Meisel method was used to synthesize the colloids.[1] First, a 500 mL flask (containing a magnetic stir bar) and a 50 mL flask are both filled with aqua regia and allowed to sit for over one hour, in order to remove metal contaminants from the reaction vessel. Aqua regia is a 1:3 volume mixture of nitric acid:hydrochloric acid; due to its highly corrosive properties, it should be handled with care in a fume hood. After all glassware is cleaned and rinsed with nanopure water until at neutral pH, approximately 45 mg of $AgNO_3$ (Sigma-Aldrich) is dissolved in 250 mL nanopure water in the 500 mL flask. This solution is heated to boiling, and then 5 mL of a 10% w/w solution of sodium citrate (Sigma-Aldrich), which is mixed in the smaller flask with nanopure water, is added to the large flask. This mixture is boiled for 1 hour, where it takes on a cloudy gray color, and then cooled. Any volume loss due to boiling is replaced with additional nanopure water.

SERS sample preparation

In order to prepare SERS (or SM-SERS) samples with the silver colloid solution, a 5 μL aliquot of rhodamine 6G (R6G) solution in methanol is combined with an aliquot (typically 100 μL) of silver colloids. This combination is vortexed for approximately 30 s, and then an aliquot of 20 mM NaCl solution is added, and the solution is vortexed for another 30 s. The volume of the NaCl aliquot used is the same as the silver colloid aliquot volume. In the case of SM-SERS samples, the concentration of the R6G solution is such that the final dye concentration in the sample is usually between 2-5 nM.[2,3] In the case where the isotope edited bianalyte approach is used, the final dye concentration in the

sample mixture is 1-2.5 nM in both R6G-*d0* and R6G-*d4*. In the case of multi-molecule SERS (MM-SERS) samples, the R6G solution is adjusted so that the final concentration of R6G is 200 nM. After mixing the SERS solutions, they are incubated in the dark between 10 minutes and 15 hours. Short incubation times are used when smaller aggregates (such as dimers) are desired. In the case of MM-SERS samples, the solution is centrifuged at ~500g for 10 minutes and resuspended in 10 mM NaCl at an 8x dilution (8x the volume of the pre-centrifuged sample) in order to minimize the presence of excess dye[4].

SERS slide preparation

In order to prepare coverslips (#1 thickness) for deposition of particles, they were first cleaned using argon plasma for approximately 15 minutes. After plasma cleaning, the slides were then functionalized with a coating of (3-Aminopropyl)triethoxysilane (APTES). Briefly, a 0.5% v/v solution of APTES in ethanol is prepared, the slides are incubated in the solution on an orbital shaker, then rinsed in both ethanol and nanopure water, and dried under a stream of dry N_2. Incubation time is adjusted between 1-10 minutes in order to control the density of sample coverage on the slide. After APTES functionalization, a 5 μL aliquot of SERS solution is allowed to sit on the slide for several seconds, and is blown off of the surface with a stream of N_2. After deposition of the SERS sample, a 5 μL aliquot of a 50x dilution of 500 nm sky blue polystyrene fluorescent beads (Spherotech) is dropcast onto the same region of the slide. This drop is allowed to sit for 5 minutes before being gently rinsed with nanopure water and dried under a gentle stream of N_2. Samples are typically imaged immediately after preparation. When not being imaged or undergoing AFM, samples were kept in a darkened vacuum dessicator.

Gold nanorod slide preparation

CTAB-stabilized gold nanorods (AuNR) were prepared in the lab using previously published methods.[5,6] First, a 1 mL aliquot of prepared AuNRs is centrifuged 3x at ~6700g for 20 minutes in order to remove excess CTAB from the nanorods. After the last centrifugation, the nanorods are suspended in 500 μL nanopure water to form a 2x concentrated solution. This solution is then dropcast onto an APTES functionalized coverslip and allowed to sit for 5 minutes before being rinsed thoroughly with nanopure water and dried with a stream of dry N_2. After drying the slide, a 5 μL aliquot of a 50x dilution of either 500 nm or 200 nm sky blue fluorescent polystyrene beads (Spherotech) is dropcast onto the slide to act as markers for stage drift correction.

2.2 Optical microscopy instrumentation

The optical microscopy setup used in Chapters 3-5 is based around an Olympus IX-71 inverted optical microscope, which uses a variable NA (0.6-1.3) 100x oil immersion objective. This microscope is configured for widefield, epi-illumination laser excitation and transmission darkfield scattering using a tungsten white-light source and condenser. A block diagram of this system can be seen below in Figure 2.1. 532 nm quasi-circularly polarized light is used for all experiments. On the detection side of the microscope, the image is relayed to a non-polarizing cube beamsplitter, which sends half of the collected light to an electron-multiplied CCD camera (EMCCD, Princeton Instruments ProEM), and the rest to a spectrometer with a liquid nitrogen cooled spectroscopy CCD camera (Princeton Instruments 2500i/Spec10). The timing of the two detectors is synced to ensure that the spectral and image data are correlated in time.

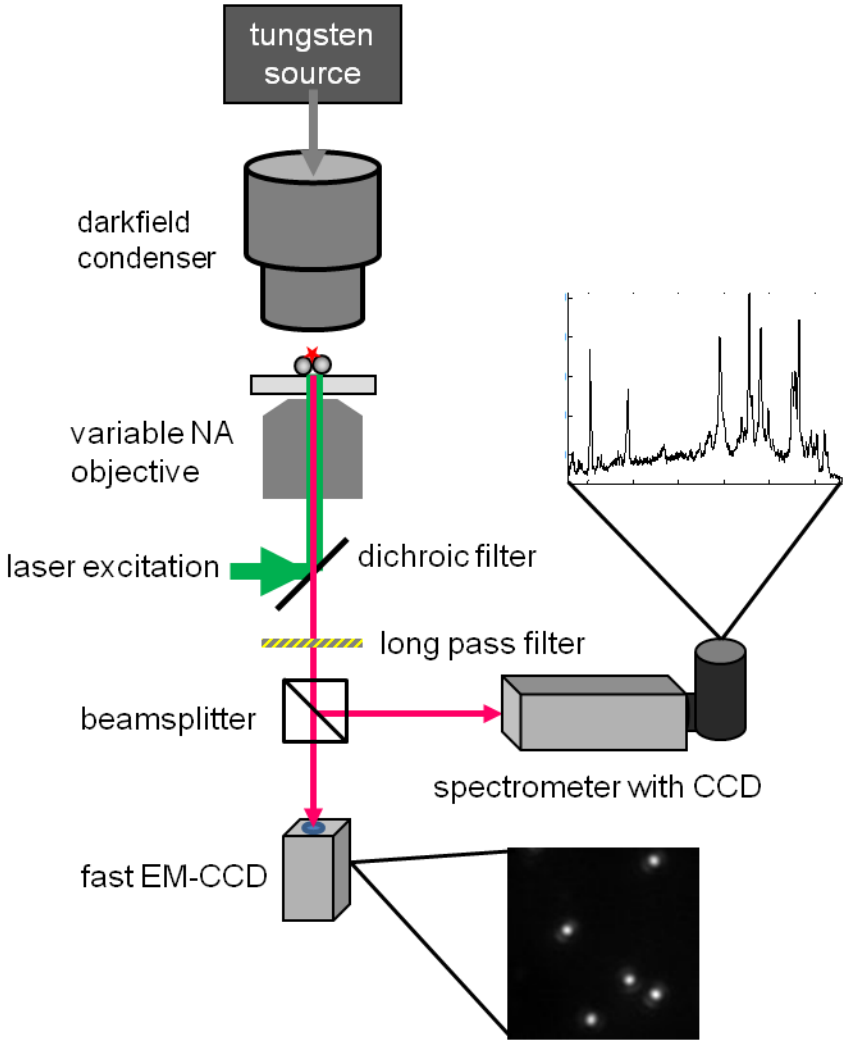

Figure 2.1 Block diagram of widefield microscope setup.

2.3 Correlated AFM and optical microscopy experiments

Instrumentation

For all experiments utilizing AFM, or correlated AFM and optical microscopy imaging, a combined total internal reflection (TIR)/AFM microscope system was used.[7] This system uses oil-immersion through-the-objective TIR for both white light and laser illumination, and the AFM head uses an IR laser to detect deflection of the AFM probe, in order to not interfere with the collection of optical data. A block diagram of this setup

can be seen in Figure 2.2. In TIR microscopy, excitation light is incident on the underside of the slide above the glass/air critical angle, which causes TIR and generates a quickly decaying evanescent field at the surface of the slide. This microscopy technique allows for both AFM and optical imaging to take place simultaneously.

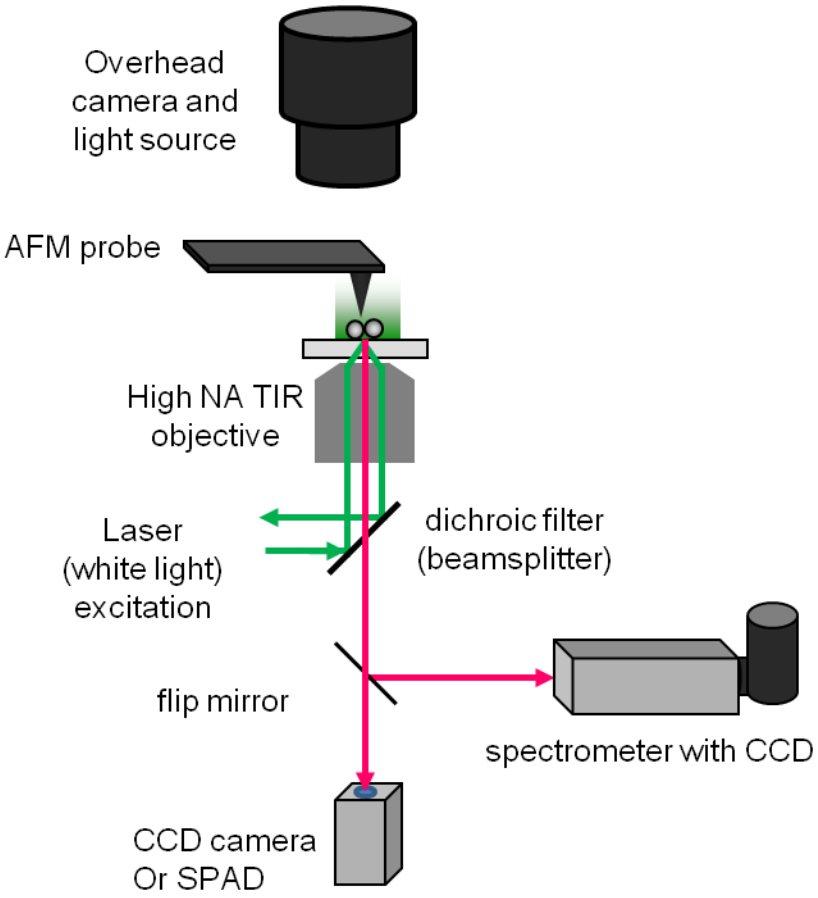

Figure 2.2. Block diagram of combined TIR/AFM setup. SPAD: single-photon avalanche diode.

AFM correlation of widefield super-resolution experiments

In the experiments presented in Chapters 3-5, after optical experiments were carried out on the widefield microscope (shown in Section 2 of this chapter), samples

were transferred to the combined TIR/AFM microscope in order to obtain correlated AFM images. In order to locate the particles from the optical experiment, experiments are carried out on gridded coverslips. These are prepared by depositing a 90 nm aluminum film onto the slide, using a bare copper TEM grid as a mask. The result is an alphanumeric aluminum grid on the coverslip, which can be used to locate regions of interest (ROIs) on both microscopes, as shown in Figure 2.3; Figure 2.3A is an image from the overhead AFM optical camera, showing the location of the AFM cantilever in relation to the gridded slide, and Figure 2.3B is a white light TIR image showing the scattering from both the nanoparticles on the slide and the AFM probe. Because calibrated, closed-loop AFM images can be correlated with optical data, this allows us to also use this technique to calibrate the pixel size of the widefield microscopy setup as well.[8]

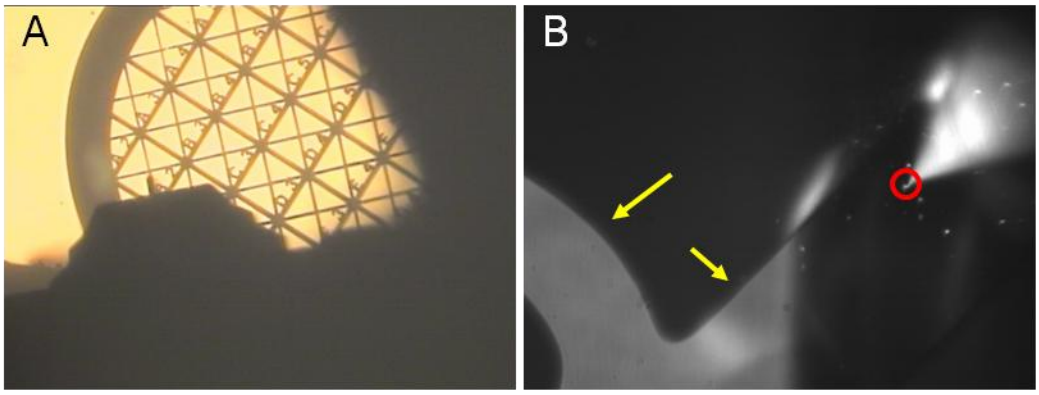

Figure 2.3. (A) Bright field image of a gridded coverslip taken with the AFM (overhead) optical camera. Aluminum coated areas appear bright in the image. The AFM cantilever is located in grid B-2 in the image. (B) Dark field image of R6G-labled silver nanoparticles on the patterned coverslip taken with a TIRF objective using TIR dark field imaging. Scattering from the AFM probe is circled. The edge of the aluminum alignment grid appears dark in this image and is indicated by the yellow arrows. Adapted with permission from Stranahan, S. M.; Titus, E. J.; Willets, K. A. SERS Orientational Imaging of Silver Nanoparticle Dimers. *J. Phys Chem. Lett.* **2011**, *2*, 2711-2715. Copyright 2011 American Chemical Society.

2.4 Super-resolution microscopy

Experimental conditions

When imaging samples for the purpose of super-resolution imaging, samples are first prepared as described in Section 1. Once samples are prepared and on the microscope, the environment around the sample can be controlled via a nitrogen dry-box placed on the microscope stage, as was done for some samples in Chapter 5. The laser excitation used in super-resolution imaging is at 532 nm in a widefield setup, with powers ranging from approximately 400-800 W/cm^2 for SERS samples, and approximately 8.8 kW/cm^2 for gold nanorods. The studies presented in this work all used quasi-circularly polarized light. Regions for analysis are selected based on particle intensity dynamics and the presence of 2 or more fluorescent marker beads in the field of view in order to properly correct for stage drift. EMCCD/spectrometer integration times

range from 0.1-0.4 s/1-2 s for SERS data, and 5 s/frame for AuNR luminescence data. After super-resolution images are collected, a darkfield scattering image of the region is collected for structure correlation purposes. An example of a correlated widefield laser image and darkfield image are shown below in Figure 2.4.

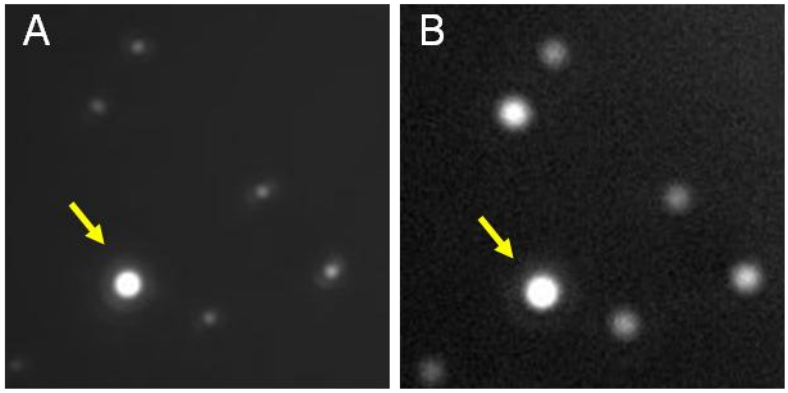

Figure 2.4. Widefield laser image (A) and darkfield image (B) of AuNR luminescence and fluorescent bead (yellow arrow).

Gaussian fitting and background subtraction of images

Super-resolution in this work is achieved through localizing the centroid position of the emission by fitting it using a model point-spread function (PSF). A commonly used model PSF for this technique is the 2-dimensional Gaussian function, shown in Equation 2.1

$$I(x,y) = z_0 + I_0 e^{\left[-\frac{1}{2}\left[\left(\frac{x-x_0}{s_x}\right)^2 + \left(\frac{y-y_0}{s_y}\right)^2\right]\right]} \qquad (2.1)$$

In this equation, the spatially dependent intensity, I(x,y) is a function of the following parameters, which can be extracted by fitting experimental data to this equation: z_0 (background intensity), I_0 (peak intensity), x_0/y_0 (centroid position), and s_x/s_y (width of the Gaussian). While the Gaussian function does not account for all aspects of the true

PSF, it is a common, computationally inexpensive model; more accurate models are discussed elsewhere in this document.

Proper application of the Gaussian model, or any other PSF model, to the data first requires that other sources of emission are accounted for within the diffraction-limited spot. When fitting with a Gaussian, multiple emission sites within a diffraction-limited spot will result in centroid fits that represent the intensity-weighted super-position of the underlying emission centroids.[9] In the case of the SERS studies in this work, background luminescence from the silver nanoparticles is subtracted off (when possible) in order to deconvolute the SERS emission centroid from the luminescence.[2] In order to do this, SERS emission and background luminescence frames are identified through intensity vs. time plots and correlated spectra, as shown below in Figure 2.5. In this analysis, we identify background luminescence frames via a threshold intensity value, as shown in Figure 2.5A, which is determined by the user. Next, correlated spectra like the ones shown in Figure 2.5B are used to ensure that emission in frames below the threshold don't show signs of Raman scattering. Next, the mean luminescence Gaussian is subtracted off of all frames, and the resulting emission is fit to determine the SERS emission centroids.

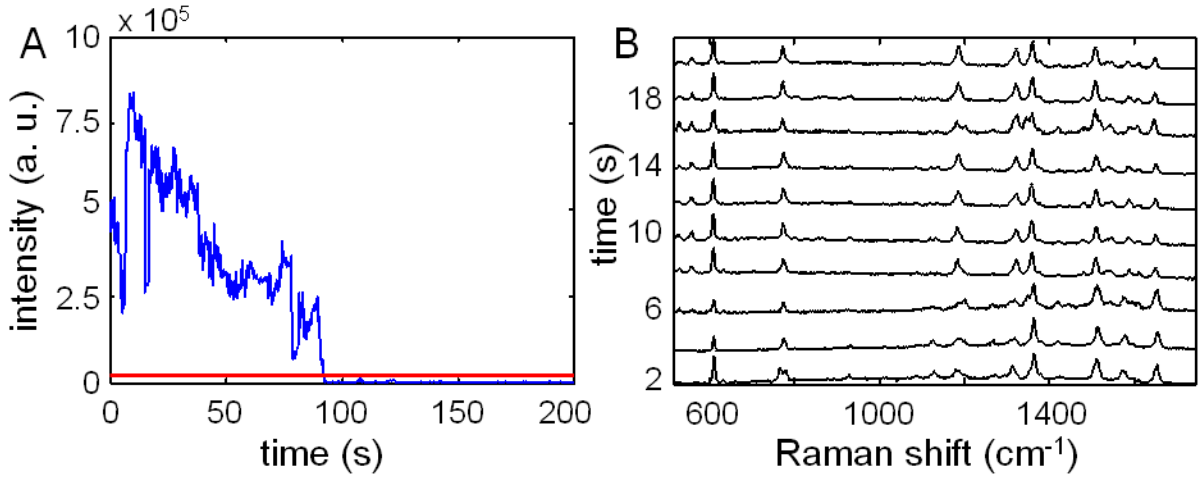

Figure 2.5. SERS aggregate intensity vs. time plot (A), based off of EMCCD image, with SERS/luminescence threshold shown in red. (B) Correlated spectra showing SERS emission for the first 20 seconds of the acquisition.

Data processing

After the nanoparticle luminescence has been fit and subtracted from the raw images, the resulting SERS fits are filtered *via* their R^2 values, usually with a threshold of 80%. This ensures that skewed centroid positions due to poor fits do not impact the final data. Example data, which corresponds to the intensity and spectral data shown in Figure 2.5, is shown in Figure 2.6. Figure 2.6A shows the R^2 filtered SERS centroid positions, where the mean luminescence centroid is at (0,0). While this plot can give insight into the SERS centroid location, the plot points are difficult to distinguish, and give no intensity information. For this reason, we analyze this data through use of frequency and intensity 2-dimensional histograms, shown in Figure 2.6B and C, respectively. The data shown in the scatter plot in Figure 2.6A are binned, based on their positions, into different pixels; Figures 2.6B-C both use 1 nm bins. Typically, the bin size used in these figures is on the order of the theoretically predicted uncertainty of the centroid position, given in Equation 2.2.[10]

$$\sigma_{\mu_i} = \sqrt{\frac{s_i^2}{N} + \frac{a^2/12}{N} + \frac{8\pi s_i^4 b^2}{a^2 N^2}} \qquad (2.2)$$

In this equation, the standard error of the mean of the PSF, σ_μ, is dependent upon the standard deviation of the Gaussian fit, s_i; the pixel size of the EM-CCD camera in nanometers, a; the standard deviation of the background in photons, b; and the total collected photons, N. Figure 2.6B shows a frequency histogram of the data, where the color axis indicates the number of SERS centroids falling within each binned pixel. In Figure 2.6C, the color axis indicates the mean intensity of the SERS events occurring within each bin, as determined by their centroids. The histogram representation of this data allows us to identify spatial locations exhibiting multiple events and/or high intensities.[2,3]

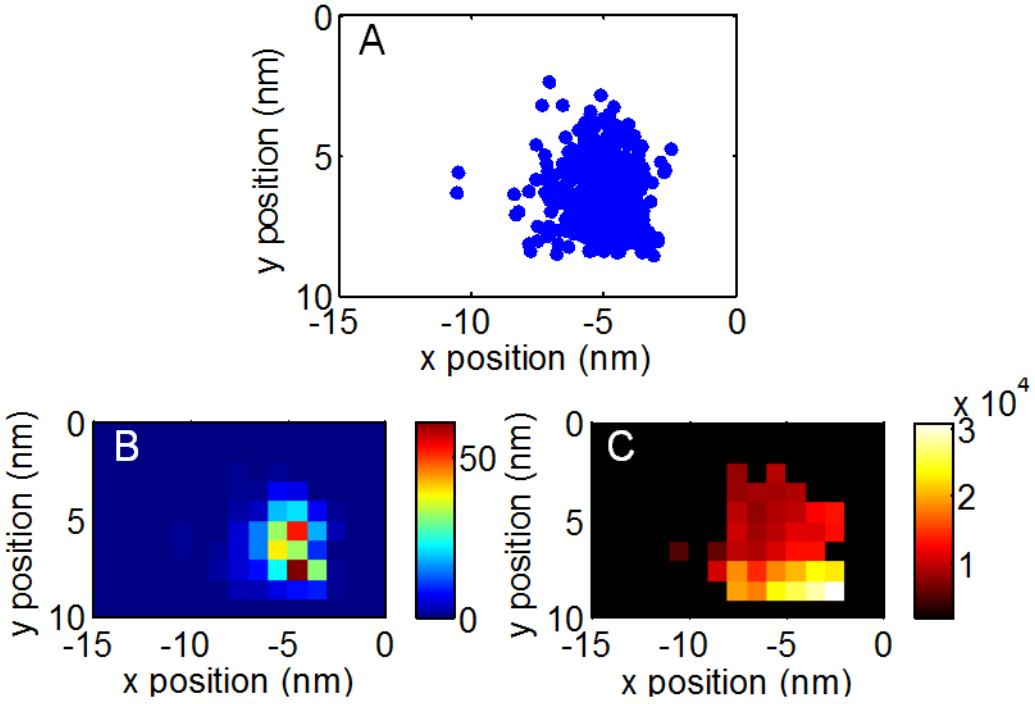

Figure 2.6. Scatter plot of luminescence corrected SERS centroid positions (A), where (0,0) is the mean luminescence centroid. Frequency (B) and intensity (C) 2-dimensional histogram representations of (A). The bin size in (B) and (C) is 1 nm.

2.5 Acknowledgement

I would like to acknowledge Karole Blythe for making all of the AuNRs used in my studies, as well as her advice in AuNR sample slide preparation.

2.6 References

(1) Lee, P. C.; Meisel, D. Adsorption and Surface-Enhanced Raman of Dyes on Silver and Gold Sols. *J. Phys. Chem.* **1982**, *86*, 3391–3395.

(2) Stranahan, S. M.; Willets, K. A. Super-Resolution Optical Imaging of Single-Molecule SERS Hot Spots. *Nano Lett.* **2010**, *10*, 3777–3784.

(3) Weber, M. L.; Willets, K. A. Correlated Super-Resolution Optical and Structural Studies of Surface-Enhanced Raman Scattering Hot Spots in Silver Colloid Aggregates. *J. Phys. Chem. Lett.* **2011**, *2*, 1766–1770.

(4) Shegai, T.; Brian, B.; Miljković, V. D.; Käll, M. Angular Distribution of Surface-Enhanced Raman Scattering from Individual Au Nanoparticle Aggregates. *ACS Nano* **2011**, *5*, 2036–2041.

(5) Ming, T.; Zhao, L.; Yang, Z.; Chen, H.; Sun, L.; Wang, J.; Yan, C. Strong Polarization Dependence of Plasmon-Enhanced Fluorescence on Single Gold Nanorods. *Nano Lett.* **2009**, *9*, 3896–3903.

(6) Mayer, K. M.; Lee, S.; Liao, H.; Rostro, B. C.; Fuentes, A.; Scully, P. T.; Nehl, C. L.; Hafner, J. H. A Label-Free Immunoassay Based Upon Localized Surface Plasmon Resonance of Gold Nanorods. *ACS Nano* **2008**, *2*, 687–692.

(7) Kaplan-Ashiri, I.; Titus, E. J.; Willets, K. A. Subdiffraction-Limited Far-Field Raman Spectroscopy of Single Carbon Nanotubes: An Unenhanced Approach. *ACS Nano* **2011**, *5*, 1033–1041.

(8) Stranahan, S. M.; Titus, E. J.; Willets, K. A. SERS Orientational Imaging of Silver Nanoparticle Dimers. *J. Phys. Chem. Lett.* **2011**, *2*, 2711–2715.

(9) Gordon, M. P.; Ha, T.; Selvin, P. R. Single-Molecule High-Resolution Imaging with Photobleaching. *Proc. Natl. Acad. Sci. U. S. A.* **2004**, *101*, 6462–6465.

(10) Thompson, R. E.; Larson, D. R.; Webb, W. W. Precise Nanometer Localization Analysis for Individual Fluorescent Probes. *Biophys. J.* **2002**, *82*, 2775–2783.

Chapter 3: Super-Resolution SERS Imaging beyond the Single-Molecule Limit: An Isotope-Edited Approach[1]

3.1 Introduction

One of the major difficulties when studying single-molecule surface-enhanced Raman scattering (SM-SERS) substrates is due to their extremely small size; the true location of the hot spot, its size, the location of the molecule on the nanoparticle surface, and the nanoscale features of the nanoparticle that are required for SM-SERS enhancement are obscured by the optical diffraction limit, which limits the resolution of optical studies of this phenomenon[1–4]. In order to overcome the diffraction limit, super-resolution optical imaging has recently emerged as a powerful tool for studying SM-SERS hot spots in an effort to understand what hot spot properties enable the highest electromagnetic field enhancements.[5–8] In super-resolution imaging, the point spread function (PSF) of a diffraction-limited spot is approximated as a two-dimensional Gaussian function in order to extract the spatial origin of the emitter.[9,10] However, in SM-SERS, the molecule responsible for the observed signal is coupled to a plasmonic nanoparticle, and thus the observed emission is a convolution of the Raman scattering from the molecule coupled to and radiated by the plasmon modes of the nanoparticle substrate.[5,11,12] As a result, when the PSF of the SM-SERS signal is fit, the location of the emitter cannot be correlated in a one-to-one fashion with the position of the molecule.

In previous work from our group, we used super-resolution imaging to show that the spatial origin of SM-SERS signals varied over time by as much as 50 nm and was highly correlated with changes in the SERS intensity.[5,7,8] Because the position of the nanoparticle substrate is fixed in these experiments, we hypothesized that motion of the

[1] Reproduced in part with permission from Titus, E. J.; Weber, M. L.; Stranahan, S. M.; Willets, K. A. Super-Resolution SERS Imaging beyond the Single-Molecule Limit: An Isotope-Edited Approach. *Nano Lett.* **2012,** *6,* 5103-5110. Copyright 2012 American Chemical Society.

probe molecule on the nanoparticle surface led to changes in the SERS intensity and corresponding shifts in the calculated SERS centroid.[5,13] This hypothesis was supported by theoretical calculations from Ausman and Schatz, which predict that changing the location of a emitting dipole on the surface of a nanoparticle dimer will shift the scattering near-field distribution surrounding that dimer.[12] We proposed that a shift in the near-field scattering distribution around the nanoparticle would translate to a shift of the PSF in the far-field, thus supporting our hypothesis that translation of the molecule on the nanoparticle surface led to the observed changes in the spatial position of the SERS emission in our experiments. However, alternate hypotheses have been proposed to explain our results, including spurious signal from the nanoparticle itself, reorientation of the probe molecule on the nanoparticle surface, polarization effects from the excited nanoparticle antennae modes, and even damage to the underlying nanoparticle. In this Chapter, we provide unambiguous proof that the position of the molecule impacts the measured SERS centroid position and is the dominant mechanism by which the SERS centroid shifts over time.

For these studies, the isotope-edited bi-analyte SERS approach, first introduced by Van Duyne and coworkers, is used.[3] The bi-analyte method uses equal amounts of two isotopologues as the SERS probe molecules, allowing for identification of each analyte through distinct marker modes in the SERS spectra. The non-deuterated R6G (R6G-*d0*) and its deuterated isotopologue (R6G-*d4*) are ideal candidates for bi-analyte SERS measurements due to the high Raman cross-section of R6G and clearly distinguishable marker modes at ~609 cm^{-1} (R6G-*d0*) and ~597 and ~1334 cm^{-1} (R6G-*d4*), with all other vibrational modes positioned at identical Raman shifts (Figure 1.4, Chapter 1). We prepare SERS samples with the bianalyte dye mixture adsorbed onto randomly assembled Ag colloid aggregates aggregated by 20 mM $NaCl_{(aq)}$.[14] This SERS solution is dropcast

onto an aminopropyltriethyoxysilane-functionalized glass coverslip patterned with an aluminum alpha-numeric grid.[15] The slide is placed on an inverted optical microscope equipped with a 532 nm laser and a beamsplitter that sends half of the SERS signal to an electron-multiplied charge-coupled device (EM-CCD) for PSF imaging, and the other half of the SERS signal to a spectrometer coupled to a liquid nitrogen cooled CCD camera for correlated SERS spectral data. The optical data is then correlated with aggregate structure using AFM after the experiment. More details regarding the experimental methods can be found in Chapter 2.

3.2 Effects due to position of molecules

The intensity time trace shown in Figure 3.1A is acquired by integrating the scattering intensity originating from the diffraction-limited spot generated by the SERS active aggregate shown in Figure 3.1D. The entire acquisition time is 200 s with 0.4 s image frames (500 frames total), although only the intensity data from the first 60 seconds is shown. The concentration of each dye in the original sample is 1.5 nM (~ 3 molecules per nanoparticle). This SERS intensity time trace exhibits step-like behavior going from low intensity (0 – 40 s) to a higher intensity (40 – 53 s) before a final return to background. These two time intervals, in which the SERS signal fluctuates around two different average intensities before the final intensity step to background, suggests the presence of multiple molecules contributing to this SERS on-event. This behavior is in contrast to intensity time traces we have reported in previous work, where the average intensity of a SERS on-event fluctuated around a single intensity level before the SERS signal turned off, suggesting behavior more consistent with a single-molecule event.[5]

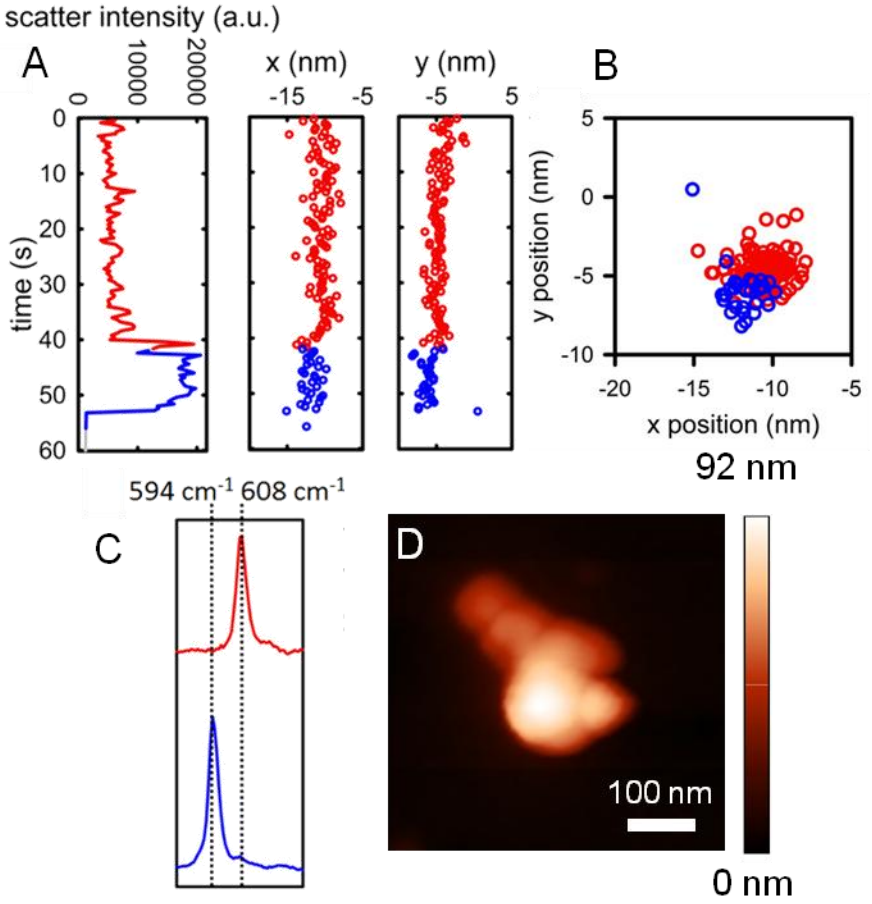

Figure 3.1. (A) Intensity time trace (left) and x- and y- SERS centroid trajectories (middle and right), colored-coded according to the identity of the emitting analyte: R6G-d4 (blue) and R6G-d0 (red). (B) Scatter plot of all SERS centroid positions from (A) with (0, 0) set at the position of the nanoparticle luminescence. Color corresponds to the identity of the emitting analyte as in (A). (C) Average SERS spectra for the first 41.6 seconds of the time trace (red) and time 41.6 – 53 seconds (blue) show switching between R6G-d0 and R6G-d4, respectively. (D) AFM scan of the SM-SERS active aggregate.

We use correlated SERS spectra (Figure 3.1C) to identify the analyte responsible for SERS emission at each time point in Figure 3.1A and color-code the time points as blue (R6G-*d4*) or red (R6G-*d0*). All identifications are made according to the presence of marker modes at ~608 cm^{-1} for R6G-d0 and ~593 cm^{-1} for R6G-d4. Vibrational mode

frequency shifts are characteristic of SM-SERS and we note the small shift in marker mode frequencies in this example from the ensemble measured marker modes to 594 cm^{-1} for R6G-d4. In the case of the R6G-*d4* assignment, we note a small shoulder in the peak that could be a small contribution from R6G-*d0*. However, given the dominance of the R6G-*d4* peak, we believe that this molecule contributes the bulk of the signal to the measured PSF.

To analyze these data, we follow a procedure described in previous work.[5,8] We begin by identifying frames that correspond to no SERS activity but have a weak luminescent background originating from the nanoparticle. The nanoparticle luminescence is fit to Equation 3.1 below:

$$I(x,y) = z_0 + I_0 e^{\left[-\frac{1}{2}\left[\left(\frac{x-x_0}{s_x}\right)^2 + \left(\frac{y-y_0}{s_y}\right)^2\right]\right]} \qquad (3.1)$$

In this equation, $I(x,y)$ is the spatially-dependent intensity, z_0 is the background, x_0 and y_0 are the centroid of the fit, and s_n is the standard deviation (width) in the n-direction.[9,16] Using this approach, we approximate the position of a single emitter as the location of the centroid of the fit, i.e. (x_0, y_0). Once we have the contribution of the nanoparticle, we subtract it from the image data corresponding to SERS activity (here, 0 – 53 seconds) in order to obtain the PSF corresponding to the isolated SERS signal. The SERS PSF is then fit to Equation 3.1 to extract the centroid position corresponding to the SERS signals.

In Figure 3.1A, we plot the calculated x_0 and y_0 coordinates of the fitted SERS centroids against time (right two columns) next to the intensity time trace (left column). The corresponding spectral data are shown in Figure 3.1C and allow us to assign each centroid coordinate to a specific analyte. Each SERS spectrum is acquired over 2 s while each SERS image is 0.4 s so there are approximately five SERS centroid fits per spectrum. Because of this difference in time resolution, the analyte assignments are

limited by the time resolution of the spectra. Based on the SERS spectra, we see that the R6G-d0 and R6G-d4 exchange over the course of the experiment, with the intensity step in the time trace corresponding to a change in analyte identity.

We create a scatter plot of all SERS centroid fits from time 0 – 53 s in Figure 3.1B, color-coded with the same analyte assignments. This plot shows that the average SERS centroid positions corresponding to R6G-*d0* or R6G-*d4* (red and blue data points, respectively) are offset from each other by ~2 nm. Based on our photon counts, image pixel size, and background noise, the theoretical uncertainty in the centroid fit is ~0.2 nm for the R6G-*d4* and ~0.3 nm for the R6G-*d0*, indicating that the centroid offset between the R6G-*d0* and R6G-*d4* only events is not simply uncertainty due to noise (see chapter 2).[9] Given that we have two distinct molecules on the nanoparticle surface and each appears at a discrete centroid position, these data allow us to conclude that the centroid position must be linked to a property of the molecule. If the nanoparticle alone were dictating the emission centroid (through spurious blinking in its luminescence), we would not expect each individual molecule to appear at a unique location.[17]

Another important feature of these data is the distance of the two SERS centroids from the site of nanoparticle luminescence. We arbitrarily set the centroid of the luminescence at (0,0), and the scatter plot in Figure 3.1B shows that both centroids are offset from the luminescence centroid by more than 10 nm in the x-direction and 5 nm in the y-direction. In previous work, we have shown that the luminescence centroid reflects the collective plasmon modes of the nanostructure, while the SERS centroid is related to local plasmon modes based on the position of the molecule; in the case of larger aggregates, the two centroids can therefore be offset by tens of nanometers.[7] The AFM image of this nanostructure, shown in Figure 3.1D, shows a large multi-nanoparticle

aggregate, which explains the offset between the SERS and luminescence centroids, but makes it difficult to assign the precise location of the hot spot.

To explain the offset between the two centroid positions of the R6G-*d0* and R6G-*d4*, we speculate that differences in the position of the two molecules on the aggregate surface is responsible for the differences in the SERS centroids. A difference in the position of each molecule on the nanoparticle surface would lead to a difference in its ability to couple with and be re-radiated by the nanoparticle plasmon modes;[12] as a result, the SERS centroid will appear in a spatially distinct location for the two analytes. We emphasize that the SERS centroid is *not* directly reporting on the position of the molecule on the nanoparticle surface, rather it is reporting how the nanoparticle re-radiates the Raman scattering from an adsorbed molecule into the far field. As the position of the molecule changes, how the plasmon re-radiates the SERS into the far field will also change, leading to a shift in the calculated SERS centroid. However, one could also argue that the two molecules are exchanging between the same molecule-sized hot spot, and the shift in the centroid is due exclusively to orientation effects of the different molecules within that hot spot.

To address this hypothesis, we present a second example in which the intensity changes in a stepwise fashion in Figure 3.2. In this example, both R6G-*d0* and R6G-*d4* are emitting simultaneously for the first 47 seconds, followed by a stepwise decrease in intensity that corresponds to a loss of the signal from the R6G-*d4* (Figure 3.2A and 3.2C). Here, the concentration of R6G-*d0* and R6G-*d4* are both 2.5 nM in the original sample mixture (~5 molecules per nanoparticle). In this time trace, the SERS intensity never drops to background, preventing us from subtracting away the luminescence background as in the previous example; as a result, we fit all frames using Equation 3.1.

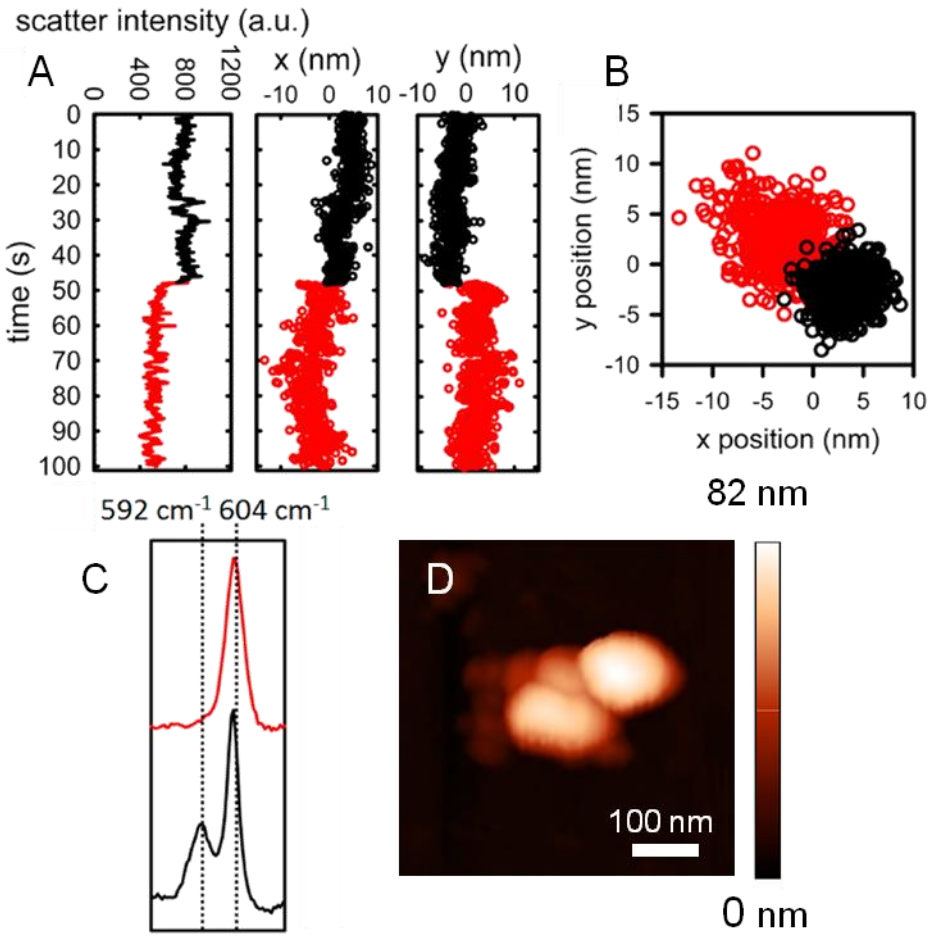

Figure 3.2. (A) Intensity time trace (left) and x- and y- SERS centroid trajectories (middle and right), colored-coded according to the identity of the emitting analyte(s): both R6G-d0 and R6G-d4 (black) and R6G-d0 (red). (B) Scatter plot of all SERS centroid positions from (A) with (0, 0) set at the average value of the SERS centroid. Color corresponds to the identity of the emitting analyte(s) as in (A).(C) Average SERS spectra for the first 47.7 seconds of the time trace (black) and time 47.8 – 100 seconds (red) showing switching between both molecules emitting, and then R6G-d0 alone, respectively. (D) AFM scan of the SM-SERS active aggregate.

The resulting centroid values in x and y are plotted in Figure 3.2A, color coded as either both R6G-*d0* and R6G-*d4* (black) or R6G-*d0* alone (red). In this case, a clear change in the centroid position occurs when the intensity drops due to the loss of the

R6G-*d4* signal. To better visualize this change, a scatter plot of the centroid values is shown in Figure 3.2B and, again, we observe a clear offset between the two centroid positions with a distance between the mean centroid values of ~8.2 nm. In the case when both molecules are emitting simultaneously, we expect the fitted centroid to report an intensity-weighted super-position of the two individual emission centroids.[18] When the signal from the R6G-*d4* turns off (due to either photobleaching or movement out of the hot spot), the centroid shifts because the PSF changes from a super-position of the two emitters to a single PSF dictated by the isolated R6G-*d0*.[18] Because the centroid changes when the the R6G-d4 molecules goes off, we know that the centroids from the two individual molecules are spatially distinct, similar to the data in Figure 3.1. Given that both molecules are emitting simultaneously during the first 47 seconds, we also know that the signal is not coming from a single molecule-sized hot spot. Lastly, we know that the molecules must be spatially distinct on the nanoparticle surface (AFM data showing the aggregate topography can be seen in Figure 3.2D), since two molecules cannot occupy the same physical space. Thus, these data further support our hypothesis that the location of the molecule on the surface influences the location of the calculated SERS centroid.

3.3 Effects of changing molecule orientation

Next, we show an example which allows us to rule out molecular orientation as the primary cause for changes in the SERS centroid. Figure 3.3A shows a third example of a time trace, collected from the aggregate shown in Figure 3.3D with a stepwise change in intensity. In this case, the concentration is 1 nM in each isotopologue (~2 molecules per nanoparticle). The intensity time trace shows a sharp drop in intensity at 64 s, much like the time trace in Figure 3.2. In this example, the molecule did turn off, but no nanoparticle luminescence was observed; given the still-unclear nature of this

background signal, it is impossible to speculate why the luminescence was so low for this sample.[19] Because we could not fit the nanoparticle background, the data were fit using a single Gaussian (Equation 3.1). Two representative spectra from both the high intensity interval (20 – 64 s) and the low intensity interval (64 – 151 s) are plotted in Figure 3.3C. The marker mode for R6G-*d4* (598 cm^{-1}) is present in all four spectra and the marker mode for R6G-*d0* (608 cm^{-1}) is absent in all four spectra, allowing us to identify all time points as originating exclusively from R6G-*d4.* We speculate two possible sources of the step-like behavior in the time trace: (1) there are two R6G-*d4* molecules emitting during the high intensity interval, and one turns off at ~64 seconds or (2) we have a single R6G-*d4* molecule emitting that reorients within the hot spot, thus changing its emission intensity. The former mechanism is consistent with the time trace and spectral data from Figure 3.2, while the latter mechanism is consistent with calculations from Xu and coworkers, which indicate that molecular orientation will affect SERS intensity due to changes in the coupling between the molecule and the plasmon modes of the nanoparticle antenna.[20,21]

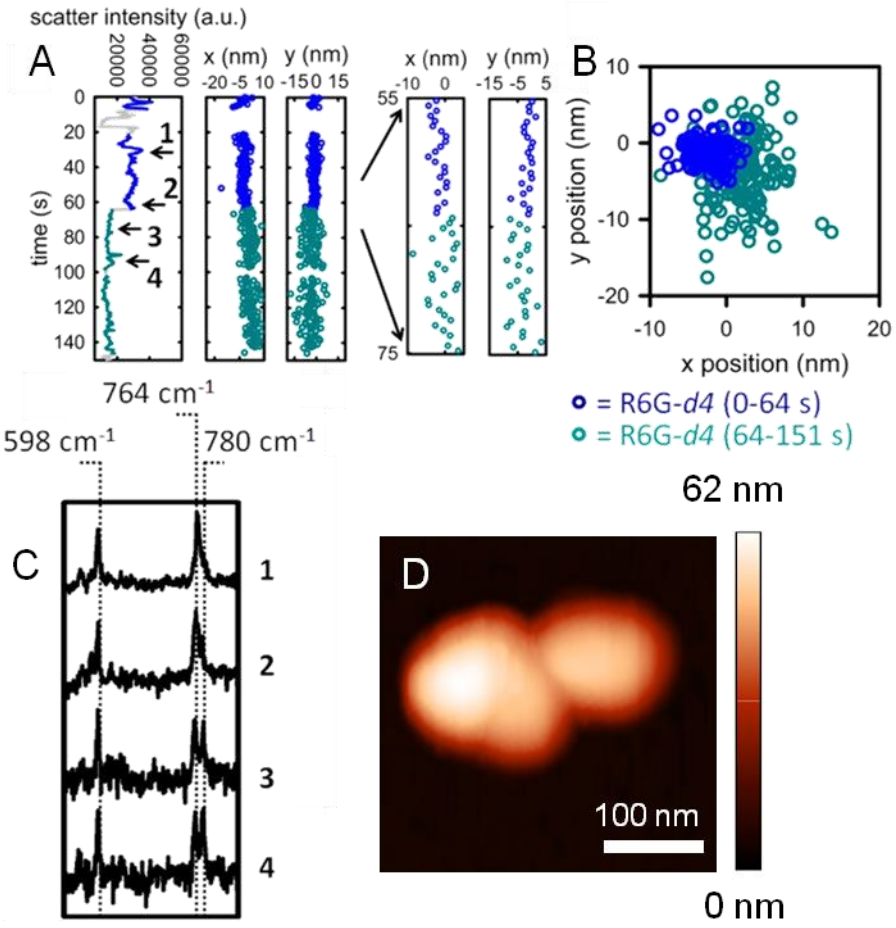

Figure 3.3. (A) Intensity time trace (left) and x and y SERS centroid trajectories (middle two columns). A zoomed-in view of the centroid positions from 55 –75 s is shown on the far right. (B) Scatter plot of the SERS centroid positions from (A). (C) Spectra taken at the indicated time points in (A) with (1) taken at 32 s, (2) taken at 60 s, (3) taken at 69 s, and (4) taken at 90 s. Color scheme for the entire figure is as follows: R6G-*d4* centroid positions corresponding to 20 – 64 s in (A) are dark blue and R6G-*d4* centroid positions corresponding to 64 – 151 s in (A) are dark cyan. (D) AFM scan of the SM-SERS active aggregate.

To explore these two mechanisms, we extend the SERS spectra to include the peak in the 764 cm^{-1} region in Figure 3.3C. This peak evolves over time, initially dominated by a single peak (spectrum 1), then showing signs of a small shoulder (spectrum 2) immediately before the intensity step occurs, and finally evolving into two

distinct peaks at 764 cm^{-1} and 780 cm^{-1} (spectra 3 and 4) during the low intensity interval. If our first mechanism (intensity drop due to multiple molecules) is correct, we would not expect a new peak to emerge in our spectra upon one of the molecules turning off. On the other hand, changes in SM-SERS peak frequencies and peak splitting are consistent with reorientation of the probe molecule.[22–27] Thus, we believe that the abrupt drop in the SERS intensity from the high to the intermediate value is associated with molecular reorientation on the surface of the nanoparticle.

If we now consider the x and y centroid positions fit during this time period (Figure 3.3A, center; Figure 3.3B), we see a gradual change in the centroid positions over the entire time interval, with the x-centroid value shifting towards more positive values and the y-centroid shifting towards more negative values. The uncertainty in the position during the high intensity interval is ~0.9 nm, while this uncertainty reaches ~1.3 nm during the low intensity interval; this change in uncertainty is reflected in the increased scatter in the centroid data during the low intensity interval. However, if we now look at the centroid positions from 55 – 75 s, which overlap with the stepwise change in SERS intensity, we find that the centroid position is stable (Figure 3.3A, right). If changes in molecular orientation lead to changes in the SERS centroid, we would expect to see a large jump in the centroid position associated with the drop in the SERS intensity. However, since the centroid remains stable, we can eliminate molecular reorientation as an explanation for changes in the SERS centroid. The stable centroid also allows us to rule out multiple molecules as an explanation for the intensity drop in this example, since our previous data in Figures 3.1 and 3.2 have shown that multiple molecules lead to changes in the SERS centroid.

3.4 Mobile emitters

Taken together, Figures 3.1 – 3.3 rule out molecular reorientation effects as the source of the changing SERS centroid and support our claim that the position of the molecule on the surface of the nanoparticle influences the location of the SERS centroid. Again, we emphasize that the centroid does not reflect the absolute position of the molecule, but reports how the nanoparticle re-radiates the Raman scattering from the molecule into the far field. In the case of a mobile single dipole, the centroid will shift as the molecule explores its local environment, consistent with our previous work.[5,8] However, the intensity of the measured SERS will be strongly influenced by the orientation of the probe molecule (Figure 3.3), which means there may not be a direct one-to-one correlation with the measured SERS intensity and the spatial origin of the signal. This observation may help explain why signals in SERS hot spots do not vary over many orders of magnitude in super-resolution images, simply due to orientational averaging effects.[5,8] These data also highlight the critical importance of working at or near the single-molecule limit when mapping out SERS hot spots using super-resolution imaging. In the case when two molecules are emitting simultaneously (as in Figure 3.2), the SERS centroid is an intensity-weighted super-position of the two emitters. In the case of stationary emitters, we can simply wait for one probe to photobleach in order to determine the spatial origin of the two centroids.[18] However, in the case of mobile emitters, this super-position effect can complicate the analysis.

To illustrate this, Figure 3.4 presents an example in which two molecules dynamically exchange within a SERS hot spot. In this example, both molecules were introduced at a concentration of 1.5 nM (~3 molecules per nanoparticle). During the first part of the time trace (Figure 3.4A), the associated spectra show a clear signature of R6G-*d0* alone (Figure 3.4B-1). However, after 16 seconds, a small shoulder appears indicating

the presence of R6G-*d4* (Figure 3.4B-2). As time progresses, the R6G-*d4* grows in to become the dominant spectral species, while the contribution from the R6G-*d0* slowly diminishes (Figure 3.4B-3 and 3.4B-4). At 43 seconds, all spectral evidence of R6G-*d0* is gone, and the spectra are exclusively R6G-*d4* (Figure 3.4B-5). This exchange in the spectra suggests slow dynamics associated with motion of the R6G-*d0* away from the hot spot and R6G-*d4* towards the hot spot.

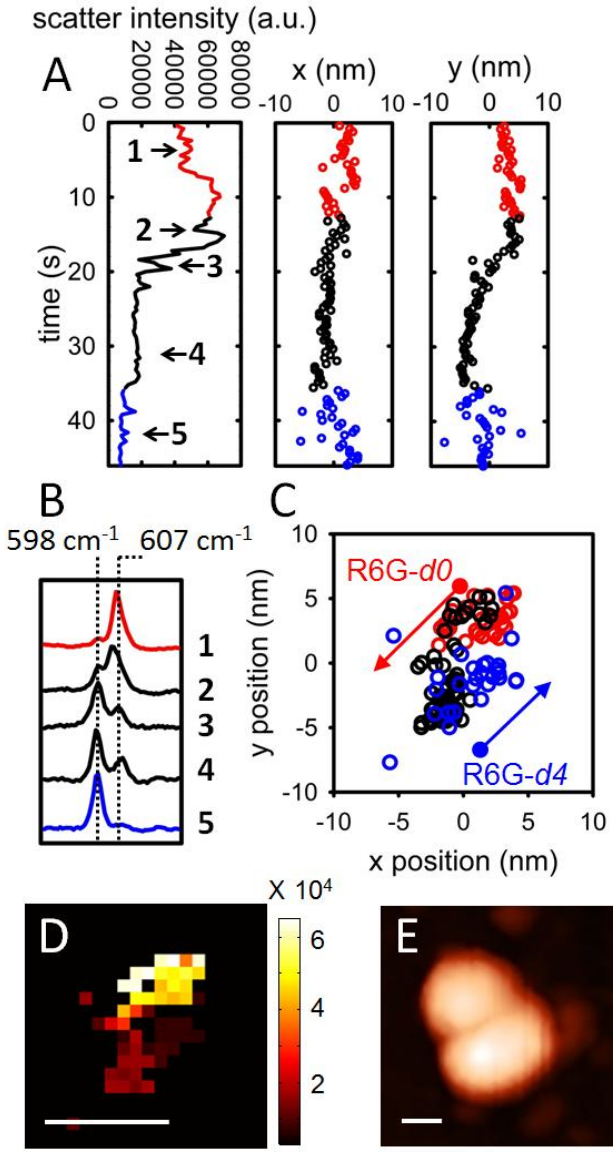

Figure 3.4. (A) Intensity time trace (left) and x- and y- SERS centroid trajectories (middle and right), colored-coded according to the identity of the emitting analyte(s): R6G-*d0* (red), R6G-*d4* (blue), and both R6G-*d0* and R6G-*d4* (black). (B) SERS spectra at the indicated times in the time trace in (A). (C) Scatter plot of all SERS centroid positions from (A) with (0, 0) set at the average value of the SERS centroid. Color corresponds to the identity of the emitting analyte(s) as in (A). (D) Spatial intensity map showing the relationship between the SERS centroid position and average intensity at that position. Bin size is 1 nm. Scale bar is 10 nm. (E) AFM image of the SERS-active nanoparticle. Scale bar is 50 nm.

If we now look at the x and y centroid fits (Figure 3.4A and 3.4C), the positions of the isolated R6G-*d0* (red points) and R6G-*d4* (blue points) appear at different locations, consistent with Figure 3.1. However, for the times when both molecules are emitting (black points), the super-position effect complicates the interpretation. In Figure 3.4C, arrows indicate the proposed trajectory of each molecule over the course of the experiment, with a circle representing the start of the trajectory and an arrowhead representing the end of the trajectory. If we first consider motion in the x-dimension, we expect the centroid value to begin at (+x) values when only R6G-*d0* is emitting. As the molecule moves towards (-x) values, its centroid contribution will shift towards (-x) values. At the same time, the R6G-d4 molecule begins moving towards the hot spot from its initial position. Because this molecule begins at (-x) values, we also expect it to contribute a (-x) centroid value. As a result, the x-centroid when both molecules are emitting is a super-position of the two (-x) values, resulting in an overall negative value of x in the centroid, as seen in Figure 3.4A (center column). As the two molecules continue to move past each other, the x-contributions from the two molecules effectively offset one another, as the x-centroid for R6G-d0 becomes more negative and the x-centroid for R6G-d4 becomes more positive. Eventually, when the R6G-d0 is completely removed from the hot spot and the R6G-d4 reaches its final position, the x-centroid is restored to a (+x) value.

Looking next at the y-dimension, we see the initial isolated R6G-*d0* has a positive y-value, while the final isolated R6G-*d4* has a negative y-value. During the intermediate times when both molecules are moving (Figure 3.4A, black data), the y-centroid smoothly moves from more positive to more negative values of y, tracking the transition in the spectra from R6G-*d0* dominance to R6G-*d4* dominance. As with the x-centroid data described above, it is clear that the centroid value is an intensity-weighted super-

position of the two SERS centroids as the two molecules exchange. One interesting feature in this data is the presence of an "excluded area" between the R6G-d0 and R6G-d4 scatter data. If the molecules are indeed moving past each other on the nanoparticle surface, then we would not expect them to occupy the same region in space, leading to discrete centroid positions associated with the position of each molecule. Although we again note that the centroid position does not reflect the absolute position of the molecule on the nanoparticle surface, this feature of the scatter plot is yet further evidence that SERS centroid is tied to the position of the molecule.

Next we spatially bin the SERS centroid positions from Figure 3.4C into 1 nm bins (which corresponds to five times our uncertainty for this data set) and calculate the total number of SERS centroids that fall into each bin. From there, we calculate the average SERS intensity of all data points within a given bin to create a spatial intensity map (Figure 3.4D), which represents the spatial distribution of the SERS intensity associated with the hot spot.[5] For this analysis, we did not exclude any data points, even though we know some SERS events originate from multiple molecules; this allows us to compare these data to previously published spatial intensity maps which were assigned to SERS from a single analyte.[5] In the example shown in Figure 3.4D, the strongest SERS intensity occurs along the upper edge of the hot spot, with a decrease in the associated intensity as the SERS centroid moves in a directional fashion away from the "hottest" region. The orientation of this high intensity edge agrees extremely well with the orientation of the junction in the associated nanoparticle dimer, shown in Figure 3.4E.

This observation is consistent with previous work, in which we noted that the SERS intensity decays in a gradient fashion as the centroid position shifts away from the "hottest" spot.[5,8] This behavior was assigned to a single molecule diffusing in a hot spot and reporting on the local electromagnetic field enhancement at different positions.[5]

Because the electromagnetic field at the nanoparticle surface decays in a gradient fashion away from the junction region, we predicted that the SERS signal would also track with this locally varying electromagnetic field, as shown in later correlated structural and optical studies.[7,8] However, in Figure 3.4D, the intensity initially decreases in gradient fashion away from the high intensity edge, but then there is a steep drop as the analyte identity switches from R6G-d0 to R6G-d4. This is due, in part, to the excluded area, but may also be due to the orientation of the R6G-d4, as described earlier. Moreover, the leftmost region of the spatial intensity map is dominated by centroid data contributed by two molecules at the same time, and therefore the SERS centroid positions corresponding to these time periods will report an intensity-weighted superposition of all emitting molecules at each time point.[18] This leads to a bias in the spatial intensity map shown in Figure 3.4D and explains the loss of smooth gradient behavior because different molecules are reporting on different regions of the spatially-varying electromagnetic field at the same time. However, even with this bias due to multiple molecules, we still see that the SERS centroid position reflects the underlying shape of the nanoparticle.

3.5 High concentration hot spot mapping

Although these data suggest that it would be favorable to use even higher concentrations of SERS tags on the nanoparticle surface in order to map out the complete hot spot, we find that above a certain threshold, the data will converge to a single location due to the super-position effect. To illustrate this point, we consider the SERS-active trimer shown in Figure 3.5A that is composed of a sphere and two rods. In this example, the SERS signal remained "on" over multiple movies and never reached a stable background, consistent with emission from multiple emitters on the surface. The integrated scatter intensity from the first acquisition is plotted against time in Figure 3.5B (left) and that of a later acquisition is plotted in Figure 3.5C (left). The correlated SERS

spectral data (not shown) show marker modes from R6G-*d4* and R6G-*d0* during both acquisitions, and we can therefore assign multiple molecule contributions to both data sets. Additionally, the spectral peaks are broader than those seen in previous examples that corresponded to "both" events, indicating there are likely more than two molecules contributing to the spectra in this example. Moreover, the PSF of this data is broadened and oriented along the long axis of the nanorod, as expected for the addition of multiple PSFs. To address this, we fit the data using both Equation 3.1 as well as a rotated, asymmetric Gaussian, which is shown in Equation 3.2

$$I(x,y) = z_0 + I_0 e^{\left[-\frac{1}{2}\left[\left(\frac{\cos^2\phi}{\sigma_x^2}+\frac{\sin^2\phi}{\sigma_y^2}\right)(x-x_0)^2+\left(\frac{-\sin(2\phi)}{\sigma_x^2}+\frac{\sin(2\phi)}{\sigma_y^2}\right)(x-x_0)(y-y_0)+\left(\frac{\sin^2\phi}{\sigma_x^2}+\frac{\cos^2\phi}{\sigma_y^2}\right)(y-y_0)^2\right]\right]} \quad (3.2)$$

The variables used to define the rotated, asymmetric Gaussian in Equation 3.2 are the same as those used in Equation 3.1, with the addition of the parameter ϕ, which defines the in-plane rotation of the Gaussian function. This PSF is used in fits to generate the data in Figure 3.5

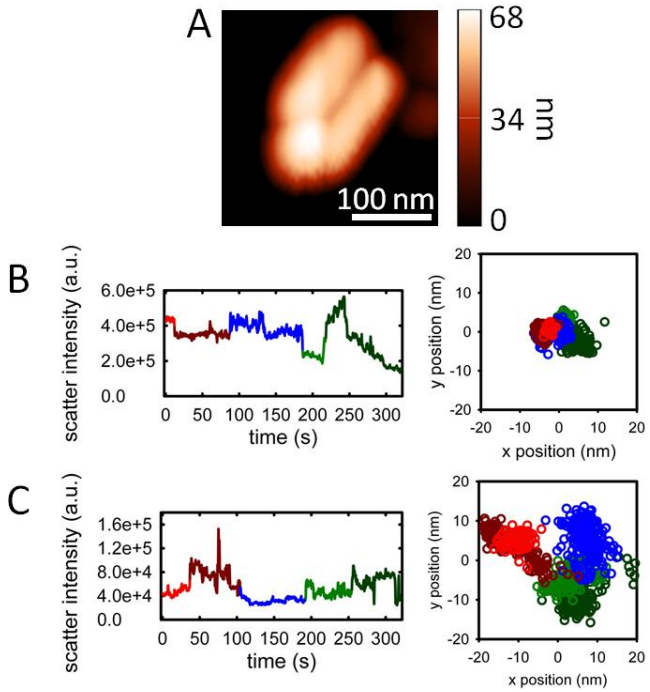

Figure 3.5. (A) AFM of a SERS-active nanoparticle trimer. (B-C) Time traces (left) showing the fluctuation of the integrated SERS intensity and the corresponding SERS centroid scatter-plots (right). (B) is the first data acquisition and (C) is a second acquisition at a later time. Color assignments in (B) and (C) are arbitrarily assigned to regions separated by intensity jumps in the time trace.

As shown in previous examples, SERS centroid positions will report an intensity-weighted super-position of the plasmon-coupled emission sites for all contributing molecules. Therefore, we arbitrarily assign the color-coding in the intensity time traces in Figure 3.5B and 3.5C according to sharp changes in the intensity to observe the spatial relationship between each intensity region. The scatter plots in the right of Figures 3.5B and 3.5C plot the SERS centroid positions for the respective time traces. The centroid positions are color-coded according to the corresponding points in the time traces. The SERS centroids in the first acquisition are confined to a region roughly ~20 x 10 nm in size and the centroids from each time interval show significant overlap (Figure 3.5B,

right). We attribute this higher degree of spatial confinement to the presence of multiple molecules contributing to each PSF, such that the SERS centroids are super-positions of multiple emitters, leading to convergence in the fits to a confined region.

On the other hand, for data acquired at a later time (Figure 3.5C), we observe that the SERS centroid locations are fit to spatially distinct positions and extend over a greater distance (~40 x 20 nm). As molecules photobleach (or diffuse out of the hot spots) in the later acquisition, the images become dominated by one (or few) molecules at a time, reducing the super-position effect and allowing distinct SERS centroids to be observed.[18] This example further highlights the fact that we cannot work too far outside the single molecule limit in super-resolution SERS imaging studies or we will simply see the average position of all emitters on the surface; this is an important point because it limits the substrates that can be studied with this approach to those that are SM-SERS active with signals that modulate in time. In the fluorescence community, this problem is addressed by using photoswitchable probes that can be actively modulated between emissive and non-emissive states.[28,29] However, in SERS, we do not have a straightforward means of modulating the signal intensity, except for probe motion in and out of the hot spot.[9] In the current data set, this motion is stochastic, driven by thermal energy due to localized laser heating, but the motion may also be suppressed if optical trapping in the hot spot is present.[30,31] As a result, controlling the signal modulation is difficult without understanding the various factors that contribute to probe mobility on the nanoparticle surface.

3.6 Quality of Gaussian PSF fitting

The data presented in this chapter has all been fit using either a 2-dimensional Gaussian, or a rotated asymmetric 2-dimensional Gaussian (Equations 3.1 and 3.2, respectively), but it is important to note that neither theoretical PSF fully accounts for the

experimentally collected emission pattern.[15,20,32,33] Figure 3.6A shows an experimentally collected image taken from the data used to generate Figure 3.5B, with the 2-dimensional Gaussian fit and residuals in Figure 3.6B and C, respectively. The residual plot is generated by taking the experimental data and subtracting off the theoretical PSF generated by the fit. In this case, it is apparent from the residuals that the 2-dimensional Gaussian fit does not account for all of the features in the experimental PSF. For this reason, we then fit the data with the rotated asymmetric 2-dimensional Gaussian function, described in Equation 3.2, in order to produce the fit and residual data shown in Figures 3.6D-E. Again we can see a non-random pattern of residuals indicating a poor fit to the model; in this case, however, we do see smaller residual values, indicating that this fit is a better match to the data than Equation 3.1. For this reason, it was used to generate the data shown in Figure 3.5.

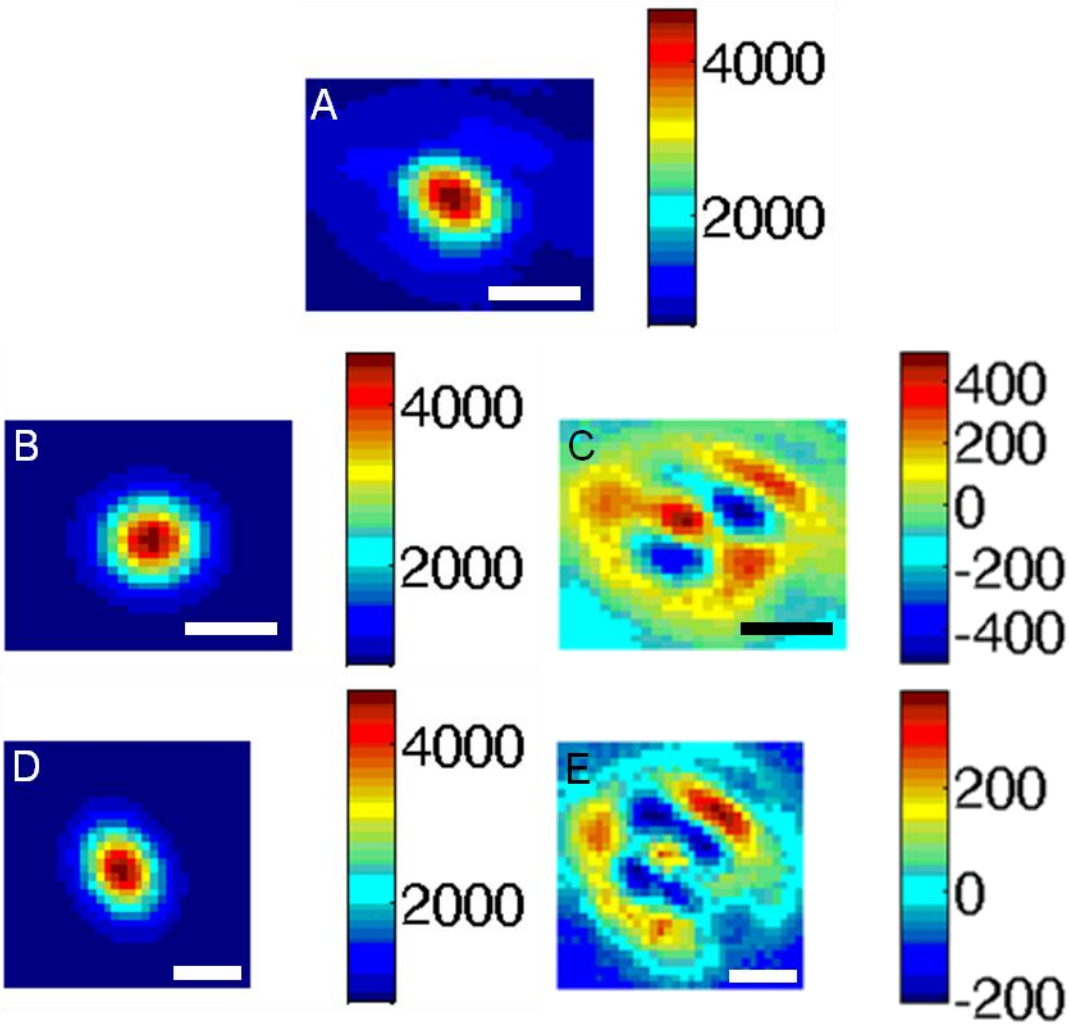

Figure 3.6. (A) Image of SERS emission from aggregate shown in Figure 3.5A. Fit data (B) and residuals of fit (C) when a 2-dimensional Gaussian is used to fit (A). Fit data (B) and residuals of fit (C) when a rotated asymmetric Gaussian is used to fit (A). Scale bars are 500 nm in all plots.

While neither of the theoretical PSFs used completely matched the experimental PSF, the results obtained from the super-resolution fitting of this data still contains useful information regarding the emission centroid location. This is because the residual pattern for each fit type remains constant for all frames collected on each aggregate, and therefore remains a source of systematic, not random, error. While the absolute positions

of the emission centroids may be different in each case, the patterns and spread of the fit data remains unchanged, which can be seen in Figure 3.7. This Figure shows this using two examples, the first in Figure 3.7A-B, which is based on the optical data used to generate Figure 3.5B. The data in Figure 3.7A-B shows the centroid localization results of using two different PSFs to fit the same data. Here we show that the relative locations of the localized centroids do not change whether the data is fit with a Gaussian PSF (Equation 3.1, Figure 3.7A) or with a rotated asymmetric Gaussian PSF (Equation 3.2, Figure 3.7B). While there is likely a difference in the absolute position of the centroids between these two fits, it is the relative positions of the localized centroids that are most useful in this work, which again remain unaffected by PSF choice. While a 2-dimensional Gaussian PSF may not account for all features of the true emission pattern, the relative centroid positions determined with this fit are identical to those from a more complicated PSF.

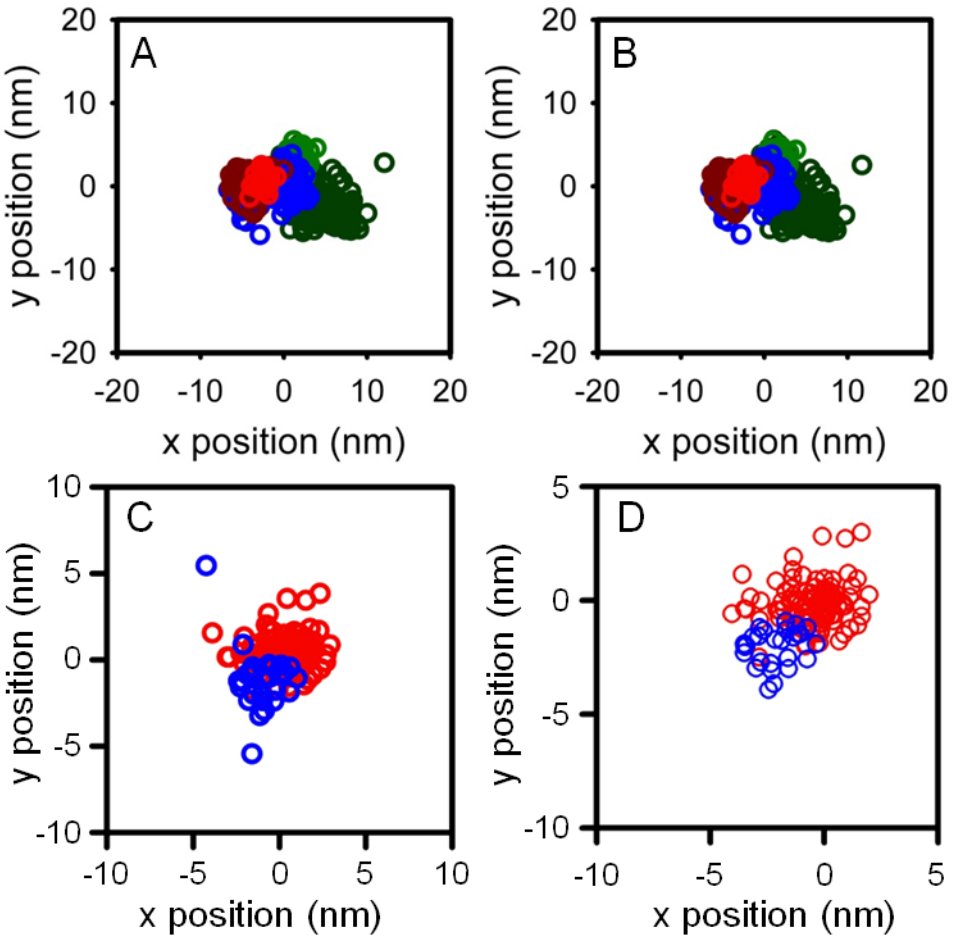

Figure 3.7. Plot of centroid positions localized using (A) Equation 3.1 (Gaussian function) and (B) Equation 3.2 (asymmetric rotated Gaussian function) for data from Figure 3.5B. Plot of SERS centroid positions from Figure 3.1 localized by fitting SERS data with Equation 3.1 (C) after subtracting background luminescence using a 2-dimensional Gaussian and (D) without background luminescence subtracted. Data in (B-C) is replicated from Figure 3.5B and 3.1B, respectively, for comparison purposes.

Another benefit coming from the robustness of the Gaussian PSF is its ability to fit SERS emission where a constant background is present. In most super-resolution SERS fitting, we fit the background luminescence of the nanoparticle aggregate with Equation 3.1, and then subtract it from frames where SERS is seen, so that the

background can be deconvoluted from the SERS emission (as in the case of Figure 3.1).[5,7] In the instances of the rest of the data shown here, the emission from the SERS active aggregates never reached a stable background level, meaning that this background could not be identified or removed *via* fitting. To address whether or not this affects the relative centroid positions of the data, we can examine the data in Figure 3.7C-D, which shows the centroid positions from the optical data in Figure 3.1 both with and without the nanoparticle luminescence background subtraction, respectively. As the data in these two plots looks nearly indistinguishable, this indicates that the presence of unsubtracted nanoparticle background does not affect the relative centroid position determined by the fit.

3.7 Conclusions

In conclusion, we have used super-resolution imaging of isotope-edited analytes to show that changes in the SERS centroid are dominated by the changing position of the molecule on the nanoparticle surface, rather than molecular reorientation or spontaneous nanoparticle emission. This result means that it is possible to track the motion of a single molecule on the surface of a SERS-active nanoparticle and map out how the local electromagnetic field is enhanced by the nanoparticle, as we had previously hypothesized. However, we have also shown that multiple molecules will lead to a super-position in the SERS centroid position, which underscores the importance of working close to the single molecule limit when trying to map out local electromagnetic field enhancements of SERS hot spots. The next question is how strongly the SERS centroid position reflects the actual position of the molecule. So far, we have discussed that the SERS centroid is a convolution between the position of the molecule and the plasmon modes of the underlying, radiating nanoparticle; however, knowing how much the SERS centroid position shifts as the position of the molecule changes is an important next step

towards relating the SERS spatial intensity maps back to nanoparticle structure. Our previous data has shown surprisingly good agreement between the spatial intensity maps and nanoparticle geometry, suggesting that the position of the molecule is a strong director of the centroid position.[7,8] However, further work—both experiment and theory—is needed to help us better understand this molecule-metal coupling in this important, yet complex, plasmonic system.

3.8 Acknowledgements

We would like to thank Spherotech for the generous gift of fluorescent nanospheres used as alignment markers and Professor Richard Van Duyne at Northwestern University for the isotopologue analytes. This work was supported by the Welch Foundation under Award No. F-1699 and the Air Force Office of Scientific Research under AFOSR Award No. FA9550-09-0112 as well as start up funds from the University of Texas at Austin.

3.9 References

(1) Camden, J. P.; Dieringer, J. A.; Wang, Y.; Masiello, D. J.; Marks, L. D.; Schatz, G. C.; Van Duyne, R. P. Probing the Structure of Single-Molecule Surface-Enhanced Raman Scattering Hot Spots. *J. Am. Chem. Soc.* **2008**, *130*, 12616–12617.

(2) Qian, X.-M.; Nie, S. M. Single-Molecule and Single-Nanoparticle SERS: From Fundamental Mechanisms to Biomedical Applications. *Chem. Soc. Rev.* **2008**, *37*, 912–920.

(3) Dieringer, J. A.; Lettan, R. B.; Scheidt, K. A.; Van Duyne, R. P. A Frequency Domain Existence Proof of Single-Molecule Surface-Enhanced Raman Spectroscopy. *J. Am. Chem. Soc.* **2007**, *129*, 16249–16256.

(4) Michaels, A. M.; Jiang; Brus, L. Ag Nanocrystal Junctions as the Site for Surface-Enhanced Raman Scattering of Single Rhodamine 6G Molecules. *J. Phys. Chem. B* **2000**, *104*, 11965–11971.

(5) Stranahan, S. M.; Willets, K. A. Super-Resolution Optical Imaging of Single-Molecule SERS Hot Spots. *Nano Lett.* **2010**, *10*, 3777–3784.

(6) Cang, H.; Labno, A.; Lu, C.; Yin, X.; Liu, M.; Gladden, C.; Liu, Y.; Zhang, X. Probing the Electromagnetic Field of a 15-Nanometre Hotspot by Single Molecule Imaging. *Nature* **2011**, *469*, 385–388.

(7) Weber, M. L.; Litz, J. P.; Masiello, D. J.; Willets, K. A. Super-Resolution Imaging Reveals a Difference between SERS and Luminescence Centroids. *ACS Nano* **2012**, *6*, 1839–1848.

(8) Weber, M. L.; Willets, K. A. Correlated Super-Resolution Optical and Structural Studies of Surface-Enhanced Raman Scattering Hot Spots in Silver Colloid Aggregates. *J. Phys. Chem. Lett.* **2011**, *2*, 1766–1770.

(9) Willets, K. A.; Stranahan, S. M.; Weber, M. L. Shedding Light on Surface-Enhanced Raman Scattering Hot Spots through Single-Molecule Super-Resolution Imaging. *J. Phys. Chem. Lett.* **2012**, *3*, 1286–1294.

(10) Thompson, R. E.; Larson, D. R.; Webb, W. W. Precise Nanometer Localization Analysis for Individual Fluorescent Probes. *Biophys. J.* **2002**, *82*, 2775–2783.

(11) Kerker, M.; Wang, D.-S.; Chew, H. Surface Enhanced Raman Scattering (SERS) by Molecules Adsorbed at Spherical Particles: Errata. *Appl. Opt.* **1980**, *19*, 4159–4174.

(12) Ausman, L. K.; Schatz, G. C. On the Importance of Incorporating Dipole Reradiation in the Modeling of Surface Enhanced Raman Scattering from Spheres. *J. Chem. Phys.* **2009**, *131*, 084708–084708–10.

(13) Weiss, A.; Haran, G. Time-Dependent Single-Molecule Raman Scattering as a Probe of Surface Dynamics. *J. Phys. Chem. B* **2001**, *105*, 12348–12354.

(14) Lee, P. C.; Meisel, D. Adsorption and Surface-Enhanced Raman of Dyes on Silver and Gold Sols. *J. Phys. Chem.* **1982**, *86*, 3391–3395.

(15) Stranahan, S. M.; Titus, E. J.; Willets, K. A. Discriminating Nanoparticle Dimers from Higher Order Aggregates through Wavelength-Dependent SERS Orientational Imaging. *ACS Nano* **2012**, *6*, 1806–1813.

(16) Yildiz, A.; Forkey, J. N.; McKinney, S. A.; Ha, T.; Goldman, Y. E.; Selvin, P. R. Myosin V Walks Hand-Over-Hand: Single Fluorophore Imaging with 1.5-Nm Localization. *Science* **2003**, *300*, 2061–2065.

(17) Andersen, P. C.; Jacobson, M. L.; Rowlen, K. L. Flashy Silver Nanoparticles. *J. Phys. Chem. B* **2004**, *108*, 2148–2153.

(18) Gordon, M. P.; Ha, T.; Selvin, P. R. Single-Molecule High-Resolution Imaging with Photobleaching. *Proc. Natl. Acad. Sci. U. S. A.* **2004**, *101*, 6462–6465.

(19) Borys, N. J.; Lupton, J. M. Surface-Enhanced Light Emission from Single Hot Spots in Tollens Reaction Silver Nanoparticle Films: Linear versus Nonlinear Optical Excitation. *J. Phys. Chem. C* **2011**, *115*, 13645–13659.

(20) Li, Z.; Shegai, T.; Haran, G.; Xu, H. Multiple-Particle Nanoantennas for Enormous Enhancement and Polarization Control of Light Emission. *ACS Nano* **2009**, *3*, 637–642.

(21) Shegai, T.; Li, Z.; Dadosh, T.; Zhang, Z.; Xu, H.; Haran, G. Managing Light Polarization via Plasmon–Molecule Interactions Within an Asymmetric Metal Nanoparticle Trimer. *Proc. Natl. Acad. Sci.* **2008**, *105*, 16448–16453.

(22) Fromm, D. P.; Sundaramurthy, A.; Kinkhabwala, A.; Schuck, P. J.; Kino, G. S.; Moerner, W. E. Exploring the Chemical Enhancement for Surface-Enhanced Raman Scattering with Au Bowtie Nanoantennas. *J. Chem. Phys.* **2006**, *124*, 061101.

(23) Barhoumi, A.; Zhang, D.; Halas, N. J. Correlation of Molecular Orientation and Packing Density in a dsDNA Self-Assembled Monolayer Observable with Surface-Enhanced Raman Spectroscopy. *J. Am. Chem. Soc.* **2008**, *130*, 14040–14041.

(24) Moskovits, M.; Suh, J. S. Surface Selection Rules for Surface-Enhanced Raman Spectroscopy: Calculations and Application to the Surface-Enhanced Raman Spectrum of Phthalazine on Silver. *J. Phys. Chem.* **1984**, *88*, 5526–5530.

(25) Papadopoulou, E.; Bell, S. E. J. Surface-Enhanced Raman Evidence of Protonation, Reorientation, and Ag+ Complexation of Deoxyadenosine and Deoxyadenosine-5′-Monophosphate (dAMP) on Ag and Au Surfaces. *J. Phys. Chem. C* **2011**, *115*, 14228–14235.

(26) Wang, Z.; Rothberg, L. J. Origins of Blinking in Single-Molecule Raman Spectroscopy. *J. Phys. Chem. B* **2005**, *109*, 3387–3391.

(27) Creighton, J. A. Surface Raman Electromagnetic Enhancement Factors for Molecules at the Surface of Small Isolated Metal Spheres: The Determination of Adsorbate Orientation from Sers Relative Intensities. *Surf. Sci.* **1983**, *124*, 209–219.

(28) Rust, M. J.; Bates, M.; Zhuang, X. Sub-Diffraction-Limit Imaging by Stochastic Optical Reconstruction Microscopy (STORM). *Nat. Methods* **2006**, *3*, 793–796.

(29) Betzig, E.; Patterson, G. H.; Sougrat, R.; Lindwasser, O. W.; Olenych, S.; Bonifacino, J. S.; Davidson, M. W.; Lippincott-Schwartz, J.; Hess, H. F. Imaging Intracellular Fluorescent Proteins at Nanometer Resolution. *Science* **2006**, *313*, 1642–1645.

(30) Hallock, A. J.; Redmond, P. L.; Brus, L. E. Optical Forces between Metallic Particles. *Proc. Natl. Acad. Sci. U. S. A.* **2005**, *102*, 1280–1284.

(31) Xu, H.; Käll, M. Surface-Plasmon-Enhanced Optical Forces in Silver Nanoaggregates. *Phys. Rev. Lett.* **2002**, *89*, 246802.

(32) Mortensen, K. I.; Churchman, L. S.; Spudich, J. A.; Flyvbjerg, H. Optimized Localization Analysis for Single-Molecule Tracking and Super-Resolution Microscopy. *Nat. Methods* **2010**, *7*, 377–381.

(33) Stranahan, S. M.; Titus, E. J.; Willets, K. A. SERS Orientational Imaging of Silver Nanoparticle Dimers. *J. Phys. Chem. Lett.* **2011**, *2*, 2711–2715.

Chapter 4: Accuracy of Super-Localization Imaging Using Gaussian and Dipole Emission Point-Spread Functions for Modeling Gold Nanorod Luminescence[2]

4.1 Introduction

While the results in the previous chapter showed that the single-molecule surface-enhanced Raman scattering (SM-SERS) centroid in silver nanoparticle (AgNP) aggregates is influenced by the position of the molecule, previous studies have indicated that the SM-SERS emission has dipolar emission characteristics that are consistent with the structure of the nanoparticles.[1–4]. Evidence of this dipolar emission can actually be seen in Figure 3.6 in the non random fit residuals resulting from the Gaussian super-resolution fitting. These residuals indicate that the true SERS emission PSF is more complicated than what can be modeled with a simple 2-dimensional Gaussian fit. To address this problem, we would like to apply a dipole emission model to our super-resolution PSF fitting (replacing the 2-dimensional Gaussian PSF), in order to improve the accuracy of the super-resolution fit, as well as to extract information about the nanostructure itself.

Dipole emission fitting has been extensively applied in single molecule fluorescence studies, where it has been shown that emission from a single dipole can cause anisotropy in the PSF, which is not captured by the 2-D Gaussian model.[5–8] Early single molecule fluorescence studies recognized that this anisotropy could be exploited to determine the 3-dimensional orientation of the emitter, especially upon slight defocusing of the image.[5–10] By modeling the dipolar emission PSF--accounting for the orientation of the emitter, the effects of any refractive index interfaces, and the imaging optics--excellent agreement between experimentally measured PSFs and the calculated patterns

[2] Reproduced in part with permission from Titus, E. J.; Willets, K. A. Accuracy of Super-Localization Imaging Using Gaussian and Dipole Emission Point-Spread Functions for Modeling Gold Nanorod Luminescence. *ACS Nano.* **2013,** *7,* 6258-6267. Copyright 2013 American Chemical Society.

were obtained.[5,6,9,10] Later work from Enderlein and Selvin showed that the centroid position determined using this more rigorous dipolar PSF model could differ from the centroid position from a 2-D Gaussian fit by more than 10 nm, depending on photon counts, numerical aperture and detector pixel size, suggesting that the dipolar PSF model would provide superior localization accuracy when fitting experimental PSF data.[11] Subsequent single-molecule super-resolution studies have further substantiated that 2-D Gaussian models can introduce significant errors in the localization accuracy of the centroid, especially for dipoles that are tilted out-of-plane relative to the sample surface.[12–14] Thus, several researchers have suggested that the dipole PSF model should be used in place of a 2-D Gaussian for fitting single-molecule fluorescence data to provide more accurate and rigorous centroid localization for super-resolution imaging.[11–13]

While the dipole-emission PSF has been successfully applied to single-molecule fluorescence, an accurate description of the emission PSF from systems involving nanoparticles can be more complicated. In the case of nanoparticle luminescence (such as the case of gold nanorods) or surface-enhanced Raman scattering (SERS), the emission is coupled out through the plasmon modes of the nanostructure.[1–4,15–19] Because dipolar plasmons are usually the strongest contributors to emission in these cases, we expect that a dipolar emission PSF could serve as an appropriate model of the experimental PSF.[1–4,19,20] However, unlike single fluorophores, which behave as single dipoles, plasmonic nanoparticles often support multiple dipole modes and may have contributions from non-plasmonic emission which can complicate the PSF.[15–18,21–24] Thus, it is important to consider different PSF models to determine which provides the best fit to the experimental data, and therefore the optimal centroid localization accuracy.

In the following study, we compare different PSF models for fitting the luminescence emission from isolated gold nanorods (AuNRs) in order to determine how each model affects the localization accuracy of the calculated centroid. We compare the results of fits using a single-dipole PSF, a multi-dipole (3-axis) PSF, and a 2-D Gaussian model. We chose AuNRs for this study because they have a strong luminescence signature that is dominated by the longitudinal plasmon mode, suggesting that a dipole PSF is an appropriate model.[15,17] Moreover, both the scattering and luminescence from this system have been previously described using single- and multi-dipole PSF models to determine the 3-dimensional orientation of single AuNRs.[15,17,20,24–27] In those studies, images were either defocused by hundreds of nanometers (or more) or the sample surface was modified to highlight the asymmetry inherent to the PSF. However, for centroid localization, we choose to work close to the microscope focus and use a standard coverslip to preserve a high signal-to-noise ratio and work closer to realistic super-resolution imaging conditions. Here, we not only obtain 3-dimensional orientation information, which we compare to the AuNR structure as determined by atomic force microscopy (AFM), but we also obtain the centroid position associated with each fit, which allows us to understand how different plasmon modes contribute to the overall PSF of AuNR emission.

4.2 Dipole emission model

For each diffraction-limited spot associated with single AuNR luminescence, three different models were used to fit the data. The first model is based upon a 2-D Gaussian, as given by Equation 4.1:

$$I(x,y) = z_0 + I_0 e^{\left[-\frac{1}{2}\left[\left(\frac{x-x_0}{s_x}\right)^2+\left(\frac{y-y_0}{s_y}\right)^2\right]\right]} \qquad (4.1)$$

In this expression, *I(x,y)* represents the intensity of the diffraction-limited spot as a function of position, z_0 is the intensity of the background, I_0 is the peak intensity of the diffraction-limited spot, s_x and s_y are the widths of the Gaussian, and x_0 and y_0 represent the centroid position. This model has been the dominant fitting approach in previous super-resolution imaging studies (see Chapter 3) exploring plasmon-mediated emission processes and will serve as a reference for the other fitting models.[21–23,28–32]

For the dipolar PSF models (both single- and multi-dipole), we modified code made available online by Jörg Enderlein.[33] This model calculates the PSF of a multi-dipole emitter at an interface, allowing for different contributions from three orthogonal dipolar axes, while taking into account refraction at the interface, how the PSF is distorted by the imaging system, and pixilation of the PSF by the detector.[9,34,35] The parameters that were fit in this experiment were the defocus of the microscope, the wavelength of emission (λ), the azimuthal and inclination angles of the longitudinal dipole mode (ϕ and θ, as defined in Figure 4.1A), intensity, background, centroid position, and the contribution of each dipole component to the total emission intensity defined through parameters κ and R as shown in Equation 4.2.

$$\mathrm{I}_{\mathrm{total}} = RI_{LM} + (1-R)\left(\frac{1+\kappa}{2} I_{TM} + \frac{1-\kappa}{2} I_{OOP}\right) \qquad (4.2)$$

In this expression, I_{LM}, I_{TM} and I_{OOP} represent the emission intensity from each orthogonal dipole component as shown in Figure 4.1B, where the longitudinal mode (LM) is defined along the longitudinal dipole axis of the AuNR, the transverse mode (TM) along the transverse axis parallel to the substrate, and the out-of-plane (OOP) axis defined perpendicular to the substrate. Because the three dipole components are fixed relative to

each other, rotating the longitudinal mode by ϕ and θ will result in a corresponding rotation of the transverse and out-of-plane dipole modes as well.

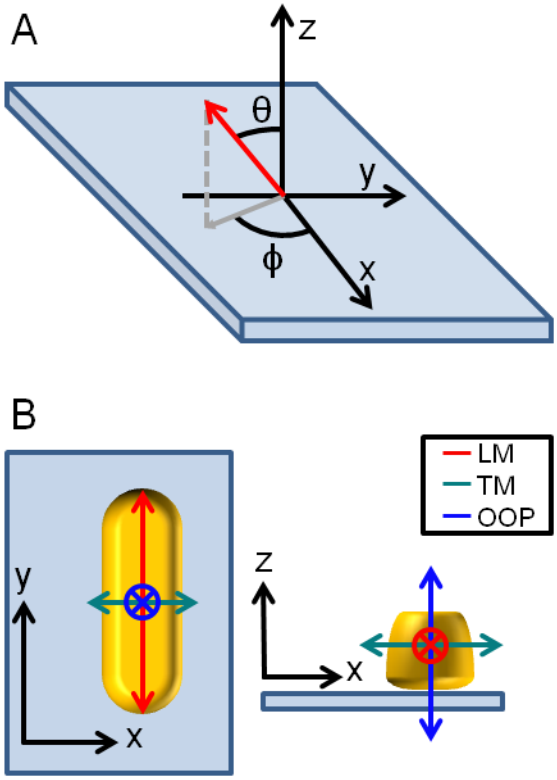

Figure 4.1. Diagram of coordinate axes relative to the sample plane (x-y) and optical axis of the microscope (z). (A) The dipole orientation angles ϕ and θ correspond to the orientation of the LM dipole mode shown in red on the AuNR in (B). (B) Definitions of the LM, TM, and OOP dipole modes relative to the coordinate axes for a nanorod with ϕ = 90°/270° and θ = 90° (the in-plane nature of the dipole makes the ϕ value symmetric along the y-axis).

Based on previous studies, AuNR luminescence is strongly coupled to the longitudinal plasmon mode of the AuNR;[15,17,36,37] this should cause the majority of emission to be polarized along the long axis of the AuNR, allowing for the possibility of fitting this emission to a single-axis dipole PSF. To explore this, we set R = 1 in Equation 4.2 and fit our data to a PSF associated with a single emitting dipole; this

single-axis dipole fit is referred to as a 1-dipole fit in the remainder of the chapter. On the other hand, although the majority of emission should be *via* the longitudinal plasmon mode of the AuNR, a small, depolarized amount of emission centered around the transverse plasmon peak has been observed in AuNR luminescence spectra as well, indicating the possible need to model the emission PSF of AuNR luminescence using a 3-axis dipole.[15,17] Previous work using defocused PSF images to probe AuNR orientation has shown that this 3-axis dipole model provides better overall fits to the data.[24,26] In this case, both R and κ are allowed to vary in our fits, in order to determine the relative contributions of each dipole mode (LM, TM, OOP) to the overall intensity. This fit is referred to as a 3-dipole fit for the remainder of this chapter. For the bulk of our studies, the 3-dipole fit will be performed by fitting emission from all three dipole modes to a single wavelength value (3-dipole, single λ), although we will also test fits in which we allow each individual dipole component to emit at its own distinct wavelength (3-dipole, multi λ).

4.3 Dipole emission fitting of single gold nanorods

In this study, AuNR samples were prepared and imaged as outlined in Chapter 2. Briefly, AuNR solution was centrifuged to remove surfactant and dropcast (along with fluorescent beads for stage drift correction) onto an alphanumerically gridded glass slide, which was coated in an aminosilane layer to immobilize the AuNRs on the surface. The luminescence of the AuNRs was excited *via* a 532 nm laser (8.8 kW/cm^2 intensity) in a widefield geometry using a 1.3 NA oil immersion objective. Luminesence signal was filtered using a dichroic/long pass filter combination and imaged onto an electron-multiplied CCD or a spectrometer. After the completion of optical experiments, the sample was transferred to a correlated optical/atomic force microscope for correlated AuNR structure measurements, as described in Chapter 2.3. Before fitting, each image

stack was corrected to remove background due to the fluorescence of the glass coverslip substrate. We then fit a small number of data frames using the Gaussian and PSF code described in Appendix 1.

To compare the accuracy of the different PSF models, we first examine the fits and residuals of two single AuNRs shown in Figures 4.2 and 4.3. The first AuNR (AuNR 1) shown in Figure 4.2 is approximately 113 nm x 38 nm (Figure 4.2A). The experimental emission image of this AuNR is shown in Figure 4.2B; this raw image is fit using each of the three models described above, and residuals are calculated by subtracting the calculated PSF fit from the experimental data. The fit (Figure 4.2C) and residuals (Figure 4.2D) using the Gaussian model (Equation 4.1) show that the Gaussian PSF approximation is a non-ideal fit for the AuNR luminescence image. Using the 1-dipole fit (Figure 4.2E), we see that the magnitude of the residuals decreases relative to the Gaussian model, but there are still strong systematic features in the residual image (Figure 4.2F). The 3-dipole model (single λ), shown in Figures 4.2G and 4.2H, produces residuals that are less than half the magnitude of the Gaussian residuals and are nearly randomly distributed across the field-of-view. Thus, the 3-dipole model (Figure 4.2G) is a better fit to the experimental data than the 1-dipole model (Figure 4.2E). This result is in agreement with previous studies, where fitting defocused images of AuNRs using a similar 3-dipole PSF algorithm yielded better fits than a 1-dipole model.[24,26] The same trend in residual patterns can be seen again in the second AuNR example (AuNR 2) shown in Figure 4.3, which shows fit and residual results for an AuNR of approximately 91 nm x 24 nm. Again we observe that the residuals are smaller and less regular as the model is changed from a 2-D Gaussian, to a 1-dipole PSF, and finally a 3-dipole PSF.

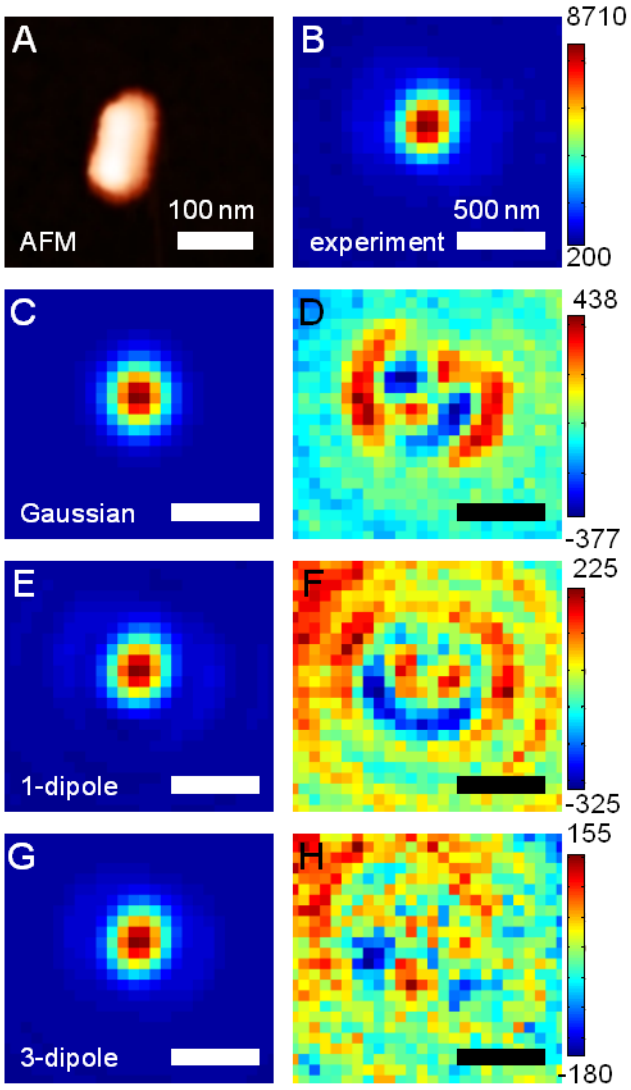

Figure 4.2. Comparison of different fits and corresponding residuals for AuNR 1. (A) AFM image of AuNR 1, with 25 nm maximum height. (B) Experimental AuNR 1 luminescence image. (C) Fit and (D) residuals of AuNR luminescence data using the 2-D Gaussian model. (E) Fit and (F) residuals using the 1-dipole PSF model. (G) Fit and (H) residuals using the 3-dipole PSF model with a single emission wavelength. Images (B) – (H) share a common 500 nm scale bar.

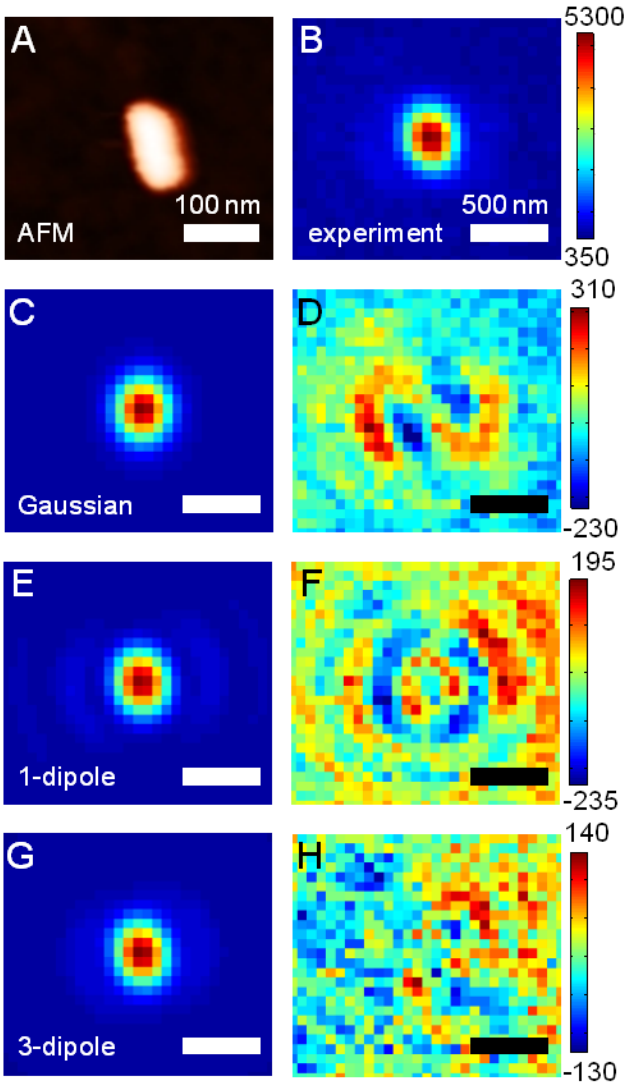

Figure 4.3. Comparison of different fits and corresponding residuals for AuNR 2. (A) AFM image of AuNR 2, with 25 nm maximum height. (B) Experimental AuNR 2 luminescence image. (C) Fit and (D) residuals of AuNR luminescence data using the 2-D Gaussian model. (E) Fit and (F) residuals using the 1-dipole PSF model. (G) Fit and (H) residuals using the 3-dipole PSF model with a single emission wavelength. Images (B) – (H) share a common 500 nm scale bar.

Selected fit results using several different PSFs on AuNR 1 are shown in Table 4.1. The 2-D Gaussian model provides the least amount of information about the AuNR 1 emission, yielding only the centroid position, but is two orders of magnitude faster than

the next fastest fit. For convenience, the average x_0 and y_0 centroid values are arbitrarily set to zero for the 2-D Gaussian fit, and all other centroid positions are reported relative to these values for comparison of centroid localization accuracy. Next, we show the parameters associated with the 1-dipole model, in which we used the experimentally measured magnification of our optical microscope as a fixed parameter during the fit (denoted 1-dipole PSF (fixed mag.) in the table). This model fits values of ϕ, θ, and λ, in addition to the centroid position. The value of ϕ agrees very well with the orientation of the longitudinal dipole mode of the AuNR, based on the AFM image in the table. However, the model suggests that the AuNR is strongly tilted out-of-plane ($\theta = 74 \pm 1°$), whereas the associated AFM data indicated that the height of AuNR 1 only varied between 39.4 and 38.1 nm from end-to-end. We also find the centroid localization is extremely different between the 1-dipole and Gaussian models, with a difference of 7 nm in the x-position and 23 nm in the y-position. Lastly, we found that the 1-dipole model vastly overestimated the wavelength of the AuNR luminescence, as shown in Figure 4.4A. While the experimentally-measured luminescence peak is at 660 nm, the 1-dipole model fits the emission at 721 ± 6 nm, which is much more red-shifted than expected.

To address this, we re-calculated the 1-dipole fit, fixing the emission wavelength at the experimentally determined maximum value of 660 nm and fitting the magnification in addition to ϕ, θ, and the centroid position (denoted 1-dipole PSF (fixed λ) in the table). Because both emission wavelength and magnification affect the size of the imaged PSF, one of the two parameters needs to be fixed or the parameters can converge to incorrect values that are well outside the expected values. We see that the centroid location and three-dimensional AuNR orientation is unchanged between the two 1-dipole fits, but the magnification is now overestimated, as expected.

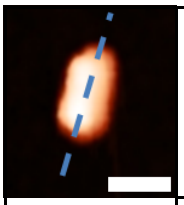

Table 4.1. Parameter values for different fitting functions applied to AuNR 1 from Figure 4.2

	ϕ (°)	**θ (°)**	**λ (nm)**	**mag.**	**Δx (nm)**	**Δy (nm)**	**fit time[a]**	**R**	**K**
2-D Gaussian	N.A.	N.A.	N.A.	N.A.	0(1)	0(2)	1 s	N.A	N.A.
1-dipole PSF (fixed mag.)	286.3(5)	74(1)	721(6)	262[b]	7(2)	-23(2)	6 min	1[b]	N.A.
1-dipole PSF (fixed λ)	286.3(5)	74(1)	660[b]	286(2)	7(1)	-23(2)	8 min	1[b]	N.A.
3-dipole PSF (single λ)	286.9(6)	85.8(7)	665(5)	262[b]	1(1)	-4(2)	18 min	0.72(5)	-0.1(3)
3-dipole PSF (multi-λ)[c]	287	85	672 (LM) 722 (TM) 693 (OOP)	262[b]	12	-4	80 min	0.8	0.4

[a]Per frame, approximate [b]Fixed parameter (experimentally measured) [c]single frame fit

The dashed line on the AFM image indicates the fit ϕ value from the 3-dipole PSF (single-λ) fit (scale bar = 100 nm).

Values in parentheses indicate the standard deviation (in the last significant digit) of the fit over 20 image frames.

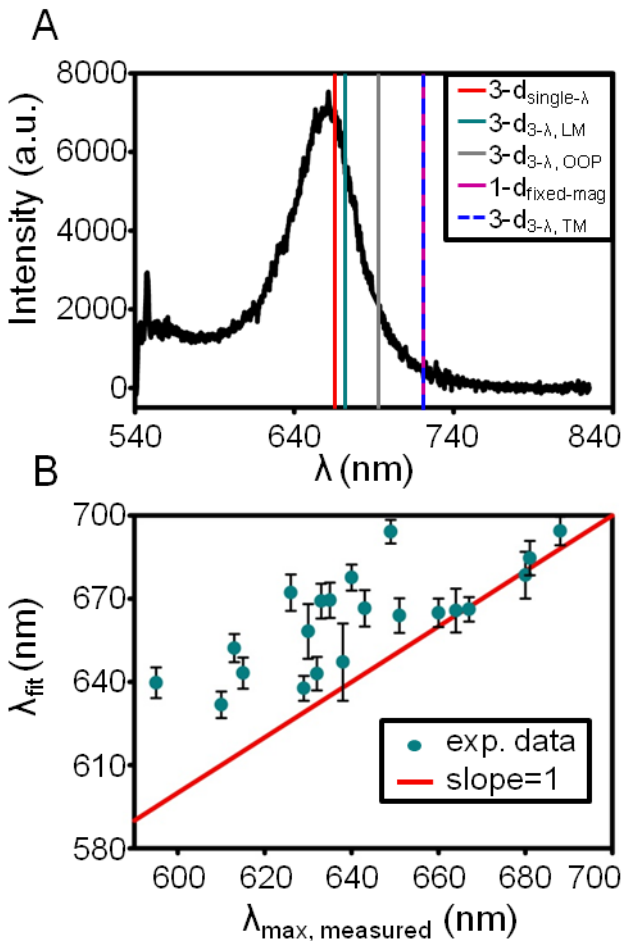

Figure 4.4. (A) Luminescence spectrum of AuNR 1 from Figure 4.2. Lines show the location of the calculated emission wavelengths for three different fits. For the 3-dipole fit where the emission wavelength of each dipole mode is fit independently, the corresponding wavelengths are indicated according to the mode assignment (LM, TM, and OOP). (B) Plot showing the relationship between the measured luminescence peak and the fitted emission wavelength using the 3-dipole PSF model of 21 AuNRs. A slope = 1 trendline is included for comparison.

Next, we show the results from the 3-dipole model, in which only a single emission wavelength was fit in addition to ϕ, θ, and the centroid position (denoted 3-dipole PSF (single λ) in the table). While the value of ϕ is essentially unchanged between the 1-dipole and 3-dipole fits, we observe that θ increases to $85.8 \pm 0.7°$ which is more

consistent with the AFM data, although still slightly out-of-plane. We also find that the calculated emission wavelength of 665 ± 5 nm is in excellent agreement with our experimental spectrum (Figure 4.4A). Based on the R value of 0.7, the emission is dominated by the longitudinal dipole mode, as expected, although there is a significant contribution from the transverse and out-of-plane modes as well. Lastly, we find that the difference between the Gaussian centroid position and 3-dipole centroid positions are quite small compared to the 1-dipole model, with differences of 1 nm and 4 nm in the x- and y-directions respectively.

In the final row of the table, we show the results of a 3-dipole model fit where the emission wavelengths for the three dipole components were allowed to vary (denoted 3-dipole PSF (multi-λ) in the table). This fit was tested because it is expected that if all of the emission is plasmon-mediated, then the transverse and out-of-plane modes would occur at shorter wavelengths than the longitudinal mode.[16,17] Based on the orientation of each axis of the 3-dipole fit, we assigned the three fit emission wavelengths to the LM, TM, and OOP components of the emission dipole (as shown in Figure 4.1B). Interestingly, all three dipole axis emission wavelengths fall to the red of both the measured luminescence peak and the 3-dipole single-λ fit (Figure 4.4A). The wavelengths determined for the TM and OOP dipole orientations are inconsistent with the expected blue-shifted wavelengths based on the results of references 16 and 17 (which show that non-longitudinal mode polarized emission should be around the wavelength of the transverse plasmon mode of the AuNR). This suggests that the AuNR shows depolarized emission that is not mediated through the TM and OOP plasmon modes, consistent with results from Motegi *et. al.*, where luminescence from AuNRs was often best fit to a 3-axis dipole, even when the wavelength of the transverse plasmon mode was well beneath the pass-band of their microscope dichroic.[24] This multi-

wavelength 3-dipole fit also yielded surprisingly poor localization accuracy, compared to the single-wavelength 3-dipole fit, particularly in the x-dimension where a difference of 12 nm was calculated. Lastly, this fit was the most computationally expensive, requiring ~80 minutes to converge to a final result.

For comparison, Table 4.2 shows the same set of parameters for the different models for AuNR 2, which is found to be completely planar with respect to the surface ($\theta \approx 90°$ for all models in Table 4.2, fits and residuals shown in Figure 4.3). From the AFM data, the height of this nanorod was 23.2 nm and 23.6 nm, at each end, consistent with a planar structure. All models (except the 3-dipole multi-λ PSF) converge to the same average centroid location, indicating that localization accuracy is not improved by using a more complex dipole PSF model instead of a simple (and computationally inexpensive) Gaussian fit. We also find that all other trends described above are maintained in this second example. For example, we find that the value of ϕ for all models matches quite well with the orientation of the AuNR, as shown in the AFM image in the table. We also find that the 3-dipole single-λ PSF model fits to an emission wavelength of 694 ± 5 nm which is in excellent agreement with the experimental peak at 695 nm, while the 1-dipole fit is dramatically red-shifted to 778 ± 4 nm.

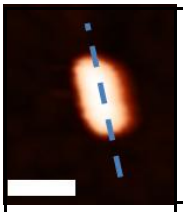

Table 4.2. Parameter values for different fitting functions applied to AuNR 2 from Figure 4.3

	ϕ (°)	**θ (°)**	**λ (nm)**	**mag.**	**Δx (nm)**	**Δy (nm)**	**fit time[a]**	**R**	**K**
2-D Gaussian	N.A.	N.A.	N.A.	N.A.	0(1)	0(2)	1 s	N.A	N.A.
1-dipole PSF (fixed mag.)	259.9(9)	89(2)	778(4)	262[b]	0(2)	0(3)	10 min	1[b]	N.A.
1-dipole PSF (fixed λ)	258.9(9)	90(2)	695[b]	293(1)	0(2)	0(2)	11 min	1[b]	N.A.
3-dipole PSF (single λ)	258.3(8)	89.8(2)	694(5)	262[b]	0(2)	0.1(9)	19 min	0.75(3)	-0.1(1)
3-dipole PSF (multi-λ)[c]	259	90	693 (LM) 635 (TM) 682 (OOP)	262[b]	-0.1	0.3	68 min	0.8	0.3

[a]Per frame, approximate [b]Fixed parameter (experimentally measured) [c]single frame fit

The dashed line on the AFM image indicates the fit ϕ value from the 3-dipole PSF (single-λ) fit (scale bar = 100 nm).

Values in parentheses indicate the standard deviation (in the last significant digit) of the fit over 20 image frames.

Since the 3-dipole (single λ) fit in the previous two examples provided the best overall agreement between the fitted wavelength and the peak in the experimental luminescence spectrum, we explored how well this model performed on other nanoparticles in our data set. In Figure 4.4B, we plot the emission wavelength fits for 21 individual AuNRs against their measured emission peak maximum. In this figure, we also include a line indicating where a relationship with a slope of one would lie in order to visualize the difference between the measured and fit values. We find that in all cases, the 3-dipole model produces an emission wavelength that either agrees with or is red-shifted relative to the actual AuNR emission with the average difference equal to 20 ± 20 nm. We also note that the wavelength fits tend to improve at longer wavelengths, where we observe much stronger agreement between our experimentally-measured and fit wavelength values. For comparison, the average emission wavelength difference for the 1-dipole PSF fit is red-shifted by 69 nm ± 10 nm from the experimental peak.

4.4 Dipole orientation parameters over many nanorods

Next, we compare the ϕ and θ estimates of the 1-dipole PSF (fixed mag) and 3-dipole (single λ) PSF models. Figure 4.5, A-D, shows histograms of the ϕ and θ estimates with both PSF models for all 59 AuNRs examined for this study. The histograms for ϕ (Figure 4.5, A and C) are distributed randomly from 0 - 360° as expected for an isotropic distribution of AuNRs on a surface. The θ values (Figure 4.5, B and D), on the other hand, are clustered towards 90°, indicating that the AuNRs are lying mostly planar on the surface. However, we find that the 1-dipole fit (Figure 4.5B) tends to pull the θ values somewhat out of plane relative to the 3-dipole fit (Figure 4.5D). Figure 4.5, E and F, plots the ϕ and θ values, respectively, for the 1-dipole fit against the ϕ and θ values for the 3-dipole fit. In the case of ϕ (Figure 4.5E), both fits show excellent agreement, as evidenced by the bulk of the fits lying on the slope = 1 trendline. On the other hand, the

θ values show relatively poor agreement, with the 1-dipole fits often showing a larger out-of-plane orientation relative to the 3-dipole fits (Figure 4.5F). Additionally, the estimation of θ when using the 1-dipole PSF is of very low precision, as shown by the large error bars in Figure 4.5F.

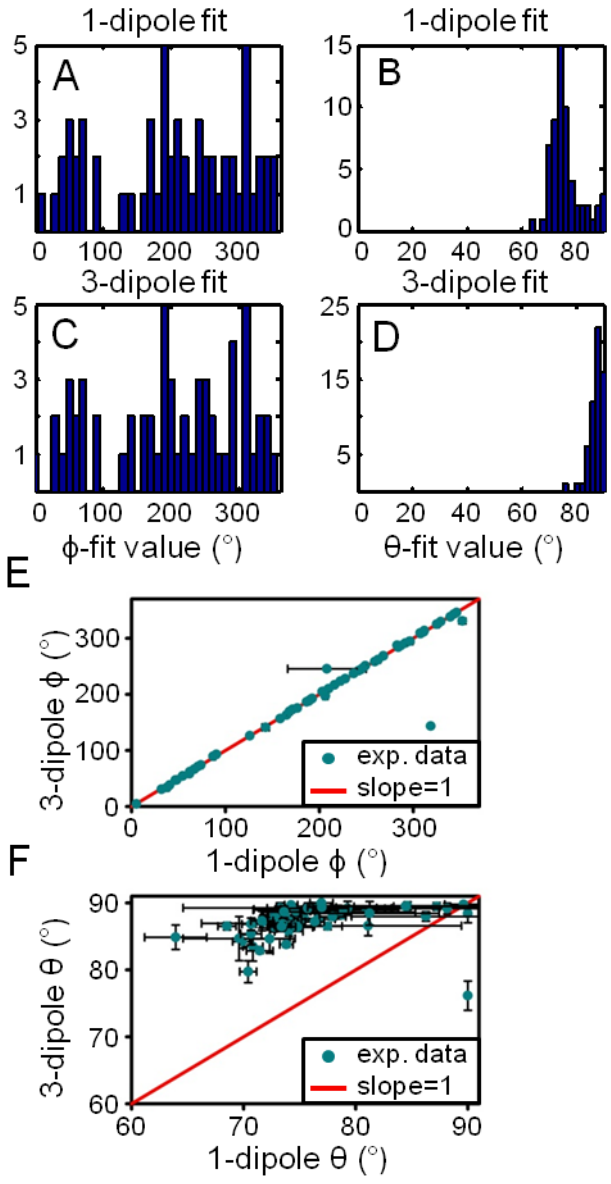

Figure 4.5. (A-D) Histograms showing fits to ϕ and θ for the 1-dipole and 3-dipole PSF super resolution fits for 59 different AuNR. (E & F) Plots showing the relationship of the ϕ values (E) and θ values (F) between the 1-dipole and 3-dipole PSF fits.

Because of the symmetry of the AuNRs used in this study, a completely in-plane nanorod could fit to two possible values of ϕ (*e.g.* ϕ_1 and ϕ_2) where $\phi_1 = \phi_2 + 180°$ (as in Figure 4.1). However, this symmetry is broken when the AuNR is out-of-plane, meaning that only one value of ϕ can accurately describe the data based on a given value of θ. For our fits, we chose an initial guess for ϕ_1 between 0 and 180° based on the orientation of the longitudinal axis of the AuNR as determined by AFM. We then fit the data a second time using ϕ_2 as the initial guess (our initial guess for θ was 90° for both fits). We found that for one initial guess of ϕ, the fitted value of θ would never move from 90°, while for the other initial guess of ϕ, the value of θ would fit to a slightly out-of-plane value (as in AuNR 1). Because the bounds for θ are defined between 0° and 90°, choosing the wrong initial guess for ϕ will not allow the fit to converge to the correct out-of-plane orientation, as the fit algorithm is unlikely to rotate the ϕ initial guess by 180° over the course of the fit. In 90% of cases where the fitted value of θ differed based on the initial guess for ϕ, we found that the average R^2 values of the fits over the 20 frames was better for the ϕ value that generated $\theta \neq 90°$. Thus, the initial guess of the in-plane orientation angle ϕ is critical for yielding the best overall fit when $\theta \neq 90°$ (note that this is not an issue in the Gaussian model, where no orientation parameters are included as initial guesses).

4.5 Localization accuracy for different fit models

Given the large disagreement in θ between the 1-dipole and 3-dipole fits shown in Figure 4.5F, we next explored how the different dipole PSF models affected centroid localization accuracy relative to the 2-D Gaussian model. For this study, we calculated the distance (in nm) between the mean Gaussian centroid position (arbitrarily set to zero) and the mean position of a dipole PSF fit as $\Delta = \sqrt{\bar{x}_{PSF}^2 + \bar{y}_{PSF}^2}$. The result is plotted against the calculated θ values for 59 different AuNRs, as shown in Figure 4.6. In the case of the 1-dipole PSF fits (Figure 4.6A), the fit centroids show a large difference from

the 2-D Gaussian fit centroids, with larger differences in Δ observed for smaller values of θ. We t-tested these data (at α=0.05) and found that 55 of 59 (93%) of the total 1-dipole centroid positions were statistically different than the 2-D Gaussian centroid locations. Next, we plotted Δ against θ for the 3-dipole fit and found that the centroids from the 3-dipole fits show much less deviation from the 2-D Gaussian centroid fits. In this case, 42 of 59 (71%) were statistically different at the 95% confidence level in the 3-dipole PSF fit. Thus, we find much better agreement between the simple, computationally inexpensive 2-D Gaussian and the more robust 3-dipole model, compared to the 1-dipole model. Importantly, this error in the centroid position is unrelated to the in-plane dipole angle, ϕ, given that we observe near identical ϕ values between the 1-dipole and 3-dipole fits (Figure 4.5E), and yet dramatically different localization accuracies.

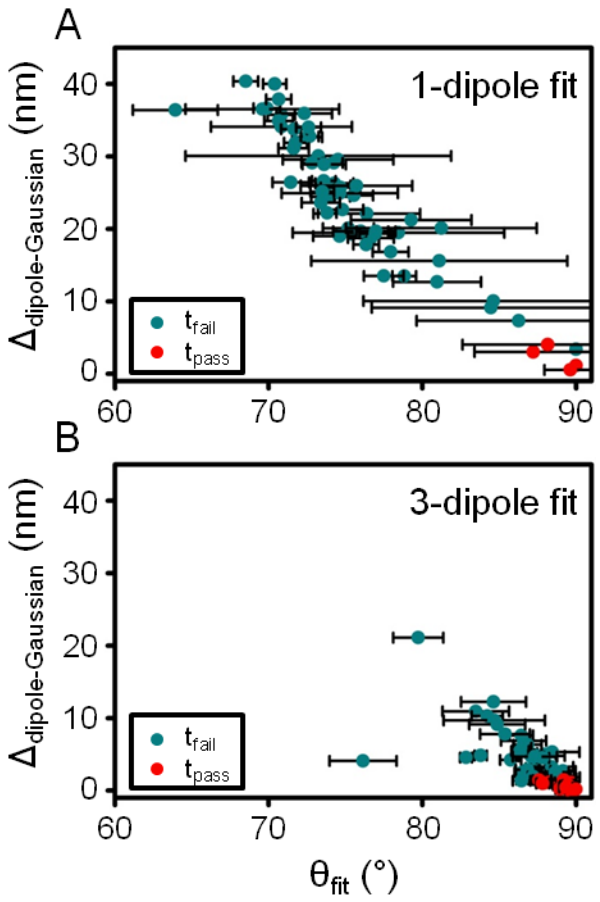

Figure 4.6. Plots showing the difference between the Gaussian centroid and the dipole PSF centroid (Δ) as a function of the fitted θ value. (A) 1-dipole PSF model. (B) 3-dipole PSF model. Colors indicate results of t-testing dipole PSF fit centroids against a 2-D Gaussian fit (t_{fail} indicates statistically different centroid populations at α=0.05, while t_{pass} indicates that the calculated centroids are the same within statistical error). Fits are shown for 59 individual AuNRs.

Our data shows that utilizing a 3-dipole PSF to fit the experimental PSF of AuNR luminescence yields the best quality fit and therefore a more accurate determination of the emission centroid. Although we tried to test whether our calculated centroid positions agreed with the relative positions of individual nanorods in the AFM images, drift in the AFM prevented an accurate comparison; thus, our conclusion that the 3-dipole PSF fit is the best model is based purely on the agreement between experimental and theoretical

results, both in the fitted values and in the associated residuals. By modeling the PSF incorrectly (*i.e.* using a 1-dipole PSF in the case of AuNRs), the accuracy of the centroid determination can be even worse than when using a 2-D Gaussian model. This result should strongly inform the use of dipole PSF fitting in future studies, in that the PSF of the emission must be well understood before the proper model can be applied. In this study, we chose a strongly anisotropic nanostructure as a test system, which is expected to behave most like a single dipole relative to other nanostructures. Even with this system, we found that the 1-dipole model yielded poor localization accuracy, which was exacerbated by under-estimation of the inclination angle θ. We believe that this error is due to a small depolarized contribution to the luminescence, which is not radiated out through the higher-energy dipolar plasmon modes of the nanorod (*e.g.* the TM or OOP modes). Given this depolarized emission, multiple dipoles were required to accurately model our experimental data, with emission fixed at a specific emission wavelength. Interestingly, Mortensen *et al.* have shown that when a diffraction-limited emitter is made up of many dipole emitters (such as a fluorophore-doped polystyrene sphere), a 2-D Gaussian will accurately describe the centroid location.[13] Our data also indicate that as more dipoles are included in the PSF model, a 2-D Gaussian shows higher overall agreement with the calculated centroid in comparison to the 1-dipole fit. This result has important implications for other plasmon-coupled emission processes, in which multiple dipole plasmon modes (possibly with different energies) may contribute to the measured emission PSF.[3,4,19] In these cases, a computationally inexpensive 2-D Gaussian may serve as a reasonable model of the emission PSF, particularly when any dominant dipolar emission modes are not oriented strongly out-of-plane. Lastly, we note that this study has focused largely on AuNRs that are oriented at fairly large values of θ relative to the substrate surface; this is due to the obvious asymmetry in the PSF which is introduced as

emitters orient further out of plane. In these cases, a 2-D Gaussian would clearly be a poor choice of fitting function for super-localization studies, based on visual inspection alone. Thus, as always, care must be taken when choosing a fitting model for any super-resolution imaging experiment, whether emission is plasmon-mediated or not.

4.6 Conclusions

In this chapter, we have applied a dipole emission PSF to the super-localization fitting of luminescence from AuNRs. The 3-dipole PSF provided the best agreement between the fitted emission wavelength and the experimentally measured luminescence spectrum, and also yielded the lowest residuals compared to the 1-dipole PSF model and the 2-D Gaussian. This fit was also able to determine the dipole orientation parameters ϕ and θ with a precision below 1° in many cases, without the need for image defocusing, and the fitted ϕ-values were in good agreement with the orientation of the AuNR as determined *via* correlated AFM imaging. Thus, a 3-dipole PSF model increases localization accuracy over both a 2-D Gaussian fit and a 1-dipole fit for this system. We have also shown that AuNR localization accuracy using the 2-D Gaussian becomes worse as the dominant longitudinal dipole moves out-of-plane relative to the substrate surface, indicating the need for more robust fitting models. Additionally, care must be taken that the correct PSF model is used, as an incorrect dipole PSF model was shown to strongly skew the localization results *via* mis-estimation of the inclination angle θ. Thus, it is critical to consider multiple dipole contributions for localizing emission from complex emitters, especially in the case of plasmon-mediated emission processes.

4.7 Acknowledgement

We would like to thank Karole Blythe for synthesizing the AuNRs used in this study, as well as Prof. Jörg Enderlein for making his "QDControl" code available freely

online. This material is based on work supported by the Welch Foundation under Award No. F-1699.

4.8 References

(1) Stranahan, S. M.; Titus, E. J.; Willets, K. A. SERS Orientational Imaging of Silver Nanoparticle Dimers. *J. Phys. Chem. Lett.* **2011**, *2*, 2711–2715.

(2) Stranahan, S. M.; Titus, E. J.; Willets, K. A. Discriminating Nanoparticle Dimers from Higher Order Aggregates through Wavelength-Dependent SERS Orientational Imaging. *ACS Nano* **2012**, *6*, 1806–1813.

(3) Shegai, T.; Brian, B.; Miljković, V. D.; Käll, M. Angular Distribution of Surface-Enhanced Raman Scattering from Individual Au Nanoparticle Aggregates. *ACS Nano* **2011**, *5*, 2036–2041.

(4) Li, Z.; Shegai, T.; Haran, G.; Xu, H. Multiple-Particle Nanoantennas for Enormous Enhancement and Polarization Control of Light Emission. *ACS Nano* **2009**, *3*, 637–642.

(5) Bartko, A. P.; Dickson, R. M. Three-Dimensional Orientations of Polymer-Bound Single Molecules. *J. Phys. Chem. B* **1999**, *103*, 3053–3056.

(6) Bartko, A. P.; Dickson, R. M. Imaging Three-Dimensional Single Molecule Orientations. *J. Phys. Chem. B* **1999**, *103*, 11237–11241.

(7) Hellen, E. H.; Axelrod, D. Fluorescence Emission at Dielectric and Metal-Film Interfaces. *J. Opt. Soc. Am. B* **1987**, *4*, 337–350.

(8) Dickson, R. M.; Norris, D. J.; Moerner, W. E. Simultaneous Imaging of Individual Molecules Aligned Both Parallel and Perpendicular to the Optic Axis. *Phys. Rev. Lett.* **1998**, *81*, 5322–5325.

(9) Böhmer, M.; Enderlein, J. Orientation Imaging of Single Molecules by Wide-Field Epifluorescence Microscopy. *J. Opt. Soc. Am. B* **2003**, *20*, 554–559.

(10) Lieb, M. A.; Zavislan, J. M.; Novotny, L. Single-Molecule Orientations Determined by Direct Emission Pattern Imaging. *J. Opt. Soc. Am. B* **2004**, *21*, 1210–1215.

(11) Enderlein, J.; Toprak, E.; Selvin, P. R. Polarization Effect on Position Accuracy of Fluorophore Localization. *Opt. Express* **2006**, *14*, 8111–8120.

(12) Lew, M. D.; Backlund, M. P.; Moerner, W. E. Rotational Mobility of Single Molecules Affects Localization Accuracy in Super-Resolution Fluorescence Microscopy. *Nano Lett.* **2013**.

(13) Mortensen, K. I.; Churchman, L. S.; Spudich, J. A.; Flyvbjerg, H. Optimized Localization Analysis for Single-Molecule Tracking and Super-Resolution Microscopy. *Nat. Methods* **2010**, *7*, 377–381.

(14) Engelhardt, J.; Keller, J.; Hoyer, P.; Reuss, M.; Staudt, T.; Hell, S. W. Molecular Orientation Affects Localization Accuracy in Superresolution Far-Field Fluorescence Microscopy. *Nano Lett.* **2011**, *11*, 209–213.

(15) Fang, Y.; Chang, W.-S.; Willingham, B.; Swanglap, P.; Dominguez-Medina, S.; Link, S. Plasmon Emission Quantum Yield of Single Gold Nanorods as a Function of Aspect Ratio. *ACS Nano* **2012**, *6*, 7177–7184.

(16) Tcherniak, A.; Dominguez-Medina, S.; Chang, W.-S.; Swanglap, P.; Slaughter, L. S.; Landes, C. F.; Link, S. One-Photon Plasmon Luminescence and Its Application to Correlation Spectroscopy as a Probe for Rotational and Translational Dynamics of Gold Nanorods. *J. Phys. Chem. C* **2011**, *115*, 15938–15949.

(17) Yorulmaz, M.; Khatua, S.; Zijlstra, P.; Gaiduk, A.; Orrit, M. Luminescence Quantum Yield of Single Gold Nanorods. *Nano Lett.* **2012**, *12*, 4385–4391.

(18) Ausman, L. K.; Schatz, G. C. On the Importance of Incorporating Dipole Reradiation in the Modeling of Surface Enhanced Raman Scattering from Spheres. *J. Chem. Phys.* **2009**, *131*, 084708–084708–10.

(19) Shegai, T.; Li, Z.; Dadosh, T.; Zhang, Z.; Xu, H.; Haran, G. Managing Light Polarization via Plasmon–Molecule Interactions Within an Asymmetric Metal Nanoparticle Trimer. *Proc. Natl. Acad. Sci.* **2008**, *105*, 16448–16453.

(20) Xiao, L.; Qiao, Y.; He, Y.; Yeung, E. S. Three Dimensional Orientational Imaging of Nanoparticles with Darkfield Microscopy. *Anal. Chem.* **2010**, *82*, 5268–5274.

(21) Stranahan, S. M.; Willets, K. A. Super-Resolution Optical Imaging of Single-Molecule SERS Hot Spots. *Nano Lett.* **2010**, *10*, 3777–3784.

(22) Weber, M. L.; Willets, K. A. Correlated Super-Resolution Optical and Structural Studies of Surface-Enhanced Raman Scattering Hot Spots in Silver Colloid Aggregates. *J. Phys. Chem. Lett.* **2011**, *2*, 1766–1770.

(23) Weber, M. L.; Litz, J. P.; Masiello, D. J.; Willets, K. A. Super-Resolution Imaging Reveals a Difference between SERS and Luminescence Centroids. *ACS Nano* **2012**, *6*, 1839–1848.

(24) Motegi, T.; Nabika, H.; Niidome, Y.; Murakoshi, K. Observation of Defocus Images of a Single Metal Nanorod. *J. Phys. Chem. C* **2013**, *117*, 2535–2540.

(25) Ha, J. W.; Marchuk, K.; Fang, N. Focused Orientation and Position Imaging (FOPI) of Single Anisotropic Plasmonic Nanoparticles by Total Internal Reflection Scattering Microscopy. *Nano Lett.* **2012**, *12*, 4282–4288.

(26) Li, T.; Li, Q.; Xu, Y.; Chen, X.-J.; Dai, Q.-F.; Liu, H.; Lan, S.; Tie, S.; Wu, L.-J. Three-Dimensional Orientation Sensors by Defocused Imaging of Gold Nanorods through an Ordinary Wide-Field Microscope. *ACS Nano* **2012**, *6*, 1268–1277.

(27) Wackenhut, F.; Virgilio Failla, A.; Züchner, T.; Steiner, M.; Meixner, A. J. Three-Dimensional Photoluminescence Mapping and Emission Anisotropy of Single Gold Nanorods. *Appl. Phys. Lett.* **2012**, *100*, 263102–263102–4.

(28) Blythe, K. L.; Mayer, K. M.; Weber, M. L.; Willets, K. A. Ground State Depletion Microscopy for Imaging Interactions between Gold Nanowires and Fluorophore-Labeled Ligands. *Phys. Chem. Chem. Phys.* **2013**, *15*, 4136–4145.

(29) Lin, H.; Centeno, S. P.; Su, L.; Kenens, B.; Rocha, S.; Sliwa, M.; Hofkens, J.; Uji-i, H. Mapping of Surface-Enhanced Fluorescence on Metal Nanoparticles Using Super-Resolution Photoactivation Localization Microscopy. *ChemPhysChem* **2012**, *13*, 973–981.

(30) Zhou, X.; Andoy, N. M.; Liu, G.; Choudhary, E.; Han, K.-S.; Shen, H.; Chen, P. Quantitative Super-Resolution Imaging Uncovers Reactivity Patterns on Single Nanocatalysts. *Nat. Nanotechnol.* **2012**, *7*, 237–241.

(31) Cang, H.; Labno, A.; Lu, C.; Yin, X.; Liu, M.; Gladden, C.; Liu, Y.; Zhang, X. Probing the Electromagnetic Field of a 15-Nanometre Hotspot by Single Molecule Imaging. *Nature* **2011**, *469*, 385–388.

(32) Titus, E. J.; Weber, M. L.; Stranahan, S. M.; Willets, K. A. Super-Resolution SERS Imaging beyond the Single-Molecule Limit: An Isotope-Edited Approach. *Nano Lett.* **2012**, *12*, 5103–5110.

(33) Enderlein, J. Imaging of Single Molecules http://www.joerg-enderlein.de/imagingOfSingleMolecules.html (accessed May 3, 2013).

(34) Patra, D.; Gregor, I.; Enderlein, J.; Sauer, M. Defocused Imaging of Quantum-Dot Angular Distribution of Radiation. *Appl. Phys. Lett.* **2005**, *87*, 101103–101103–3.

(35) Patra, D.; Gregor, I.; Enderlein, J. Image Analysis of Defocused Single-Molecule Images for Three-Dimensional Molecule Orientation Studies. *J. Phys. Chem. A* **2004**, *108*, 6836–6841.

(36) Dulkeith, E.; Niedereichholz, T.; Klar, T. A.; Feldmann, J.; von Plessen, G.; Gittins, D. I.; Mayya, K. S.; Caruso, F. Plasmon Emission in Photoexcited Gold Nanoparticles. *Phys. Rev. B* **2004**, *70*, 205424.

(37) Varnavski, O. P.; Goodson, T.; Mohamed, M. B.; El-Sayed, M. A. Femtosecond Excitation Dynamics in Gold Nanospheres and Nanorods. *Phys. Rev. B* **2005**, *72*, 235405.

Chapter 5: Superlocalization Surface-Enhanced Raman Scattering Microscopy: Comparing Point Spread Function Models in the Ensemble and Single-Molecule Limits[3]

5.1 Introduction

In the previous chapter, we showed that a dipole emission PSF could be used to accurately fit the emission of single gold nanorods (AuNRs), giving improved localization accuracy over the 2-dimensional Gaussian fit, while also giving the orientation and emission wavelength of the structure.[1] In that study, the dipole PSF fitting technique was used on AuNRs because previous research had shown that the longitudinal dipole plasmon strongly dictates the luminescence emission of the nanostructure.[2,3] Even though this mode is dominant, we found that we still needed to account for the contribution of multiple emitting dipole modes in order to obtain an accurate fit. After using this case study to understand the benefits and limitations of this fitting technique, we now move on to applying this technique to more complex nanostructures, such as single-molecule surface-enhanced Raman scattering (SM-SERS) substrates.

In the case of SERS-active nanoparticle dimers, most of the emission is coupled out through the longitudinal dipole plasmon mode of the nanostructure, suggesting that a dipole PSF might also be an appropriate model for fitting emission from these types of structures.[4–7] In previous work, we have shown excellent qualitative agreement between the SM-SERS emission from a nanoparticle dimer and a calculated dipole PSF based upon the 3-dimensional orientation of that dimer.[6] Shegai *et al.* have shown similar qualitative agreement between a Fourier plane image of SERS emission from a nanoparticle dimer and a calculated dipole PSF, again using geometric parameters from the nanostructure to define the three-dimensional orientation of the calculated dipole

[3] Reproduced in part with permission from Titus, E. J.; Willets, K. A. Superlocalization Surface-Enhanced Raman Scattering Microscopy: Comparing Point Spread Function Models in the Ensemble and Single-Molecule Limits. *ACS Nano.* **2013,** *7,* 8284-8294. Copyright 2013 American Chemical Society.

emitter.[7] However, these studies have not attempted to actually fit the experimental emission pattern to a dipole PSF, which would not only provide a quantitative evaluation of the appropriateness of the dipole PSF model, but also calculate the centroid position and the three-dimensional orientation of the best-fit dipole, which could then be compared to the actual nanoparticle structure. Such a study would be especially informative when comparing the emission patterns from SERS-active nanoparticle dimers in the regimes of both high analyte concentration (where we expect the SERS emission to couple to all resonant plasmon modes in the dimer, reducing the influence of the molecule on the PSF shape) and the single molecule level (where the position of the molecule can impact plasmon coupling and therefore the site of the SERS emission).[8,9]

In the current study, we have applied a dipolar PSF fitting algorithm to model SERS emission from dye-labeled silver nanoparticle dimers to extract the centroid position as well as other geometric parameters of the SERS emitter (which is again a dependent on both the analyte molecule and the nanoparticle structure). We have imaged dimers covered with a high concentration of SERS reporter dyes (multi-molecule SERS, or MM-SERS) as well as SM-SERS active nanoparticle dimers. In addition to fitting the experimental emission patterns to a single dipole PSF, we have also fit the data to the sum of three mutually orthogonal dipoles in order to account for other dipolar plasmon modes that may interact with the molecule on the surface. In the work shown in Chapter 4, we found that three dipole modes were necessary to provide the optimum fit—and thus best localization accuracy—to luminescence from gold nanorods, suggesting that a similar three dipole approach might also be appropriate for these studies.[1] The various dipole PSF fits are compared to the standard 2-D Gaussian model in order to compare the fit centroids and precision between the different models.

5.2 Dipole emission model

The 2-D Gaussian used for fitting SERS emission is shown in Equation 5.1.

$$I(x,y) = z_0 + I_0 e^{\left[-\frac{1}{2}\left[\left(\frac{x-x_{0G}}{s_x}\right)^2+\left(\frac{y-y_{0G}}{s_y}\right)^2\right]\right]} \qquad (5.1)$$

Each experimental diffraction-limited image is fit to Equation 5.1 to extract z_0 (background intensity), I_0 (peak intensity), x_{0G}, y_{0G} (x and y Gaussian fit centroid positions), and s_x and s_y (the widths of the Gaussian in the x and y directions), for a total of 6 fit parameters.[9–11]To generate the dipole PSF for the SERS fitting, we utilized a modified version of Jörg Enderlein's "QDControl.m" code, which is freely available online.[12] This algorithm generates a theoretical PSF based on a dipole emitter with up to 3 mutually orthogonal dipole components, and calculates the PSF based on the dipole component strengths, the orientation and position of the emitter, as well as the dielectric environment and microscope imaging parameters. When fitting data to this model, we fix as many known or experimentally verifiable parameters as possible, including microscope magnification, numerical aperture (NA) of the objective, refractive index of the coverslip and immersion medium, detector pixel size and coverslip thickness. The parameters that are fit (unless otherwise noted) include the microscope focus, the emission wavelength (λ), the orientation of the longitudinal dipole mode (φ and θ, see Figure 5.1), the dipole-fit centroid position of the dipole emission (x_{0D}, y_{0D}), the background and peak emission intensity, the distance of the emitter from the coverslip (z), as well as the values κ and R, which define the relative contribution of each dipole axis component, as described below in Equation 5.2.

$$I_{total} = RI_{LM} + (1-R)\left(\frac{1+\kappa}{2}I_{TM} + \frac{1-\kappa}{2}I_{OOP}\right) \qquad (5.2)$$

In Equation 5.2, I_{total} represents the total dipole emission vector, and I_{LM}, I_{TM}, and I_{OOP} represent unit vectors along each dipole axis (representing the longitudinal, transverse and out-of-plane modes, respectively), as depicted in Figure 5.1. For nanoparticle dimers, the longitudinal plasmon mode is approximated as the line connecting the centers of the two nanoparticles, which is expected to dominate the SERS emission.[4–7] As shown in Figure 5.1A, the longitudinal mode is defined by the orientational parameters φ and θ. We define the transverse dipole mode as perpendicular to the longitudinal mode and parallel to the plane of the coverslip, and the out-of-plane mode as perpendicular to both the longitudinal and transverse modes.

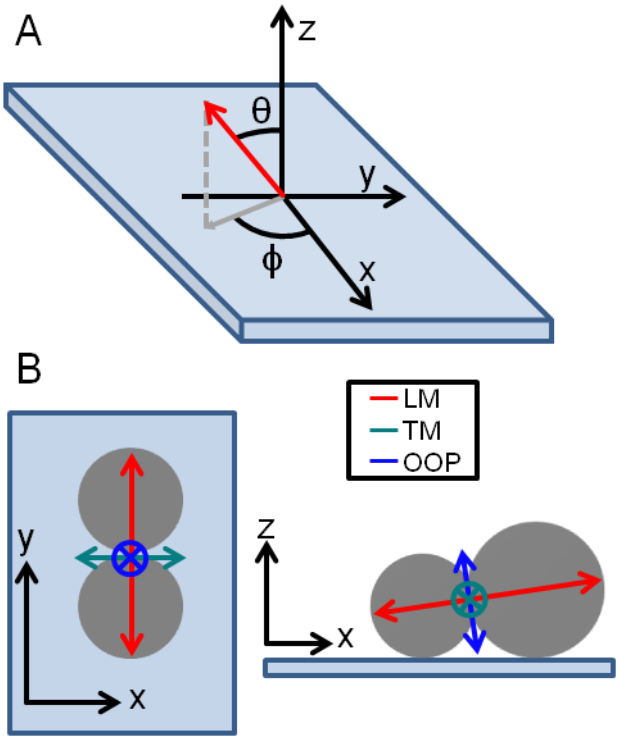

Figure 5.1. Orientation of axes used to define the dipole modes relative to the substrate. (A) Diagram showing how angles φ and θ define the longitudinal dipole mode. (B) Diagrams showing the definition of the longitudinal (LM), transverse (TM) and out-of-plane (OOP) modes relative to nanoparticle structure. LM is estimated to lie along the center-to-center line of the nanoparticles.

5.3 Dipolar emission from MM-SERS samples

Samples of silver nanoparticle dimer aggregates labeled with rhodamine 6G (R6G) (or its deuterated analog, R6G-d4) were prepared as described in Chapter 2, with the MM-SERS samples containing roughly 200 R6G molecules/aggregate and the SM-SERS samples containing roughly 2 dyes per aggregate; SM-SERS behavior was confirmed *via* on-off intensity fluctuations and a bi-analyte approach (see Chapter 2).[13,14] Optical data was collected using an inverted optical microscope with 532 nm laser excitation in a widefield geometry. Dark-field scattering was used to measure the localized surface plasmon resonance (LSPR) of selected nanostructures after SERS imaging. The sample was then transferred to an atomic force microscope (AFM) coupled to an optical microscope in order to confirm that the nanoparticle aggregates are dimers and to determine their 3-dimensional structure. Fitting was carried out using protocols outlined in Chapter 4 and Appendix 1.

We began by looking at MM-SERS samples, where we expect the geometric features of the nanoparticle to dominate the emission pattern.[7] Figure 5.2 shows an example of a SERS-active dimer (Figure 5.2A) and its associated SERS emission pattern (Figure 5.2B). The emission pattern is dominated by a bright central lobe, but there are low intensity side lobes oriented parallel to the long axis of the dimer, indicative of dipolar behavior.[6,15–17] Fitting the emission pattern to the 2-D Gaussian in Equation 5.1 (Figure 5.2C), we find that this simple model fails to capture all of the features of the SERS emission pattern, particularly the low intensity side lobes, as seen in the systematic error in the calculated residuals shown in Figure 5.2D.

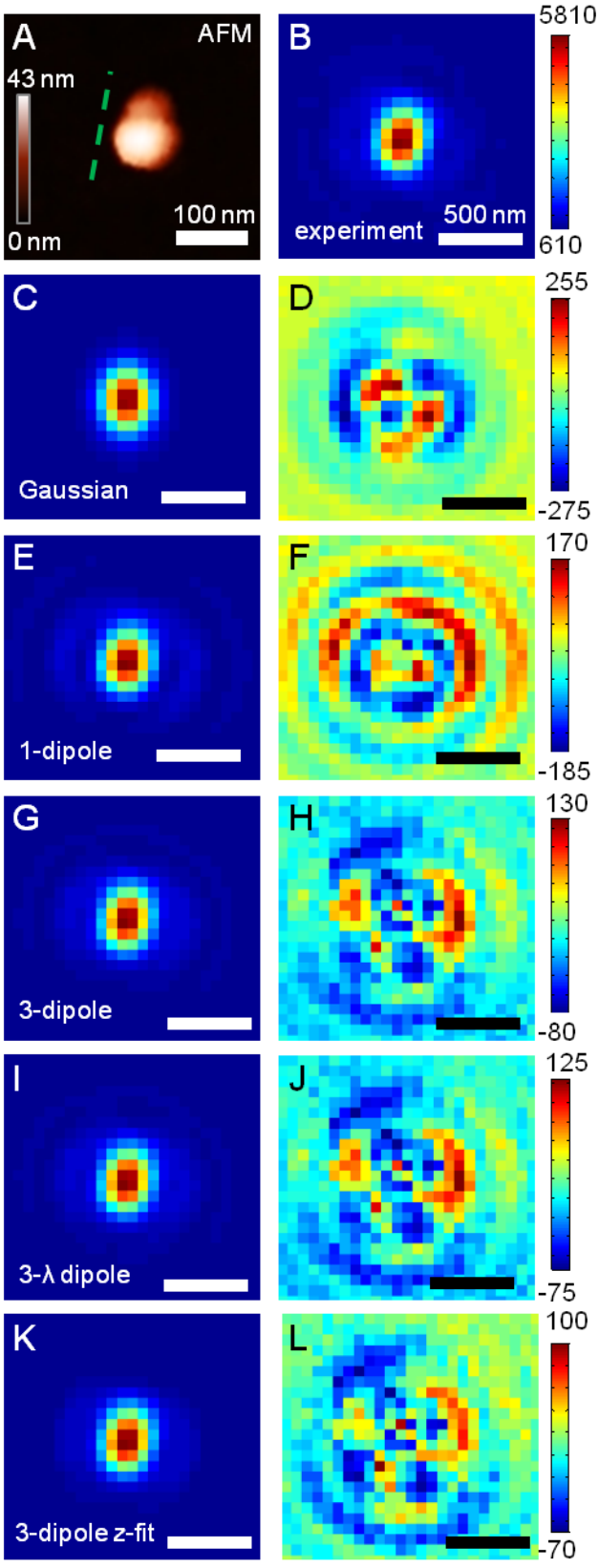

Figure 5.2. (A) AFM structure of nanoparticle dimer, where the green line indicates the φ value of the 3-dipole fit. (B) Experimental MM-SERS intensity image. (C-L) Fits (left) and residuals (right) for the different PSF models as indicated.

Next, we fit the data to a single-axis dipole (fixing R = 1 in Equation 5.2 and assuming the emission originates at the surface, z = 0), which we refer to as a 1-dipole fit, shown in Figure 5.2E. In previous work, this model has shown excellent qualitative agreement between experimental emission patterns and a single dipole PSF.[6,7] Qualitatively, the 1-dipole fit better accounts for the shape of the experimental PSF, especially the low intensity side lobes. We also obtain values for φ and θ (Table 5.1) which show reasonable agreement with the orientation and out-of-plane tilt of the longitudinal mode of the SERS-active dimer, the estimation of which is based on a line connecting the nanoparticle centers (Figure 5.2A and 5.3A, respectively). However, the 1-dipole fit also exhibits non-random residuals, as evidenced in Figure 5.2F. This observation is consistent with the study on gold nanorods shown in Chapter 4, where a 1-dipole fit was insufficient for modeling the PSF due to the presence of non-LM polarized emission.[1] Moreover, we find that the calculated emission wavelength of 661 ± 7 nm is well to the red of both the SERS and the LSPR spectra of the sample (Figure 5.3B), indicating that this model is insufficient to capture all of the properties of the SERS emission from the nanoparticle dimer.

Table 5.1. Parameter values for different fitting functions applied to the MM-SERS example from Figure 5.2

	φ (°)	**θ (°)**	**λ (nm)**	**Δx (nm)[a]**	**Δy (nm)[a]**	**fit time[b]**	**R**	**K**	**z**
2-D Gaussian	N.A.	N.A.	N.A.	0.0(5)	0.0(4)	1 s	N.A	N.A.	N.A.
1-dipole PSF	279.8(9)	77.6(6)	661(7)	1.9(5)	-10(1)	7 min	11[c]	N.A.	00[c]
3-dipole PSF (single-λ)	280.0(9)	85.3(2)	602(2)	0.5(5)	-2.5(4)	15 min	0.82(2)	-0.7(1)	00[c]
3-dipole PSF (multi-λ)[d]	281	83	597 (LM) 540 (TM) 586 (OOP)	0.8	-1.9	71 min	0.8	-0.05	00[c]
3-dipole z-fit PSF	278 (1)	83.3(5)	573(4)	0.0(5)	-0.3(4)	25 min	0.82(3)	-0.21(7)	74(8)

[a] $\Delta x(\Delta y)$ corresponds to $(x(y)_{0D}\text{-}x(y)_{0G})$ for each type of fit [b] Per frame, approximate [c] Fixed parameter [d] Single frame fit

Values in parentheses indicate the standard deviation of the fit in the last significant figure over 20 image frames.

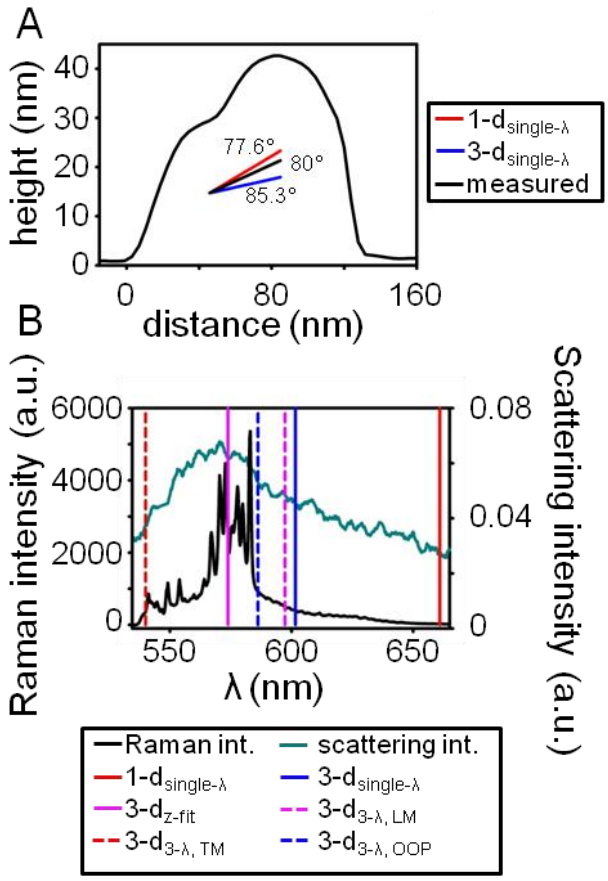

Figure 5.3. (A) AFM cross-section along the φ axis of the nanoparticle dimer from Figure 2. The red and blue lines show the θ values from the 1-dipole and 3-dipole fits, with the black line indicating the measured θ value. (B) Nanoparticle scattering (cyan) and Raman (black) spectra corresponding to the nanoparticle from Figure 2 with emission wavelength fit estimates overlaid. In the case of the 3-λ dipole fit, each wavelength is represented separately.

To account for the possibility of any emission coupling through the transverse or out-of-plane modes of the nanoparticle aggregate, a 3-axis dipole model was used, in which both R and κ from Equation 5.2 were included as fit parameters. For our first fit, we assumed a single emission wavelength, given that this model performed best when modeling luminescence from a gold nanorod, despite failing to capture the fact that the LM, TM, and OOP mode have different resonances.[1] Figure 5.2, G-H, show the results

of the fit and associated residuals, and we find that this model exhibits smaller residuals than the 1-dipole and Gaussian fits, indicating that including contributions from each dipole axis is important in modeling the correct PSF. This model also provides values for φ and θ (Table 5.1) which are in reasonable agreement with the geometry of the dimer (Figure 5.2A and 5.3A). However, the residuals in Figure 5.2H remain non-random, which tells us that this model is also imperfect at representing the SERS emission from a nanoparticle dimer. This conclusion is further supported by the wavelength fit value of 602 ± 2 nm, which is still more to the red than the bulk of the SERS emission as well as the LSPR maximum (Figure 5.3B).

Given that each dipole mode (LM, TM, and OOP) is expected to have a unique plasmon resonance, we next fit the data to a 3-axis, 3-wavelength dipole, where each dipole component has its own associated emission wavelength (denoted 3-λ dipole, Figure 5.2I-J).[18,19] Interestingly, the residuals are nearly identical between the 3-dipole (single-λ) fit in Figure 5.2H and the 3-λ dipole fit in Figure 5.2J, showing that even if we allow the wavelengths to be fit independently, we do not observe a significant improvement in the overall quality of fit. Comparing the calculated emission wavelengths of the three dipole modes (Figure 5.3B), we find that both the TM and OOP mode are blue-shifted of the LM emission, as expected. However, the TM wavelength runs into our lower wavelength limit of 540 nm, which was set based on the cutoff wavelength of our longpass filter. Moreover, the LM emission wavelength fit remains too far to the red of the actual emission, indicating that this model does not provide a significant improvement over the single-λ analog.

As a final test, we reran the 3-dipole fit with a single emission wavelength, but this time included the distance of the emitter from the surface as a fit parameter (denoted 3-dipole z-fit). We had set this value to z = 0 for all previous fits, but we recognized that

the emission might be offset from the surface, based on the geometry of the nanoparticle dimer. The fit and residuals for this model are shown in Figure 5.2, K-L; again, we observe the same systematic error in the fit residuals, although the magnitude of the residuals is smaller than the other 3-dipole cases. Interestingly, the emission wavelength that was fit using this model shows excellent agreement with the strongest SERS emission as well as the LSPR of the nanoparticle dimer (Figure 5.3B). Moreover, the calculated three-dimensional orientation once again agrees very well with the geometry of the nanoparticle dimer. However, we note that the surface offset, z, was fit to a value of 74 ± 8 nm, which is larger than the actual height of the nanoparticles, as shown in Figure 5.3A. We also find that allowing the z-value to be included as a fit parameter leads to non-convergence of several of our fits (4 out of 20 frames do not converge). One possible explanation for this lack of convergence is the inclusion of too many fit parameters, which simply creates too large of a parameter space for our fits to ultimately reach a global minimum. However, we do not have this same convergence issue in the 3-λ case, where we have two additional fit parameters over the case in which an offset is included. A second possible explanation for the poor convergence is that the model assumes that the emission is traveling through a uniform refractive index environment (air) from its offset height z to the coverslip surface, which is most likely a naïve assumption given the presence of the silver nanoparticle at the surface, as well as the possible presence of condensed water due to ambient humidity.[13]

The results of the different fits used on this MM-SERS sample are compiled in Table 5.1. For all of the dipole fits, the φ values are within several degrees of each other and agree well with the orientation of the longitudinal axis of the dimer. The θ values show slightly more variation, although they converge near the measured θ value of 80º, as shown in Figure 5.3A. Thus, the various dipole fits perform reasonably well in

predicting geometric parameters for the MM-SERS case. Moreover, all of the 3-dipole fits show R-values of ~0.8, indicating that the bulk of the emission (~80%) is dominated by the longitudinal dipole mode, as expected.

The results of a 2-D Gaussian fit are presented in the top row of Table 5.1 for comparison, and the average Gaussian centroid position is set to 0 in both x and y, with all other dipole centroid positions reported relative to the Gaussian centroid (*i.e.* x_{0D}-x_{0G}). While there is variation in the calculated centroid positions, we observe that the worst agreement with the Gaussian centroid occurs for the 1-dipole case, which we also found was a poor model for representing the data. For the 3-dipole z-fit model, we find that the centroid position actually agrees (within error) with the Gaussian, which is encouraging given that this model also yielded the best wavelength agreement. However, as discussed above, this model also yielded a non-physical value for the surface offset, had poor convergence statistics, and is computationally expensive. The single and multi-wavelength variants of the 3-dipole fit both show a slight shift from the Gaussian centroid, with calculated distances of 2.5 nm and 2.1 nm, respectively. Previous work has shown that as θ decreases from 90º, the calculated distances between the Gaussian and dipole centroids increases.[1,20–22] Interestingly, for our previous gold nanorod work (Chapter 4), we found that a θ value of 85º (as calculated here for the 3-dipole fit) would lead to a centroid shift of nearly 10 nm between the Gaussian and 3-dipole models, well above what is calculated here.[1] Thus, we find that using a Gaussian model to fit the MM-SERS emission leads to much smaller standard centroid standard deviations with respect to the more rigorous (and computationally expensive) 3-dipole fits compared to other plasmon-mediated emission processes. Lastly, we note that in all cases where multiple image frames were fit, the standard deviation in the centroid position is ≤ 0.5 nm (except

for the 1-dipole model), indicating that the SERS centroid is immobile in the MM-SERS regime.

5.4 Dipolar emission from SM-SERS samples

We next proceed to an SM-SERS sample, which should allow us to observe the effect of the molecule on the PSF, given that the position of the molecule dictates how the emission couples to the different plasmon modes, as discussed in Chapters 1 and 3.[5,10,23] Figure 5.4 compares the fits and residuals of the Gaussian and dipole fits on the SM-SERS active nanoparticle dimer shown in Figure 5.4A, and we again see that the residual values shrink as we move from a 2-D Gaussian to a 1-dipole fit, and then improve incrementally as we apply the 3-dipole, 3-λ dipole, and 3-dipole z-fit models. As in the MM-SERS data presented in Figure 5.2, all of the fit residuals are non-random, indicating that these models are still not sufficient to capture the entirety of the SERS PSF.

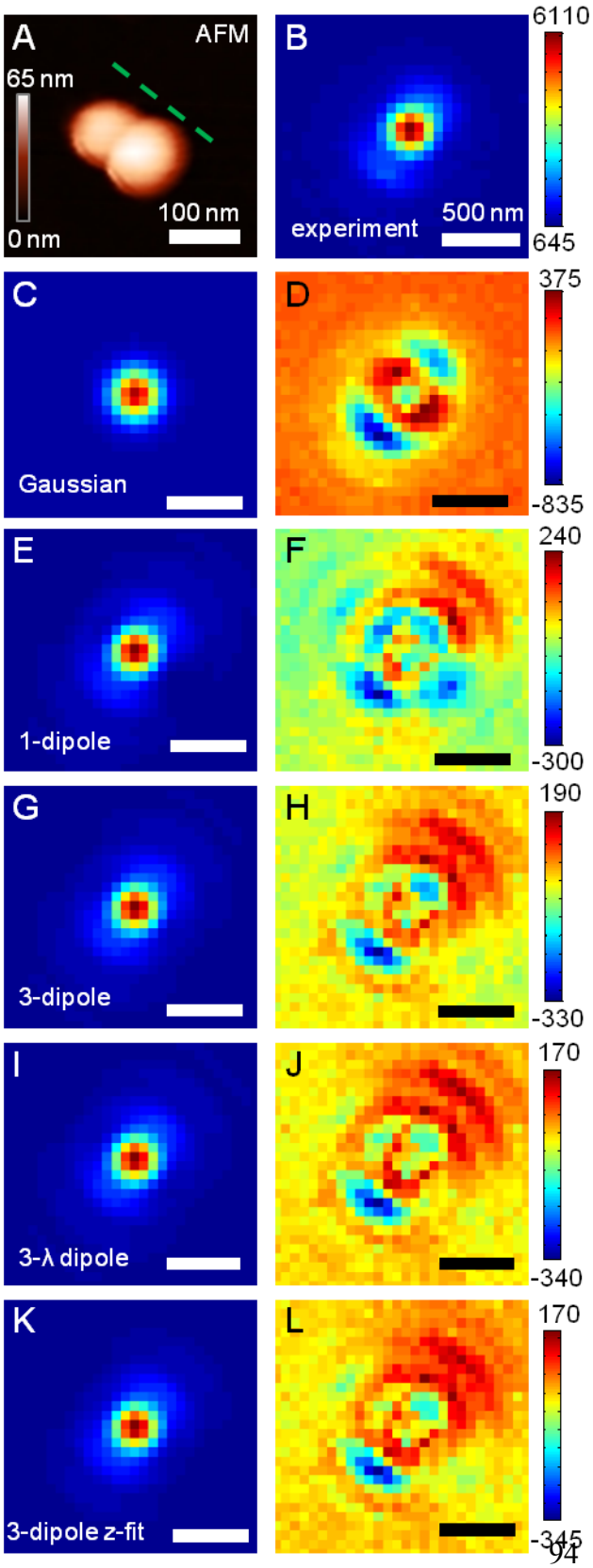

Figure 5.4. (A) AFM structure of nanoparticle dimer, where the green line indicates the φ value of the 3-dipole fit. (B) Experimental SM-SERS intensity image. (C-L) Fits (left) and residuals (right) for the different PSF models as indicated.

In previous super-resolution imaging experiments on SM-SERS substrates (see Chapter 3), we noted that silver nanoparticles are inherently luminescent and that this luminescence is convoluted with the SERS in the experimental emission patterns.[9,24] We can isolate the two signals by exploiting the inherent on-off behavior of SM-SERS signals. Accounting for the luminescence could have important implications for the resulting fits, because we have previously reported that the luminescence centroid can be spatially distinct from the SERS emission centroid.[24] To remove the luminescence contribution, we first use our correlated spectra to identify images when no SERS is observed, and nanoparticle luminescence is the only contributor; an example is shown in Figure 5.5A. We use a 2-D Gaussian to fit each of the images associated with nanoparticle luminescence, and then calculate an average best fit to represent the contribution from the nanoparticle, as shown in Figure 5.5B. Given the poor signal-to-noise of the luminescence, the more complex dipole models did not perform well, generating random and incorrect values of φ, which is why we used the 2-D Gaussian model to fit the luminescence images. Next, we subtract away the fitted luminescence contribution from the experimental emission image shown in Figure 5.4B to yield the isolated SM-SERS shown in Figure 5.5C. This image is then fit to the 3-dipole model (Figure 5.5D) and the residuals are calculated (Figure 5.5F). We find that the residuals are nearly identical between the fits to the subtracted image (Figure 5.5F) and the non-subtracted image (Figure 5.4H). However, if we compare the centroid positions that we calculate using either the raw image data or the subtracted image (Figure 5.5E), we find that the difference in average centroid position between the two cases is 1.7 nm. Although this offset is statistically significant as determined *via* a paired t-test (at α=0.05), we do not apply the luminescence subtraction for the rest of our SM-SERS analysis due to the lack of residual improvement.

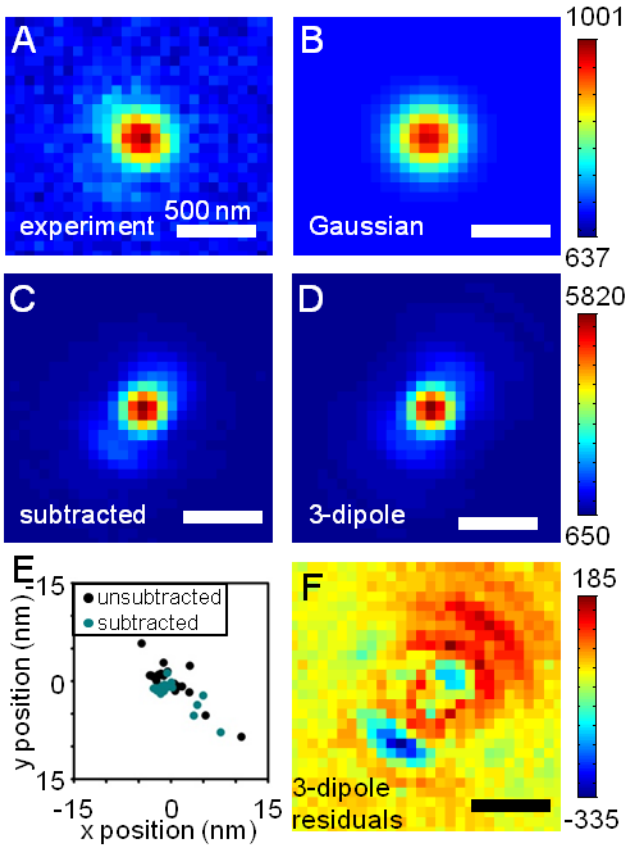

Figure 5.5. (A) Example image of nanoparticle luminescence background. (B) Average 2-D Gaussian fit of nanoparticle luminescence over 20 frames. (C) Subtracted SM-SERS intensity image obtained by subtracting the best fit to the luminescence in Figure 5B from the experimental data in Figure 4B. (D) 3-dipole fit and (F) residuals for the subtracted image in 5C. (E) Calculated centroid positions of SM-SERS emission from 20 image frames with and without nanoparticle background subtraction.

Table 5.2 compares the fit results of the different PSF fits on the SM-SERS sample from Figures 5.4 and 5.5. Again, it is seen that the dipole PSF fits all show good agreement when fitting the in-plane orientation of the dimer (Figure 5.4A), φ, just as in the MM-SERS case. In this case, the 3-dipole fits show a significantly better agreement with the measured θ value of 86° than the 1-dipole fit. As in the case of MM-SERS emission, the 1-dipole PSF highly overestimates the emission wavelength (based on the MM-SERS

spectrum shown in Figure 5.3B). The 3-dipole fit also overestimates λ, although not as dramatically as the 1-dipole fit, consistent with previous results. Unlike the MM-SERS case, the 3-λ model provides very poor wavelength fits, with both the TM and OOP mode far to the red of the calculated LM emission. Also, by including a z offset in the 3-dipole model PSF, we again find the most reasonable prediction of the emission wavelength, but also observe an overestimate of the distance of the emission from the surface, as the z-offset is calculated at 80 ± 12 nm from the surface, while the height of the tallest particle in the dimer is only 59 nm. Finally, we have included the results of the nanoparticle luminescence-subtracted fit, which shows that while there may be a slight difference between the average luminescence-subtracted and unsubtracted 3-dipole fit centroids, the other fit estimates are in agreement.

Table 5.2. Parameter values for different fitting functions applied to the SM-SERS example from Figure 5.4.

	φ (°)	**θ (°)**	**λ (nm)**	**Δx (nm)[a]**	**Δy (nm)[a]**	**fit time[b]**	**R**	**K**	**z**
2-D Gaussian	N.A.	N.A.	N.A.	0(2)	0(2)	1 s	N.A	N.A.	N.A.
1-dipole PSF	39(2)	70(2)	630(12)	28(3)	25(4)	13 min	11[c]	N.A.	00[c]
3-dipole PSF (single-λ)	38(1)	89(3)	603(7)	1(4)	4(3)	33 min	0.79(4)	0.0(2)	00[c]
3-dipole PSF (multi-λ)[d]	37.6(9)	85(1)	611(5) (LM) 793(8) (TM) 780(30) (OOP)	4(1)	7(2)	137 min	0.84(1)	0.97(4)	00[c]
3-dipole z-fit PSF[d]	38(2)	85(2)	584(6)	6(2)	8(2)	26 min	0.92(4)	0.8(3)	80(12)
bkgd. subtracted 3-dipole PSF[d]	38(2)	89(2)	603(8)	1(3)	5(2)	17 min	0.83(3)	-0.1(3)	00[c]

[a] $\Delta x(\Delta y)$ corresponds to $(x(y)_{0D}\text{-}x(y)_{0G})$ for each type of fit [b] Per frame, approximate [c] Fixed parameter

Values in parentheses indicate the standard deviation of the fit in the last significant figure over 31 image frames (except for lines marked with ([d]).

Looking at the calculated centroid values across the different models, we see that the standard deviations are much higher for the SM-SERS centroid positions (2 - 4 nm) compared to the MM-SERS values (≤ 0.5 nm). On first glance, one might assume that the larger error is due to lower signal-to-noise associated with SM-SERS, but a comparison across multiple samples found that MM-SERS samples with similar signal-to-noise ratios showed smaller standard deviations in the centroid positions, as shown below in Figure 5.6. Thus, we attribute the increased variability in the centroid position in the SM-SERS sample as an effect of molecular motion, which influences how the molecule interacts with the various plasmon modes of the nanoparticle, thereby shifting its centroid.[8,10,23]

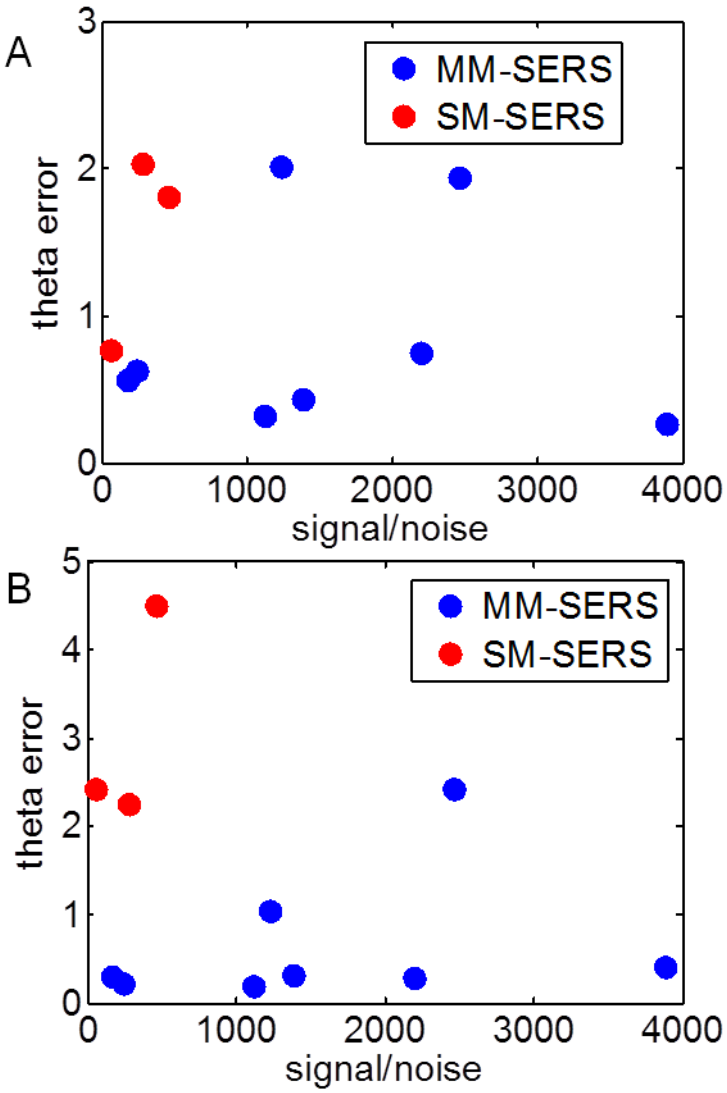

Figure 5.6. Plots showing uncertainty in fit values of θ vs. the signal-to-noise ratio of the SERS emission in both the 1-dipole (A) and 3-dipole (B) fits.

5.5 Localization of SERS emission in SM- and MM-cases

To compare the calculated centroids between MM-SERS and SM-SERS samples, we calculated two-dimensional spatial intensity maps, which relate the intensity of the measured SERS to the position of the calculated centroid.[9] To do this, fitted centroid locations from individual image frames associated with SERS emission are collected into

1 nm bins, and the color of the bin is determined by the average fitted intensity of the points in each bin. We have calculated spatial intensity maps using both the 2-D Gaussian (Figure 5.7, middle column) and the 3-dipole (Figure 5.7, right column) models. A white "x" is used to represent the average value of the Gaussian centroid in the 3-dipole spatial intensity maps for ease of comparison. We chose the single-λ 3-dipole model with no z offset for these calculations because the 1-dipole model has provided the poorest fits of all the dipole models, the 3-λ model produced unreasonable wavelength values for the TM and OOP modes in the SM-SERS regime, and the 3-dipole z-fit model produced non-physical offset values and poor convergence characteristics.

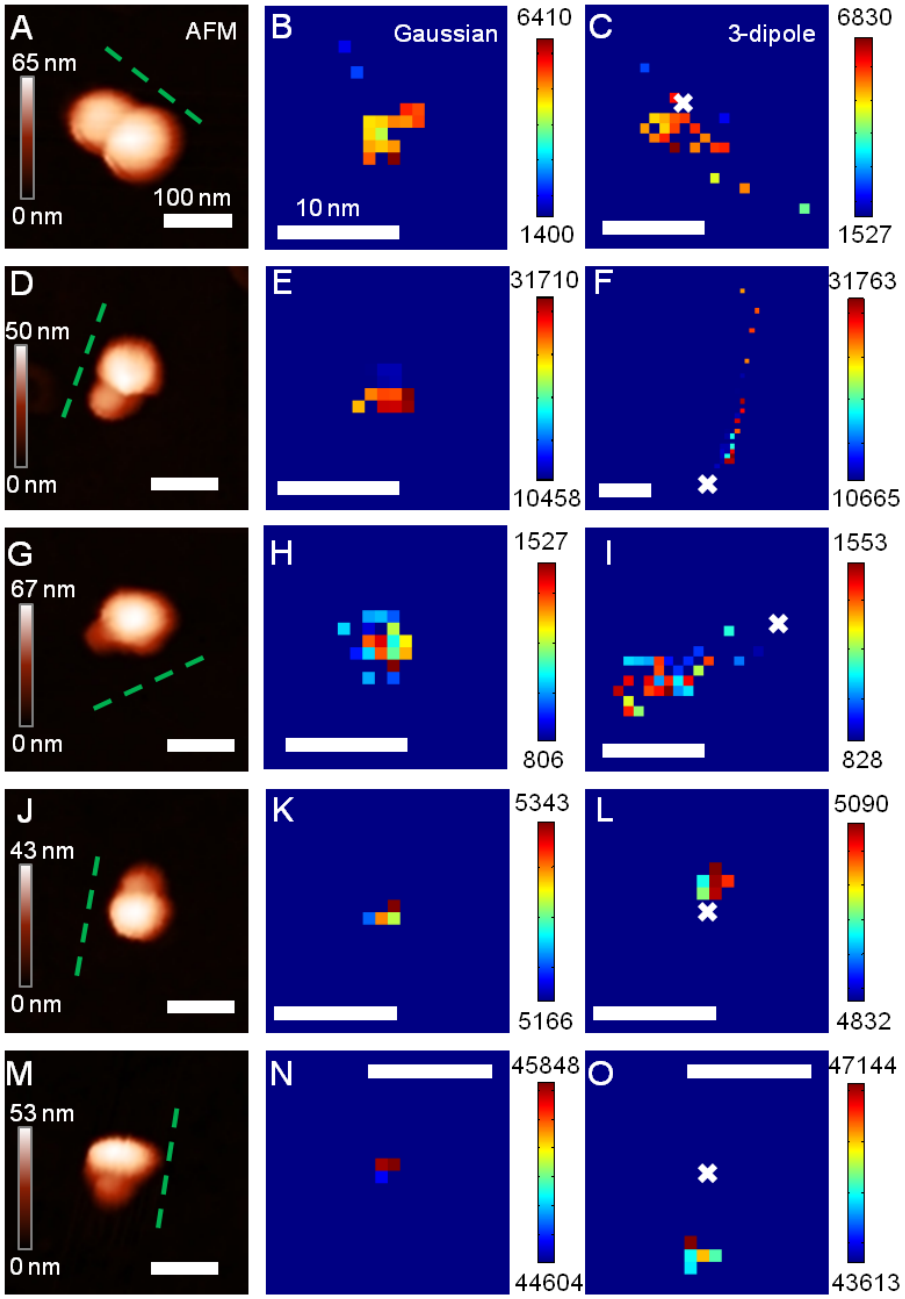

Figure 5.7. AFM images and spatial intensity maps that indicate the average intensity of all centroids located within each 1 nm bin. (Left column) AFM image (with the 3-dipole φ fit estimate indicated by the dashed line), (center column) spatial intensity map using the 2-D Gaussian model, and (right column) spatial intensity map using the 3-dipole model. A white x indicates the average position of the 2-D Gaussian centroid. Panels (A-I) show SM-SERS examples, with MM-SERS examples in (J-O).

Figure 5.7 shows a series of AFM images and the associated spatial intensity maps for three SM-SERS samples and two MM-SERS samples. In the case of the SM-SERS examples (Figure 5.7, panels A-I), the Gaussian and 3-dipole fits not only localize the emission to different positions, but the 3-dipole fits also show significantly more spread in the centroid position, oriented along the φ axis of the dimer. This direction of centroid motion is highly correlated with changing values of θ which was also seen in the nanorod study shown in Chapter 4, and consequently we have noted higher uncertainties in the fit values of θ in the single molecule examples (typically ±3º). As described above, we assign the changing SM-SERS centroid to a mobile molecule on the nanoparticle surface; as the molecule moves, the efficiency with which it couples to the different plasmon modes of the nanoparticle changes, thereby shifting the measured centroid.[8–10] In previous work, we have noted that the SM-SERS centroid position can change by as much as 40 nm over the course of an experiment, allowing us to effectively map out the local electromagnetic enhancement associated with the hot spot.[9,11] One question that has come up is whether the dramatic change in the centroid position was an artifact due to the relative simplicity of the 2-D Gaussian fitting model we used. In this study, we find that using a more complex 3-dipole model actually generates more spread in the centroid position relative to the 2-D Gaussian. Moreover, our previous work using a 2-D Gaussian model has shown excellent qualitative agreement between the shape of the spatial intensity maps and the structure of the underlying nanoparticle junctions.[24,11] In the examples shown here, we find that the 3-dipole model does not provide good qualitative agreement with the orientation of the nanoparticle junctions

In contrast to the SM-SERS examples, the MM-SERS data shown in Figure 5.7, panels J-O, show tightly confined centroid positions associated with low standard deviations in the calculated θ values (±0.7º). The MM-SERS centroid behavior is

consistent with the picture that we are measuring an ensemble-averaged centroid position, due to the fact that we have multiple molecules that are able to couple to all resonant plasmon modes within the structure. Even if the molecules are mobile on the surface, the average centroid does not change dramatically because the high surface coverage ensures that emission is not dominated by coupling to a single plasmon mode. As a result, the centroid collapses to a single value which is largely dictated by the geometry of the nanostructure, rather than the positions of the individual molecules.

5.6 Determining dipole orientation in SM- and MM-cases

Despite the fact that the SM-SERS samples show mobile centroids relative to the MM-SERS counterparts, we find that the 3-dipole fit is still able to produce orientation parameters that reflect the underlying nanoparticle structure. In Figure 5.8, we show the relationship between the measured and fit values of both φ and θ using the 3-dipole PSF. In Figure 5.8A, the calculated φ value agrees well with the experimentally measured φ value based on the nanoparticle structure whether we are probing an SM-SERS or an MM-SERS-active dimer. However, when comparing θ fit values with the measured structure of the nanoparticle (Figure 5.8B), we see that the fit data does not agree with the measured structure as well as the φ values do. The lack of agreement may be due to our definition of θ, which is based on the relative height and separation of the two nanoparticles and may not reflect the true orientation of the longitudinal plasmon mode. We also observe that the single molecule cases have larger uncertainties in θ than the MM-SERS cases, consistent with the larger centroid uncertainties noted in Figure 5.7. We again attribute the increased uncertainty in θ as an effect from the motion of a single molecule, whereas molecular effects in the case of the high-dye concentration samples are averaged over many molecules.

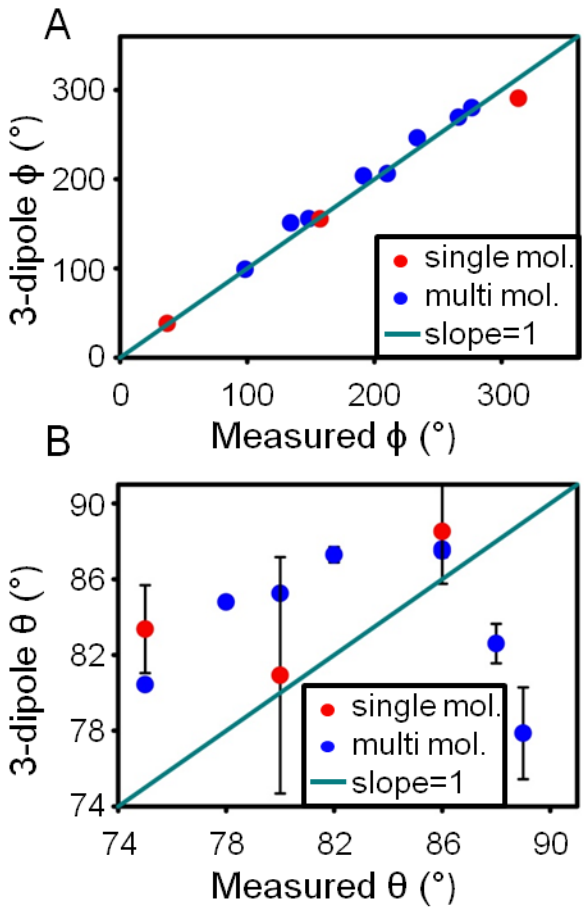

Figure 5.8. Relationship between 3-dipole fits and estimates based on structure for both (A) φ and (B) θ. Points are color-coded based on whether the sample is SM- or MM-SERS.

After comparing the quality of super-resolution fits using both Gaussian and dipole emission PSF modeling, we find that none of the dipole PSFs used in this study can accurately describe the full PSF of a SERS active aggregate, based on the non-random residuals associated with the various fits. This being said, a 3-dipole PSF fit showed much lower residuals than the 2-D Gaussian, and was able to accurately represent the geometry of the underlying structure, while still being sensitive to the contributions of the molecule in the SM-SERS examples. Even for the simple case of nanoparticle dimers, the minimum level of complexity that can give reasonable estimates for θ and λ is

a 3-dipole fit. Fitting plasmon-mediated emission with a dipole PSF of insufficient complexity (*e.g.* a 1-dipole fit) can strongly skew several fit parameters, notably θ, λ, and the centroid location.

We hypothesize that one reason the 3-dipole fits show systematic residuals in both the MM-SERS and SM-SERS cases is that the three mutually-orthogonal dipoles share a common origin. In reality, we would not expect this to be the case. For example, an asymmetric dimer is expected to have a longitudinal dipole mode oriented along the long axis of the dimer, as well as two transverse modes, each associated with the two different nanoparticles that comprise the dimer. If the two nanoparticles are of different size (as is the case in the examples shown here), then we expect one transverse mode to have a stronger resonant overlap with our emission than the other,[25] which would bias the origin of the emission polarized along the transverse dipole mode towards one nanoparticle. Our 3-dipole model cannot capture this subtle shift because we model the three dipoles as originating from a common origin, which may explain why our fits still show systematic errors. In principle, we could try to fit the data to three (or more) decoupled dipole modes, but the number of adjustable parameters becomes quite high and the computational expense nearly prohibitive. Moreover, as we work on higher order aggregates (timers, tetramers, *etc*), representing the various mode contributions (especially in the absence of structure correlation) becomes extremely challenging. While the dipole models do give more insight into the nature of the underlying plasmon modes, the 2-D Gaussian still remains a useful model in super-resolution fitting of plasmon-mediated emission, due to its robustness, low computational expense, and ability to capture the effect of a mobile molecule on the centroid position in SM-SERS samples.

5.7 Conclusion

In this study, we have compared the results of fitting diffraction-limited emission patterns from both MM-SERS and SM-SERS active silver nanoparticle dimers, using a 2-D Gaussian and several variations of a dipolar emission PSF. A 3-dipole PSF fit provided the best overall fit, based on the magnitude of the residuals and fits to measurable parameters (φ, θ, λ), although with increased computational expense, systematic error in the fits, and imperfect agreement between the structure of the nanoparticle and the shape of the spatial intensity maps in the SM-SERS limit. We have also have shown that, based on the difference between the SM-SERS and MM-SERS examples, the position of the SERS reporter molecule can influence the shape of the PSF—and thus the results of the fit—in the low concentration regime. On the other hand, a high concentration of SERS reporter molecules yields less uncertainty in the fit parameters and gives more precise centroid localization, due to the averaging of the various molecular contributions to the PSF. Lastly, we show that the choice of model when fitting plasmon-mediated emission strongly affects super-resolution results, and that structure correlation remains an important tool for comparing spatial intensity maps against nanoparticle geometry.

5.8 Acknowledgement

We would like to thank M. Weber and Y. Mueanngern for preparing the Ag colloids used in this study, and J. Enderlein for freely distributing his "QDControl.m" code through his website. This material is based on work supported by the Welch Foundation under Award No. F-1699.

5.9 References

(1) Titus, E. J.; Willets, K. A. Accuracy of Superlocalization Imaging Using Gaussian and Dipole Emission Point-Spread Functions for Modeling Gold Nanorod Luminescence. *ACS Nano* **2013**, *7*, 6258–6267.

(2) Fang, Y.; Chang, W.-S.; Willingham, B.; Swanglap, P.; Dominguez-Medina, S.; Link, S. Plasmon Emission Quantum Yield of Single Gold Nanorods as a Function of Aspect Ratio. *ACS Nano* **2012**, *6*, 7177–7184.

(3) Yorulmaz, M.; Khatua, S.; Zijlstra, P.; Gaiduk, A.; Orrit, M. Luminescence Quantum Yield of Single Gold Nanorods. *Nano Lett.* **2012**, *12*, 4385–4391.

(4) Li, Z.; Shegai, T.; Haran, G.; Xu, H. Multiple-Particle Nanoantennas for Enormous Enhancement and Polarization Control of Light Emission. *ACS Nano* **2009**, *3*, 637–642.

(5) Shegai, T.; Li, Z.; Dadosh, T.; Zhang, Z.; Xu, H.; Haran, G. Managing Light Polarization via Plasmon–Molecule Interactions Within an Asymmetric Metal Nanoparticle Trimer. *Proc. Natl. Acad. Sci.* **2008**, *105*, 16448–16453.

(6) Stranahan, S. M.; Titus, E. J.; Willets, K. A. SERS Orientational Imaging of Silver Nanoparticle Dimers. *J. Phys. Chem. Lett.* **2011**, *2*, 2711–2715.

(7) Shegai, T.; Brian, B.; Miljković, V. D.; Käll, M. Angular Distribution of Surface-Enhanced Raman Scattering from Individual Au Nanoparticle Aggregates. *ACS Nano* **2011**, *5*, 2036–2041.

(8) Ausman, L. K.; Schatz, G. C. On the Importance of Incorporating Dipole Reradiation in the Modeling of Surface Enhanced Raman Scattering from Spheres. *J. Chem. Phys.* **2009**, *131*, 084708–084708–10.

(9) Stranahan, S. M.; Willets, K. A. Super-Resolution Optical Imaging of Single-Molecule SERS Hot Spots. *Nano Lett.* **2010**, *10*, 3777–3784.

(10) Titus, E. J.; Weber, M. L.; Stranahan, S. M.; Willets, K. A. Super-Resolution SERS Imaging beyond the Single-Molecule Limit: An Isotope-Edited Approach. *Nano Lett.* **2012**, *12*, 5103–5110.

(11) Weber, M. L.; Willets, K. A. Correlated Super-Resolution Optical and Structural Studies of Surface-Enhanced Raman Scattering Hot Spots in Silver Colloid Aggregates. *J. Phys. Chem. Lett.* **2011**, *2*, 1766–1770.

(12) Enderlein, J. Imaging of Single Molecules http://www.joerg-enderlein.de/imagingOfSingleMolecules.html (accessed May 3, 2013).

(13) Dieringer, J. A.; Lettan, R. B.; Scheidt, K. A.; Van Duyne, R. P. A Frequency Domain Existence Proof of Single-Molecule Surface-Enhanced Raman Spectroscopy. *J. Am. Chem. Soc.* **2007**, *129*, 16249–16256.

(14) Nie, S.; Emory, S. R. Probing Single Molecules and Single Nanoparticles by Surface-Enhanced Raman Scattering. *Science* **1997**, *275*, 1102–1106.

(15) Bartko, A. P.; Dickson, R. M. Three-Dimensional Orientations of Polymer-Bound Single Molecules. *J. Phys. Chem. B* **1999**, *103*, 3053–3056.

(16) Bartko, A. P.; Dickson, R. M. Imaging Three-Dimensional Single Molecule Orientations. *J. Phys. Chem. B* **1999**, *103*, 11237–11241.

(17) Hellen, E. H.; Axelrod, D. Fluorescence Emission at Dielectric and Metal-Film Interfaces. *J. Opt. Soc. Am. B* **1987**, *4*, 337–350.

(18) Hao, E.; Schatz, G. C. Electromagnetic Fields around Silver Nanoparticles and Dimers. *J. Chem. Phys.* **2004**, *120*, 357–366.

(19) Halas, N. J.; Lal, S.; Chang, W.-S.; Link, S.; Nordlander, P. Plasmons in Strongly Coupled Metallic Nanostructures. *Chem. Rev.* **2011**, *111*, 3913–3961.

(20) Enderlein, J.; Toprak, E.; Selvin, P. R. Polarization Effect on Position Accuracy of Fluorophore Localization. *Opt. Express* **2006**, *14*, 8111–8120.

(21) Engelhardt, J.; Keller, J.; Hoyer, P.; Reuss, M.; Staudt, T.; Hell, S. W. Molecular Orientation Affects Localization Accuracy in Superresolution Far-Field Fluorescence Microscopy. *Nano Lett.* **2011**, *11*, 209–213.

(22) Lew, M. D.; Backlund, M. P.; Moerner, W. E. Rotational Mobility of Single Molecules Affects Localization Accuracy in Super-Resolution Fluorescence Microscopy. *Nano Lett.* **2013**.

(23) Stranahan, S. M.; Titus, E. J.; Willets, K. A. Discriminating Nanoparticle Dimers from Higher Order Aggregates through Wavelength-Dependent SERS Orientational Imaging. *ACS Nano* **2012**, *6*, 1806–1813.

(24) Weber, M. L.; Litz, J. P.; Masiello, D. J.; Willets, K. A. Super-Resolution Imaging Reveals a Difference between SERS and Luminescence Centroids. *ACS Nano* **2012**, *6*, 1839–1848.

(25) Oubre, C.; Nordlander, P. Optical Properties of Metallodielectric Nanostructures Calculated Using the Finite Difference Time Domain Method. *J. Phys. Chem. B* **2004**, *108*, 17740–17747.

Chapter 6: Raman Characterization, Modification and Application of Carbon Nanotube AFM Probes Towards Problems in SERS[4]

6.1 Introduction

In the previous chapters, several methods of super-resolution imaging have been used to study single- and multi-molecule SERS "hot spots", yielding information about the interactions between the Raman active molecule(s) and the SERS active silver nanoparticle aggregates. One important piece of information that cannot be determined from these studies is exactly where the molecule is on the nanoparticle aggregate when it is emitting. This is due to the fact that the SERS emission from the molecule is coupled out into the far-field through the nanoparticle, as discussed in previous chapters. Being able to map out the size, shape, and location of the "hot spot" topography could aid in the rational design of SERS sensors with single-molecule sensitivity, but this is difficult to obtain through super-resolution studies due to the above mentioned problem.

In previous studies, several different sub-diffraction limited techniques have been used to understand the structure of SM-SERS "hot spots", such as scanning near-field optical microscopy (SNOM)[1–3] or structural imaging techniques like atomic force microscopy (AFM)[4,5] or electron microscopies (SEM/TEM).[6,7] While these techniques are useful tools in this field, they each have drawbacks, such as distortion of the plasmonic fields with a large probe (SNOM) or lack of optical information (SEM/AFM). It is for these reasons that we attempted to utilize a combined total internal reflection (TIR)/AFM microscope with a carbon nanotube (CNT) AFM probe, in order to allow for the simultaneous collection of optical and sub-diffraction-limited topographical information. In this technique, a CNT-functionalized AFM probe is scanned over a

[4] Reproduced in part with permission from Kaplan-Ashiri, I.; Titus, E. J.; Willets, K. A. Subdiffraction-Limited Far-Field Raman Spectroscopy of Single Carbon Nanotubes: An Unenhanced Approach. *ACS Nano.* **2011,** *5,* 1033-1041. Copyright 2011 American Chemical Society.

plasmonically active substrate to measure the structure of the substrate, while the sample is simultaneously excited with the evanescent field from a TIR microscope. By placing the CNT on the AFM probe in close proximity to the nanostructure, we hoped to enhance the Raman signal from the CNT (CNT-SERS), which would then be collected and correlated to the probe position in order to map regions of strong enhancement, as shown in Figure 6.1 below.[8,9] One of the major benefits of this experiment is that by attaching the Raman analyte (CNT) to the AFM probe, the location of the enhanced fields can also be observed without the molecule-nanoparticle convolution of super-resolution imaging. Furthermore, this technique can even outperform standard AFM when it comes to determining nanoparticle topography, due to the high resolution offered by the high-aspect ratio CNT-AFM probe.[10–12]

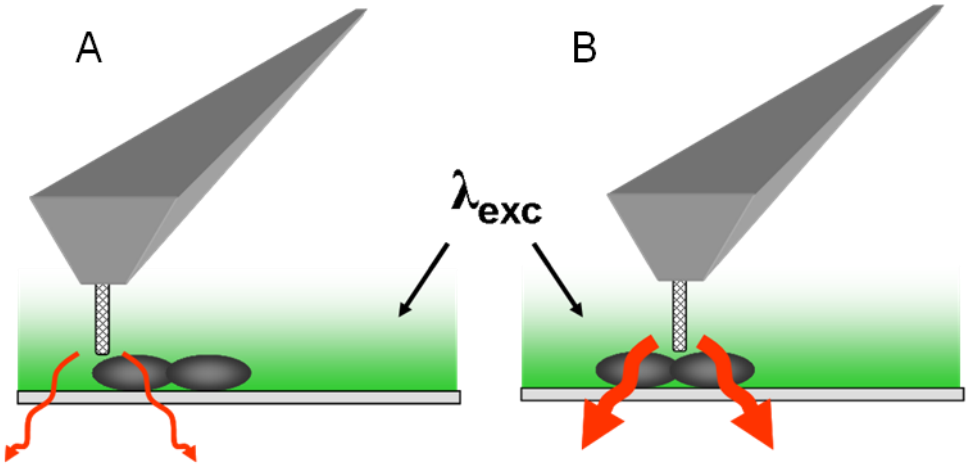

Figure 6.1. Schematic of the CNT-AFM scanning experiment, showing weak Raman scattering in regions of low enhancement (A) and strong Raman scattering in regions of high enhancement (B).

In order to accurately map the topography of SERS "hot spots" around nanostructures using this technique, we first started by preparing and characterizing CNT-AFM probes. The probes were structurally characterized *via* SEM and optically

characterized *via* the TIR/AFM microscope. In the process of optically characterizing the probes, we were able to use the tunable intensity profile of the evanescent field of the TIR microscope to characterize the Raman signature of the CNT-AFM probe along its long-axis with sub-diffraction limited resolution. Additionally, we were able to use this technique in order characterize the *in situ* chemical functionalization of the end of the CNT on the AFM probe.[13] Once the normal Raman characteristics of these probes have been discussed, we include some data regarding the scanning of plasmonic structures with CNT-AFM probes.

6.2 Fabrication of CNT-AFM probes and experimental setup

CNT-AFM probes for all experiments were fabricated using a scanning electron microscope system (FEI Strata) equipped with a nanomanipulation system (Zyvex), and a gas injection system (Omniprobe)[14]. First, a tungsten wire is dipped into a dry multi-walled CNT sample (8-15 nm OD), and then is attached to the manipulator, while a gold coated AFM probe (Budget Sensors Tap300GB) is mounted to a stub in the SEM. After locating an appropriate single CNT on the end of the wire, the CNT is brought into contact with the end of the AFM probe using the manipulator. To attach the CNT to the probe, a small amount of platinum is deposited onto the CNT-probe junction using electron beam deposition of an organo-platinum complex from the gas injection system. A SEM image of a fabricated probe is shown in Figure 6.2A.

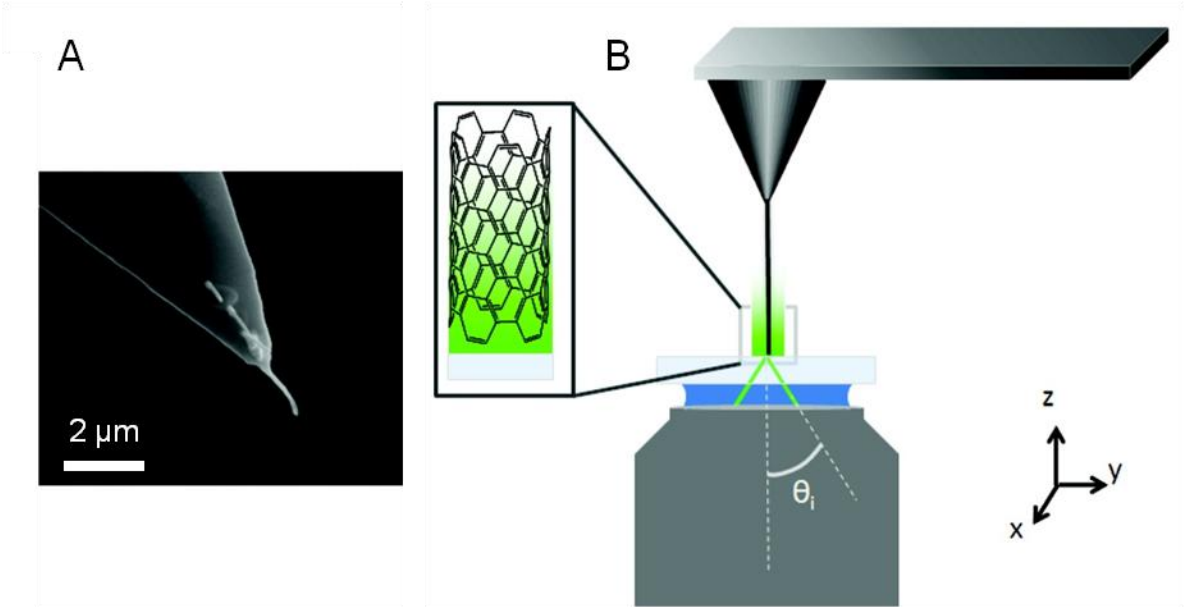

Figure 6.2. (A) AFM tip functionalized with a single carbon nanotube. (B) General schematic of the experiment. An AFM is coupled with an optical microscope based on through-the-objective TIR for Raman excitation. The AFM tip is functionalized with a single carbon nanotube, which is excited by the TIR evanescent field, and its Raman scattering is detected. The penetration depth of the evanescent field is tuned by adjusting the angle of incidence (θ_i) of the excitation beam. Adapted with permission from Kaplan-Ashiri, I.; Titus, E. J.; Willets, K. A. Subdiffraction-Limited Far-Field Raman Spectroscopy of Single Carbon Nanotubes: An Unenhanced Approach. *ACS Nano.* **2011**, *5*, 1033-1041. Copyright 2011 American Chemical Society.

Once a CNT-AFM probe has been fabricated, it is then used in the combined optical/atomic force microscope, a basic schematic of which is shown in Figure 6.2B, with a more detailed description shown in Figure 2.2.[15] In this setup, the CNT-AFM probe is imaged using the evanescent field from the TIR microscope. Excitation at the surface of the microscope slide is due to the evanescent field produced by excitation light that is incident on the coverslip/air interface above the critical angle. This creates an evanescent field that decays exponentially, as shown by Equation 6.1.[15–17]

$$I(z) = I_0 e^{-z/\ d} \tag{6.1}$$

In this equation, *I(z)* represents the intensity of the evanescent field at a distance *z* from the coverslip/air interface, I_0 represents the intensity at the interface, and *d* represents the penetration depth, or decay factor, of the intensity profile. The penetration depth of the evanescent field can be controlled by adjusting the angle of incidence of the beam, which is dictated by Equation 6.2.

$$d = \frac{\lambda_0}{4\pi}\left(n_1^2 \sin^2(\theta_i - n_2^2\right)^{-1/2} \tag{6.2}$$

Again, *d* is the penetration depth of the field, while λ_0 is the excitation wavelength, θ_i is the incident angle of the beam on the interface, and n_1 and n_2 are the refractive indices at the interface. Because TIR occurs at the coverslip/air interface, n_1=1.515 (glass) and n_2=1 (air); the minimum and maximum angles of incidence in this setup are dictated by the critical angle of the interface and the NA of the objective (1.45), respectively. In this experiment, the TIR angle is controlled *via* a micrometer driven lens at the back of the microscope, allowing θ_i, and therefore d, to be reproducibly set, after calibration of the lens position *vs*. θ_i.[18] Based on this experimental setup, the range of penetration depths used for experiments were between roughly 300-50 nm. While smaller penetration depths are achievable, low signal-to-noise becomes an issue. Based on this knowledge, CNTs for AFM probes are selected to have lengths of over 500 nm in order to ensure that the evanescent field interacts with the CNT only, and not the metallic part of the AFM probe. Additionally, because this microscope system is being used to measure Raman signals from the CNT, inorganic immersion oil (Cargille) is used to couple the microscope objective to the coverslip in place of the typically organic immersion oil, which has a Raman spectrum that overlaps with the CNT.

6.3 Position dependent Raman spectra along length of CNT-AFM probe

In order to utilize the CNT-AFM tips as Raman probes to investigate SERS, the unenhanced Raman of the CNT-AFM probes needs to be characterized. Due to the highly localized fields around plasmonic nanoparticles, we wanted to have an understanding of how the relative strength of the CNT Raman bands change along the length of the CNT. We accomplished this by collecting CNT-AFM probe Raman spectra at a range of different penetration depths. Because the penetration depth of the field can be adjusted in small steps (down to 2-10 nm), this technique actually allows for sub-diffraction limited optical characterization of the probes.[16,17] The Raman bands that we use to characterize the CNT-AFM probe are known as the G band and D band, which show up at ~1580-1590 cm^{-1} and ~1350 cm^{-1}, respectively. The G band is associated with graphitic in-plane vibrations, associated with the sp^2 hybridization of the CNT. The D (disorder) band is associated with sp^3 hybridization, which is expected at the end of the CNT, or at defect sites along the CNT.[19–24] These two Raman bands can be seen in the spectra shown in Figure 6.3A. This figure shows the Raman D and G bands (excited with p-polarization) for the CNT-AFM probe shown in Figure 6.2A, collected at several different penetration depths.

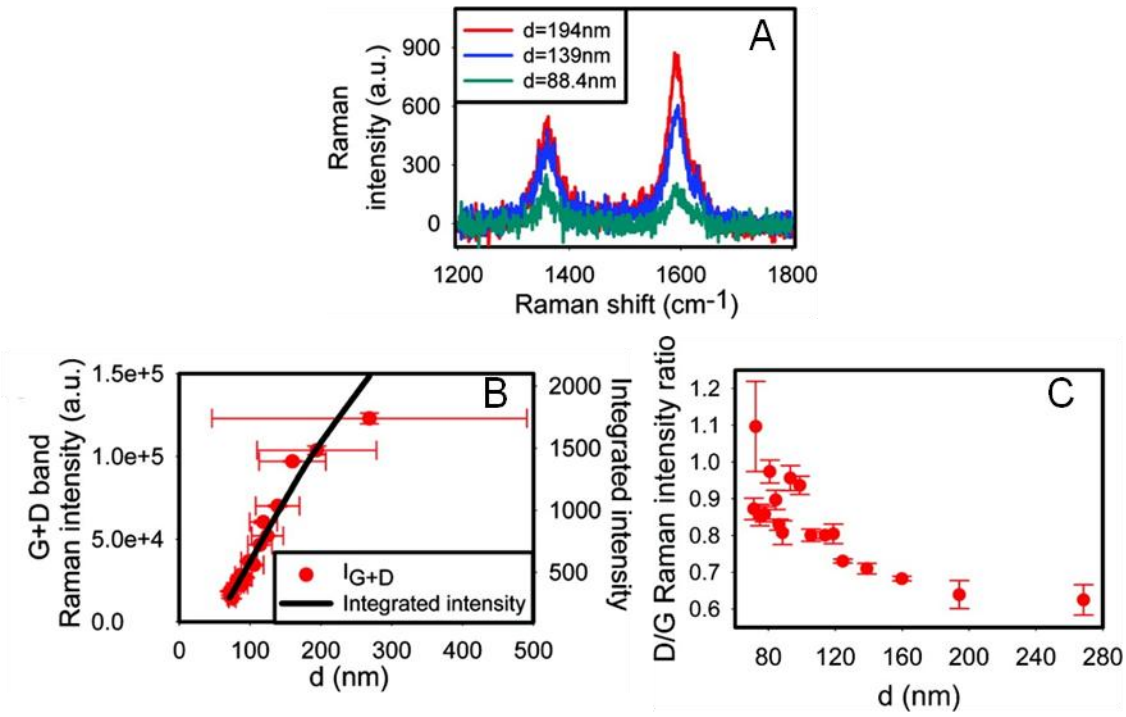

Figure 6.3. (A) Spectral series showing decrease in AFM-CNT Raman signal as penetration depth of evanescent field is lowered (p-polarized excitation). (B) Plot showing combined G and D band Raman intensity of probe and theoretical integrated intensity of the evanescent field vs. penetration depth. (C) Plot of D/G Raman intensity ratios decreasing as penetration depth increases. Adapted with permission from Kaplan-Ashiri, I.; Titus, E. J.; Willets, K. A. Subdiffraction-Limited Far-Field Raman Spectroscopy of Single Carbon Nanotubes: An Unenhanced Approach. *ACS Nano.* **2011**, *5*, 1033-1041. Copyright 2011 American Chemical Society.

In order to more quantitatively investigate the changes in the Raman scattering of the CNT-AFM probe with respect to changing penetration depth, we started by fitting collected Raman spectrum containing G and D bands to the sum of two Lorentzians with a linear background using Equation 6.3.

$$I(\tilde{\upsilon}) = I_{BG,0} + I_{BG,\tilde{\nu}}\tilde{\nu} + \sum_{i=1}^{i=2} I_{0,i} \frac{\left(\frac{1}{2}w_i\right)}{(\tilde{\nu} - \tilde{\nu}_{0,i})^2 + \left(\frac{1}{2}w_i\right)^2} \qquad (6.3)$$

In this equation, $I_{BG,0} + I_{BG,\tilde{\nu}}\tilde{\nu}$ is the linear, frequency dependent background, I_0 is the peak intensity, w_i is the width of each peak, and $\tilde{\upsilon}_{0,i}$ is the center frequency of the peak. By fitting the Raman spectrum of the CNT, we can extract integrated intensities for both the G and D bands. We start this analysis first by looking at the sum of the G and D peaks *vs.* the integrated intensity of the TIR evanescent field, which can be calculated based on the angle of incidence of the beam. The intensity of the evanescent field decreases with increasing θ_i (decreasing d) due to a decrease in I_0, which itself is dependent on θ_i.[16] Figure 6.3B shows that the sum of the integrated G and D peaks tracks closely with the calculated intensity of the evanescent field. Next, in Figure 6.3C, we compare how the D/G Raman integrated intensity ratio is affected by changing penetration depth. Here we can see that the relative contribution of the D band to the overall Raman scattering increases as penetration depth decreases.

In order to understand why the D/G Raman scattering ratio changes with penetration depth, we start by considering the relative Raman scattering contributions from different parts of the CNT, and how this will change with penetration depth. First, previous studies have shown that the majority of the D band Raman signal originates from the end of the CNT, due to the sp^3 hybridization present at the CNT terminus.[19] Next, we consider that this terminus will be very close to the interface generating the TIR, and that by changing the penetration depth, we adjust the overall fraction of the field intensity that is in the region close to the interface.[16,17] This means that at lower penetration depths, the end of the CNT gets a larger fraction of the overall illumination than it does at higher penetration depths.

6.4 Polarization sensitivity of CNT-AFM probes

The CNT-AFM polarization response is also an important characteristic of the probe, due to the highly polarized nature of the plasmon modes that give rise to

spectroscopic enhancement; if this system is to be used to map plasmonic enhancements, the CNT needs to be able to be excited by the plasmon enhanced fields.[25,26] In order to study this, we use linearly polarized excitation, with the polarization direction controlled *via* a doubled Fresnel rhomb. In TIR/evanescent field excitation, we define our polarization directions as s- and p-polarized, where s-polarized light is polarized parallel to the TIR interface, and p-polarized light is polarized perpendicular to this.[16] Because the incident angle of the excitation beam is not normal to the coverslip air interface, p-polarized light will have both in-plane and out-of-plane components, while s-polarized light will be exclusively in plane with respect to the coverslip surface; This means that p-polarized light will have a polarization component aligned with the long axis of the CNT, which should be more polarizable.[16,22,27] This is reflected in the p- and s-polarized Raman spectra shown in Figure 6.4, which correspond to the CNT-AFM probe shown in Figure 6.2A. At both penetration depths shown in this figure, we observe no observable Raman scattering from the CNT when exciting with s-polarization.

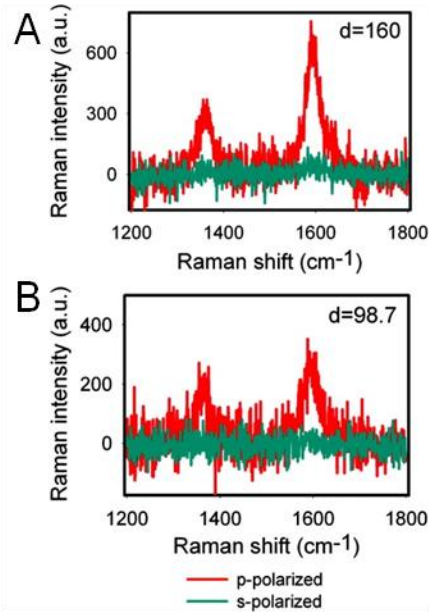

Figure 6.4. Excitation polarization dependence of the Raman spectra of a single carbon nanotube. The nanotube was excited separately with p-polarized (red line) and s-polarized (blue line) light. Spectra at two different penetration depths are presented, (A) d = 160 nm and (B) d = 98.7 nm. Adapted with permission from Kaplan-Ashiri, I.; Titus, E. J.; Willets, K. A. Subdiffraction-Limited Far-Field Raman Spectroscopy of Single Carbon Nanotubes: An Unenhanced Approach. *ACS Nano.* **2011**, *5*, 1033-1041. Copyright 2011 American Chemical Society.

Based on the polarization sensitivity of the Raman signal shown in Figure 6.4, we should also be able to utilize the polarization dependence of the CNT-AFM probe Raman in order to characterize its orientation. In this case, we would expect linear, vertically aligned CNT-AFM probes to have a polarization response similar to Figure 6.4, while a bent CNT should have more intense s-polarized scattering. Figure 6.5 shows p- and s-polarized Raman spectra at 2 penetration depths for two different probes. The CNT probe shown in Figure 6.5A appears bent in the SEM, and consequently shows much stronger s-polarized signal. Additionally, there appear to be extra spectral features in the Raman spectra of this CNT, possibly due to what appears to be amorphous carbon on the CNT as shown in the SEM image. In the case of the CNT-AFM probe shown in Figure 6.5B, we

again see spectral features indicating non-vertical CNT-AFM probe, but this cannot be confirmed *via* SEM. Because this CNT-AFM probe was fabricated from CNTs from a different manufacturer then those shown in Figures 6.5A and 6.2B, it may have Raman characteristics that do not match what has been observed for the other two probes, highlighting the need for Raman characterization of these probes.

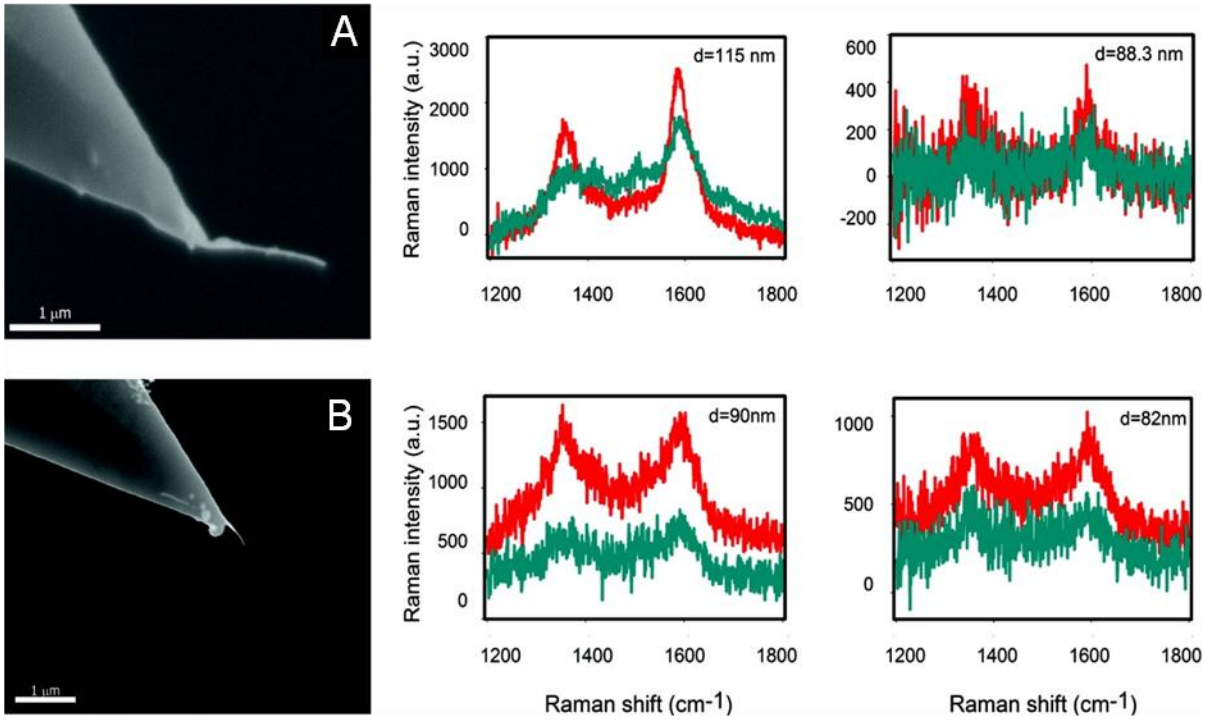

Figure 6.5. Excitation polarization dependence on nanotube orientation and structure. Sets of spectra for two different carbon nanotubes, each having different orientation and structure, were acquired using both p-polarized (red line) and s-polarized (blue) excitation. For each nanotube, spectra at two different penetration depths are presented. Adapted with permission from Kaplan-Ashiri, I.; Titus, E. J.; Willets, K. A. Subdiffraction-Limited Far-Field Raman Spectroscopy of Single Carbon Nanotubes: An Unenhanced Approach. *ACS Nano.* **2011**, *5*, 1033-1041. Copyright 2011 American Chemical Society.

6.5 *In situ* functionalization of CNT-AFM probes.

For any nanostructured, plasmonic substrate where we might consider using these CNT-AFM probes to map field enhancements, the fields generated by the plasmonic substrates are expected to have polarizations in the plane of the sample.[25,26] This could be problematic, because one of the major lessons of the CNT-AFM probe polarization study is that well aligned probes show significantly less Raman scattering when excited with in-plane (s) polarization compared to vertically (p) polarized light. Additionally, the type of topography that is accessible to the CNT probe is more likely to support in-plane plasmon modes rather than modes perpendicular to the substrate. This presents one of the most significant challenges to the goal of mapping plasmonic enhancement with these probes. One method of possibly addressing this problem could be to chemically functionalize the end of the CNT probe such that additional probe molecules with a different polarization response could be attached to the end of the CNT. In working towards this goal, we started by tracking the in situ chemical oxidation of the CNT using Raman spectroscopy. This oxidation is carried out by landing a CNT-AFM probe in a dried drop of 5% nitric acid on a coverslip, while simultaneously observing it on the TIR-AFM microscope. Because this experiment happens in ambient conditions, there is enough moisture on the slide due to ambient humidity to facilitate the oxidation reaction.[28] This process oxidizes the CNT, generating more sp^3 hybridization, which can be tracked through the growth of the Raman D band scattering.[19,20] Before and after spectra of a CNT-AFM probe undergoing this process can be seen in Figure 6.6 below. In this figure, the increase in the Raman D band intensity can be clearly seen in the spectrum of the functionalized CNT. Despite the success of this experiment, further functionalization of the CNT proved to be too difficult to undertake, due to the fragility of the CNT probe.

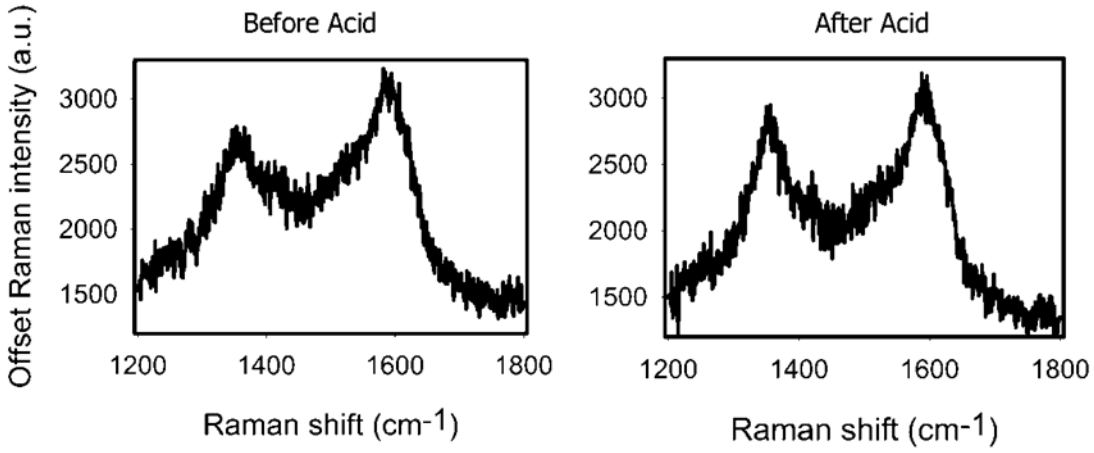

Figure 6.6. Raman spectra of a single carbon nanotube before and after 1 minute dipping in HNO_3. Adapted with permission from Kaplan-Ashiri, I.; Titus, E. J.; Willets, K. A. In Situ Chemical Functionalization of a Single Carbon Nanotube Functionalized AFM Tip using a Correlated Optical and Atomic Force Microscope. *Proc. Mat. Res. Soc.* **2011**, *1318*, 1-6. Copyright 2011 Materials Research Society.

6.6 Scanning plasmonically active silver nanoparticle aggregates

Samples and experimental setup

Although the data presented in the previous sections indicates that the Raman polarizibility of the CNT-AFM probes is not likely to be efficiently excited by the polarization of the enhanced fields around nanostructures, we still attempted to scan several silver nanoparticle aggregates using the CNT-AFM probes. Because the goal is to observe SERS from the CNT as it interacts with a plasmonic substrate during a scan, strong plasmonic enhancement is needed from the sample in order to obtain a measurable Raman signal on the timescale of an AFM scan.[7] For this reason, silver nanoparticle (AgNP) aggregates were chosen for this study due to the strength of their plasmonic enhancement, which can support single molecule SERS (SM-SERS) when coupled with specific Raman reporters.[7,29] AgNP aggregate samples for the CNT-AFM scanning experiment were prepared as specified in Chapter 2, but dye molecules were omitted

from the solutions. Dye was omitted in order to ensure that any optical signals collected during a scan originate from the CNT. We considered using rhodamine 6G (R6G) labeled samples, which would allow for a quick optical identification of strongly enhancing aggregates, but the possibility of spurious signals from the R6G makes assignment of the origin of the Raman signal (due to R6G or CNT) difficult. Unlabeled aggregates avoid this problem, but don't allow for identification of "hot" (strongly enhancing) aggregates before the start of a scan, and previous work has shown that "hot" aggregates are present at a very low percentage in these samples.[30]

In order to carry out a CNT-AFM scanning experiment, silver nanoparticle aggregates are prepared and deposited onto a plasma cleaned coverslip as described in Chapter 2. In addition to standard borosilicate coverslips, we also used #1 thickness quartz coverslips, which have a less intense fluorescence background. These samples were then mounted on the combined TIR/AFM setup shown in Figure 2.2 for scanning. During these experiments, we are using inorganic immersion oil in order to minimize background carbonaceous Raman signals. The optical detection setup used here was a single photon avalanche diode (SPAD), which was aligned to collect signal from a large area of the sample. A counting card (National Instruments) was used to measure photon counts from the SPAD and was also used to collect signals from the AFM controller that indicate the end of each AFM scan line. This allowed for correlation of optical signals from the SPAD and the position of the AFM probe. Laser intensities on the order of 0.5-6 kW/cm^2 were used to excite the nanostructures used in this experiment.

Scanning unlabeled AgNP aggregates

Examples of CNT-AFM scanning experiments using a relatively low laser power (500 W/cm^2) are shown below in Figure 6.7. Figure 6.7A shows the topography of the AgNP aggregate under investigation as determined using the CNT-AFM probe. Figure

6.7B shows the simultaneously-collected photon counts from the system, mapped in 2-dimensions in order to correlate the location of the CNT-AFM probe with the emitted photons from the system. In the optical data shown in Figure 6.7B, the minimum level on the colorbar axis is set to 3 standard deviations above the mean photon count rate, in order to show only statistically significant counts. Tip positions showing significant photon counts are boxed in Figure 6.7A-B. In order to increase the resolution, a small subsection of the scan region from Figure 6.7A-B was rescanned, with the results shown in Figure 6.7C-D, again with the tip positions where significant optical intensity was recorded highlighted on both plots. These highlighted regions agree with the correlated optical and topographical data of the larger scan, indicating the possibility that we are collecting enhanced Raman signals from the CNT, albeit with a low signal-to-noise ratio. Additionally, it is difficult to assign optical signals to a single CNT-AFM probe position due to the poor resolution in the X axis. In the scan data shown in Figure 6.7C-D, the AFM probe moved in 0.6 nm steps with a 3 ms dwell time at each point along the X-axis (fast scan direction) in a line-by-line scan, which when coupled with the 500 ms integration time, makes the photon count mapping resolution 99.4 nm in the x-direction. This is an important limitation, as this resolution is dependent on some fundamental limitations of both the optical detection and AFM sides of the experiment; better signal-to-noise is obtained with long integration times, but this sacrifices spatial resolution due to limits on how slow the AFM probe can be scanned to accurately determine topography. In this case, the y-direction (slow scan direction) is unaffected because each row of the AFM image is built up one line at a time.

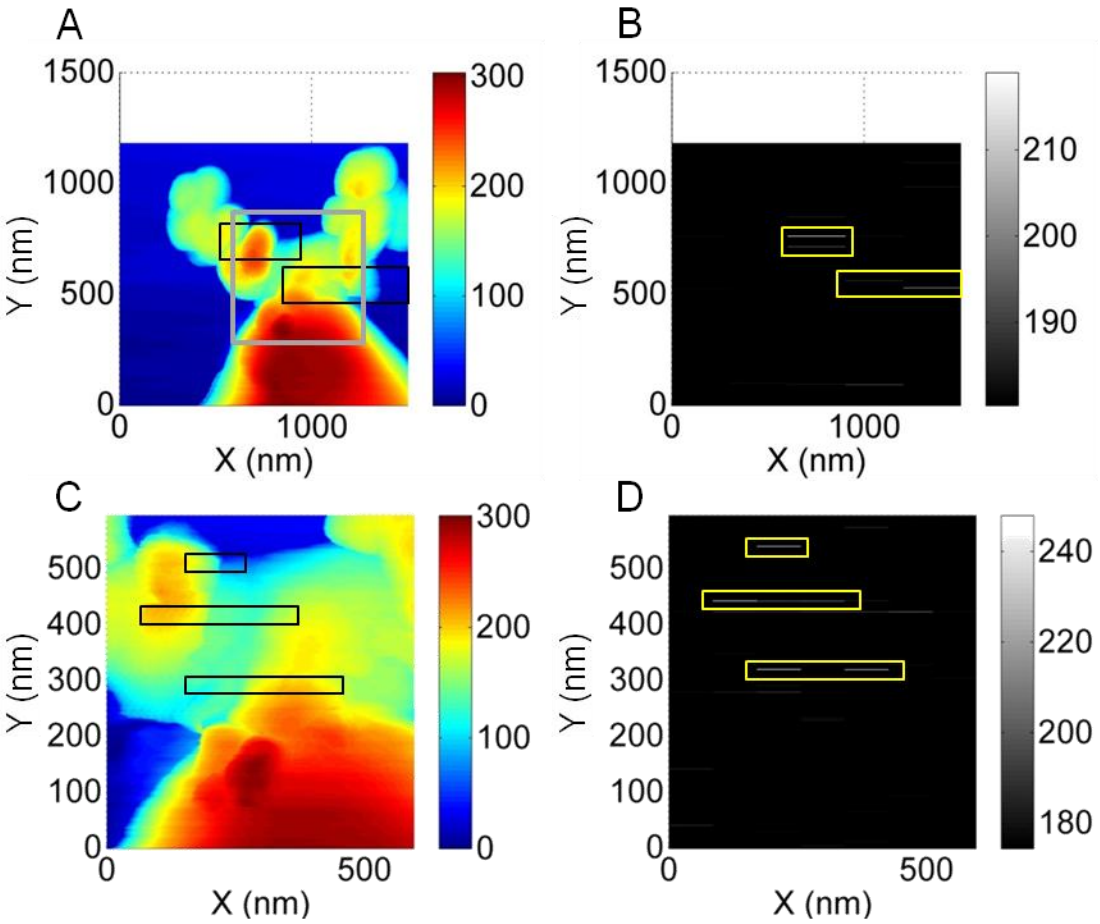

Figure 6.7. (A) Topography of AuNP aggregate from AFM scan, with correlated optical counts from SPAD (B) for low laser intensity CNT-AFM scan of aggregate (500 W/cm^2). Zoomed in AFM measured topography (C) and correlated optical counts (D) of same particle at same power. The gray box in (A) shows the region mapped in (C) and (D). Colorbars in (A) and (C) represent height in nm, while the colorbars in (B) and (D) represent SPAD counts/500 ms

Because the scans in shown in Figure 6.7 showed optical signals in the same topographical regions around the aggregate, but had low signal-to-noise, we rescanned the particle under higher intensity laser illumination in order to increase the signal from any potential CNT-AFM SERS. The results of this scan are shown in Figure 6.8A-B. In this case, we still see photon counts that correlate to nanoparticle topography, but we also

see additional regions that show strong optical signals where there is no nanoparticle (as indicated by the green boxes in Figure 6.8B). One hypothesis that we posited for this effect is that the enhanced fields from the aggregate could have damaged the CNT, which has been observed in the case of other Raman probes.[31] Additionally, when we scanned the topography of the AgNP aggregate after the high power illumination, we saw that the aggregate topography had changed, shown in the before and after AFM scans in Figure 6.8C-D, likely due to melting of the nanoparticle.[32]

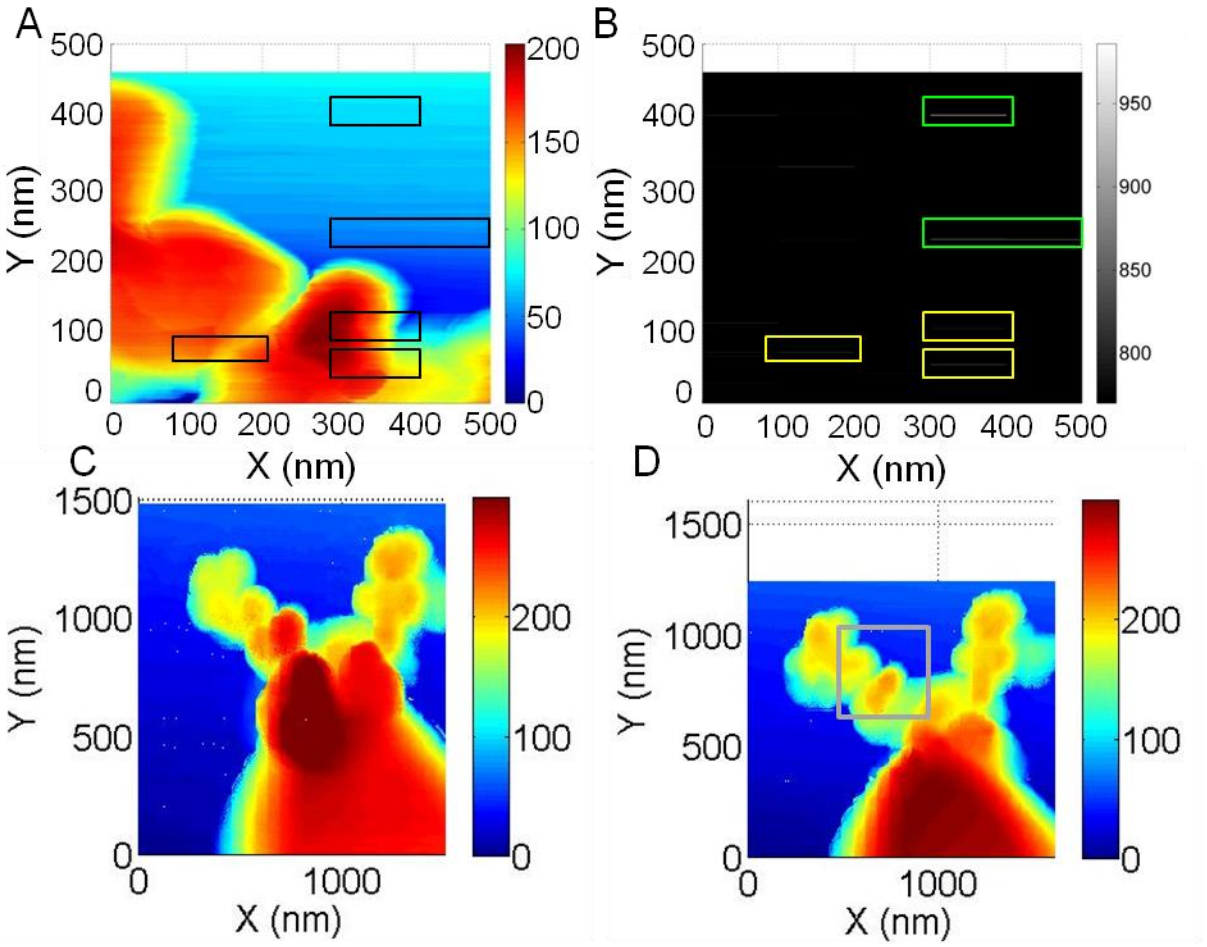

Figure 6.8. (A) Topography of AuNP aggregate from AFM scan, with correlated optical counts from SPAD (B) for high laser intensity CNT-AFM scan of aggregate (3 kW/cm^2). Yellow boxes in (B) indicate aggregate-correlated photon counts, while green boxed areas have no correlation. Panel (C)-(D) show the changing topography of the AgNP aggregate before (C) and after (D) the high intensity laser illumination. Gray box in (D) shows region mapped in (A) and (B). Colorbars in (A), (B), and(C) represent height in nm, while the colorbar in (B) represents SPAD counts/500 ms, where the colorbar minimum is set to 3 standard deviations above the mean.

6.7 Conclusions

In the pursuit of developing a scanning-analyte method of mapping SERS enhancements using our TIR-AFM instrument, we were unable to collect meaningful optical signals from around AgNP aggregates using a CNT-AFM probe. Uncorrelated

signals, poor signal to noise, and lack of intensity bursts were all problems in most scans using this technique. These issues could have been due to the incompatible Raman polarizability of the CNT, which results in a low Raman cross-section for the CNT when illuminated with light polarized in the plane of the sample, or the low probability of finding a nanoparticle aggregate with strong enhancement when searching unlabeled AgNP aggregates.[22,27,30] Additionally, the experiment time (approx 50 minutes for a single scan) makes it very time consuming to scan many aggregates when looking for a "hot" AgNP aggregate on a slide. While we were unable to map SERS enhancements, we were able to develop methods to use TIR microscopy to spectrally characterize the CNT-AFM probe along its length with sub-diffraction-limited resolution using TIR, and to track the oxidation of the CNT-AFM probe *in situ* using Raman spectroscopy.

Throughout this document, the overarching goal of this work has been to gain a deeper understanding of how molecule/nanoparticle interactions affect the emission of SERS. In this work, we have seen that molecule position can affect the far-field emission centroid in SM-SERS, and seen evidence that this is due to the ability of the molecule to couple into different plasmon modes based on its location. We have also applied dipole PSF super-resolution fitting to plasmonic emitters, and shown it to be a useful tool to understand which plasmon modes are emitting, and to get the orientation of certain nanostructures. We also attempted to control the position of the SERS active molecule in these studies by using a CNT-AFM tip to probe SERS enhancements around AgNP aggregates. Hopefully this work has illuminated the impact of the molecule on the emission characteristics of SERS active nanostructures, and helps provide some tools for future studies in this field.

6.8 Acknowledgement

I would like to acknowledge Ifat Kaplan-Ashiri for mentoring me on the use of this instrument, as well as for instruction in making CNT-AFM probes, and her assistance in all of the experiments mentioned in this chapter. I would also like to thank Rachel Shaver for doing some of the initial setup of this instrument, and Beiyue Shao for her work towards chemically functionalizing CNT-AFM probes. Next, I would like to thank the Xidex Corporation of Austin, Texas, for the contribution of carbon nanotubes. This work was supported with funding from DARPA (Grant No. N66001-09-1-2075) as well as startup funds from the University of Texas at Austin.

6.9 References

(1) Alonso-Gonzalez, P.; Schnell, M.; Sarriugarte, P.; Sobhani, H.; Wu, C.; Arju, N.; Khanikaev, A.; Golmar, F.; Albella, P.; Arzubiaga, L.; *et al.* Real-Space Mapping of Fano Interference in Plasmonic Metamolecules. *Nano Lett.* **2011**, *11*, 3922–3926.

(2) Hillenbrand, R.; Keilmann, F.; Hanarp, P.; Sutherland, D. S.; Aizpurua, J. Coherent Imaging of Nanoscale Plasmon Patterns with a Carbon Nanotube Optical Probe. *Appl. Phys. Lett.* **2003**, *83*, 368–370.

(3) Rang, M.; Jones, A. C.; Zhou, F.; Li, Z.-Y.; Wiley, B. J.; Xia, Y.; Raschke, M. B. Optical Near-Field Mapping of Plasmonic Nanoprisms. *Nano Lett.* **2008**, *8*, 3357–3363.

(4) Michaels, A. M.; Jiang; Brus, L. Ag Nanocrystal Junctions as the Site for Surface-Enhanced Raman Scattering of Single Rhodamine 6G Molecules. *J. Phys. Chem. B* **2000**, *104*, 11965–11971.

(5) Stranahan, S. M.; Titus, E. J.; Willets, K. A. SERS Orientational Imaging of Silver Nanoparticle Dimers. *J. Phys. Chem. Lett.* **2011**, *2*, 2711–2715.

(6) Weber, M. L.; Willets, K. A. Correlated Super-Resolution Optical and Structural Studies of Surface-Enhanced Raman Scattering Hot Spots in Silver Colloid Aggregates. *J. Phys. Chem. Lett.* **2011**, *2*, 1766–1770.

(7) Camden, J. P.; Dieringer, J. A.; Wang, Y.; Masiello, D. J.; Marks, L. D.; Schatz, G. C.; Van Duyne, R. P. Probing the Structure of Single-Molecule Surface-Enhanced Raman Scattering Hot Spots. *J. Am. Chem. Soc.* **2008**, *130*, 12616–12617.

(8) Peica, N.; Thomsen, C.; Maultzsch, J. Tip-Enhanced Raman Scattering along a Single Wall Carbon Nanotubes Bundle. *Phys. Status Solidi B* **2010**, *247*, 2818–2822.

(9) Yano, T.; Verma, P.; Saito, Y.; Ichimura, T.; Kawata, S. Pressure-Assisted Tip-Enhanced Raman Imaging at a Resolution of a Few Nanometres. *Nat. Photonics* **2009**, *3*, 473–477.

(10) Woolley, A. T.; Cheung, C. L.; Hafner, J. H.; Lieber, C. M. Structural Biology with Carbon Nanotube AFM Probes. *Chem. Biol.* **2000**, *7*, R193–R204.

(11) Wade, L. A.; Shapiro, I. R.; Ma, Z.; Quake, S. R.; Collier, C. P. Correlating AFM Probe Morphology to Image Resolution for Single-Wall Carbon Nanotube Tips. *Nano Lett.* **2004**, *4*, 725–731.

(12) Wilson, N. R.; Macpherson, J. V. Carbon Nanotube Tips for Atomic Force Microscopy. *Nat. Nanotechnol.* **2009**, *4*, 483–491.

(13) Kaplan-Ashiri, I.; Titus, E. J.; Willets, K. A. In Situ Chemical Functionalization of a Single Carbon Nanotube Functionalized AFM Tip Using a Correlated Optical and Atomic Force Microscope. *MRS Online Proc. Libr.* **2011**, *1318*, null–null.

(14) Yu, M.-F.; Lourie, O.; Dyer, M. J.; Moloni, K.; Kelly, T. F.; Ruoff, R. S. Strength and Breaking Mechanism of Multiwalled Carbon Nanotubes Under Tensile Load. *Science* **2000**, *287*, 637–640.

(15) Stiles, R. L.; Willets, K. A.; Sherry, L. J.; Roden, J. M.; Van Duyne, R. P. Investigating Tip−Nanoparticle Interactions in Spatially Correlated Total Internal Reflection Plasmon Spectroscopy and Atomic Force Microscopy. *J. Phys. Chem. C* **2008**, *112*, 11696–11701.

(16) Axelrod, D.; Burghardt, T. P.; Thompson, N. L. Total Internal Reflection Fluorescence. *Annu. Rev. Biophys. Bioeng.* **1984**, *13*, 247–268.

(17) McKee, K. J.; Smith, E. A. Development of a Scanning Angle Total Internal Reflection Raman Spectrometer. *Rev. Sci. Instrum.* **2010**, *81*, 043106.

(18) Mattheyses, A. L.; Axelrod, D. Direct Measurement of the Evanescent Field Profile Produced by Objective-Based Total Internal Reflection Fluorescence. *J. Biomed. Opt.* **2006**, *11*, 014006–014006–7.

(19) Dresselhaus, M. S.; Dresselhaus, G.; Saito, R.; Jorio, A. Raman Spectroscopy of Carbon Nanotubes. *Phys. Rep.* **2005**, *409*, 47–99.

(20) Dresselhaus, M. S. NT10: Recent Advances in Carbon Nanotube Science and Applications. *ACS Nano* **2010**, *4*, 4344–4349.

(21) Dresselhaus, M. S.; Jorio, A.; Hofmann, M.; Dresselhaus, G.; Saito, R. Perspectives on Carbon Nanotubes and Graphene Raman Spectroscopy. *Nano Lett.* **2010**, *10*, 751–758.

(22) Jorio, A.; Pimenta, M. A.; Filho, A. G. S.; Saito, R.; Dresselhaus, G.; Dresselhaus, M. S. Characterizing Carbon Nanotube Samples with Resonance Raman Scattering. *New J. Phys.* **2003**, *5*, 139.

(23) Maejima, K.; Suzuki, O.; Uchida, T.; Aoki, N.; Tachibana, M.; Ishibashi, K.; Ochiai, Y. Raman and Transport Studies in Multi-Walled Carbon Nanotubes. *J. Phys. Conf. Ser.* **2006**, *38*, 33.

(24) Minati, L.; Speranza, G.; Bernagozzi, I.; Torrengo, S.; Toniutti, L.; Rossi, B.; Ferrari, M.; Chiasera, A. Investigation on the Electronic and Optical Properties of Short Oxidized Multiwalled Carbon Nanotubes. *J. Phys. Chem. C* **2010**, *114*, 11068–11073.

(25) Hao, E.; Schatz, G. C. Electromagnetic Fields around Silver Nanoparticles and Dimers. *J. Chem. Phys.* **2004**, *120*, 357–366.

(26) Halas, N. J.; Lal, S.; Chang, W.-S.; Link, S.; Nordlander, P. Plasmons in Strongly Coupled Metallic Nanostructures. *Chem. Rev.* **2011**, *111*, 3913–3961.

(27) Duesberg, G. S.; Loa, I.; Burghard, M.; Syassen, K.; Roth, S. Polarized Raman Spectroscopy on Isolated Single-Wall Carbon Nanotubes. *Phys. Rev. Lett.* **2000**, *85*, 5436–5439.

(28) Garcia, R.; Martinez, R. V.; Martinez, J. Nano-Chemistry and Scanning Probe Nanolithographies. *Chem. Soc. Rev.* **2006**, *35*, 29–38.

(29) Stranahan, S. M.; Willets, K. A. Super-Resolution Optical Imaging of Single-Molecule SERS Hot Spots. *Nano Lett.* **2010**, *10*, 3777–3784.

(30) Kneipp, K.; Wang, Y.; Kneipp, H.; Perelman, L. T.; Itzkan, I.; Dasari, R. R.; Feld, M. S. Single Molecule Detection Using Surface-Enhanced Raman Scattering (SERS). *Phys. Rev. Lett.* **1997**, *78*, 1667–1670.

(31) Pieczonka, N. P. W.; Aroca, R. F. Inherent Complexities of Trace Detection by Surface-Enhanced Raman Scattering. *ChemPhysChem* **2005**, *6*, 2473–2484.

(32) Link, S.; Burda, C.; Nikoobakht, B.; El-Sayed, M. A. How Long Does It Take to Melt a Gold Nanorod?: A Femtosecond Pump–probe Absorption Spectroscopic Study. *Chem. Phys. Lett.* **1999**, *315*, 12–18.

Appendix 1: Details of Super-Resolution Fitting using a Dipole Emission Model

A1.1 Dipole Emission theory

The super-resolution dipole-emission model fit algorithm is designed to fit the emission from one or more single, isolated dipolar emitters imaged with a high NA objective. This technique is used in place of/in addition to fitting with another point-spread function (PSF) model, such as a 2-dimensional (2-D) Gaussian, in order to localize the emission centroid produced by the dipolar emitters. When imaging a dipole emission pattern, it is known that the orientation of the emitting dipole is captured in the experimental image.[1–4] By fitting this pattern with the appropriate dipole emission model, the dipole orientation, location, emission wavelength, and other parameters can be extracted. In addition to this, the dipole emission model accurately fits the dipole-orientation-linked asymmetry of the emission pattern, which yields improved centroid localization accuracy when compared to a 2-D Gaussian function.[5] While there are many benefits to using a dipole emission model, it is important to note that it is much more complex than a 2-D Gaussian PSF making it more computationally expensive as well as very sensitive to distortions of the dipole emission pattern.

The dipole emission model that is discussed here is derived from the QDControl.m code provided online by Jörg Enderlein, which calculates a theoretical dipole emission pattern based on user-provided dipole orientation and imaging conditions.[6,7] In our work, the program has been modified to fit experimental optical data using user-provided initial guesses and non-linear least-squares minimization, and dipole emission parameters of interest are then extracted from this fit. Anywhere from 8-10 variables are fit during a dipole model fit, depending on the type of model used. Several additional known values need to be verified and input into the model before fitting, such

as the numerical aperture (NA) of the microscope objective, the microscope magnification (as determined *via* a USAF 1951 test target and AFM, see Chapter 2.3), the pixel size of the detector, and the refractive indices of the glass coverslip, microscope immersion oil, and imaging medium. The fit variables are the microscope focus, λ (emission wavelength), ϕ and θ (dipole orientation parameters, see Figure A1.1), κ and R (controls contributions from mutually orthogonal dipole components, see Equation A1.1), x_0 and y_0 (centroid position), I_0 (peak intensity), z_0 (background intensity), as well as the distance of the emission from the slide surface (in some experiments).

In this fitting scheme, we use the angles ϕ and θ (ranging from 0°-360° and 0°-90° respectively) to determine the orientation of the longitudinal dipole mode of the structure; a diagram showing how ϕ and θ are defined is included below in Figure A1.1A. In addition to fitting data to a single dipole (1-dipole model), we can also allow the dipole fit to include two additional orthogonal dipole modes resulting in a 3-dimensional dipole model (3-dipole model). The presence of these orthogonal modes is controlled through the variables R and κ, which are defined below in Equation A1.1.[7]

$$I_{total} = RI_{LM} + (1-R)\left(\frac{1+\kappa}{2} I_{TM} + \frac{1-\kappa}{2} I_{OOP}\right) \qquad \text{(A1.1)}$$

In this equation, I_{total} represents the overall dipole emission vector, where I_{LM}, I_{TM}, and I_{OOP} represent unit vectors along the subscripted axes, which are defined in Figure A1.1B. R is fixed at 1 when fitting data to a 1-dipole model, while R and κ are included as variables in the 3-dipole model.

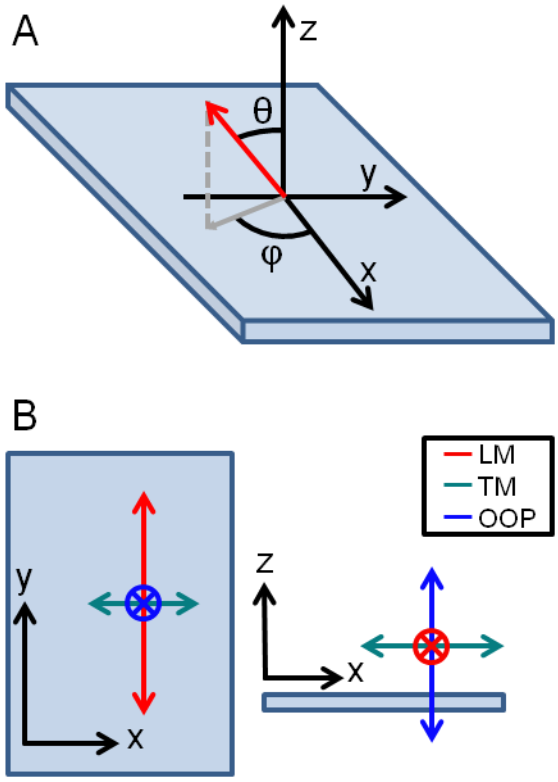

Figure A1.1. Diagram of coordinate axes relative to the sample plane (x-y) and optical axis of the microscope (z). (A) The dipole orientation angles ϕ and θ correspond to the orientation of the LM dipole mode shown in red (B). (B) Definitions of the LM, TM, and OOP dipole modes relative to the coordinate axes with ϕ = 90º/270º and θ = 90º (the in-plane nature of the dipole makes the ϕ value symmetric along the y-axis). Adapted with permission from Titus, E. J.; Willets, K. A. Accuracy of Superlocalization Imaging Using Gaussian and Dipole Emission Point-Spread Functions for Modeling Gold Nanorod Luminescence. *ACS Nano.* **2013**, *7*, 6258-6267. Copyright 2013 American Chemical Society.

A1.2 Data Collection and preprocessing

In most experiments, the dipole model fitting is carried out on several successive frames of the same data acquisition, which requires us to apply a stage drift correction to obtain accurate centroid locations. Typically, fluorescent polystyrene beads are deposited on the substrate near the sample, and data is only collected from dipole emitters in regions where there are two or more beads in the field of view that are capable of being

used to correct the stage drift. To calculate the stage drift correction, the bead centroids are first localized using a 2-D Gaussian function, as shown in Equation A1.2.[8]

$$I(x,y) = z_0 + I_0 e^{\left[-\frac{1}{2}\left[\left(\frac{x-x_0}{s_x}\right)^2 + \left(\frac{y-y_0}{s_y}\right)^2\right]\right]} \qquad \text{(A1.2)}$$

In this equation, z_0, I_0, x_0, and y_0 all represent the same parameters as in the dipole model, while s_x and s_y represent the width of the Gaussian in each dimension. After extracting the centroid position for each bead from each frame of the fit, the centroid shift of the beads is used to generate an average shift for each frame. This process is carried out before any dipole emission fitting takes place, and is carried out with the program Create_Correction.m, which is another in-house MATLAB script. This shift data is applied to the dipole emitter centroids (as determined by the dipole model fit) to correct for the effects of the stage drift on centroid localization. It is also important to note that this method can only counteract slow (~1nm/frame) stage drift; if the stage drift is too fast, it can move the emitter enough during the acquisition of one frame to distort the dipole emission pattern.

A second aspect of the fitting to consider is background subtraction during data pre-processing. Depending on the imaging conditions, background subtraction is often needed due to the intrinsic fluorescence of microscope coverslips, which are commonly used as imaging substrates. Because the experiments discussed here are collected using a widefield excitation geometry, the background appears as a large Gaussian with the dimensions of the laser spot. This is compensated for by taking images from a region of the slide that shows this glass background only (empty of dipole emitters and drift markers), then fitting this background image with Equation A1.2. This fit is then subtracted from the images that were collected of the dipole emitters. This background-

subtraction is typically carried out when the background-to-signal ratio is high enough that it negatively impacts the dipole model fit. If the data necessitates the use of this background subtraction, it is carried out before the drift correction or dipole emission code is run on the data using a separate algorithm.

A1.3 Dipole Emission Fitting

The code used to run the dipole model fitting is named FitLauncherGUI.m, and is written in MATLAB. The main control panel for this script is shown in Figure A1.2. The first step of this code is to read-in the image data (formatted as a TIFF stack) by clicking "Load Image". Next, a region-of-interest (ROI) is selected using the "View Data" button, such that it only encompasses the dipole emission pattern of a single emitter, usually a region of less than 2 microns in image-space. After accepting the ROI, the initial guesses of the fit need to be set, so that the starting point of the model is a close approximation of the experimental data. This step is important because due to its complexity, the model can converge to a false minimum or take too long to iterate to the global minimum of the fit. In order to quickly generate accurate initial guesses, the first frame of the data is initially fit to a rotated asymmetric 2-D Gaussian function, shown below in Equation A1.3.

$$I(x,y) = z_0 + I_0 e^{\left[-\frac{1}{2}\left[\left(\frac{\cos^2\phi}{\sigma_x^2}+\frac{\sin^2\phi}{\sigma_y^2}\right)(x-x_0)^2+\left(\frac{-\sin(2\phi)}{\sigma_x^2}+\frac{\sin(2\phi)}{\sigma_y^2}\right)(x-x_0)(y-y_0)+\left(\frac{\sin^2\phi}{\sigma_x^2}+\frac{\cos^2\phi}{\sigma_y^2}\right)(y-y_0)^2\right]\right]} \quad \text{(A1.3)}$$

The parameters in this equation are the same that are in the 2-D Gaussian equation (Equation A1.2), with the addition of the parameter ϕ, which determines the rotation of the asymmetric Gaussian. This fit is applied using the "Gaussian pre-fit" control, and can be run on a single frame in approximately 1 second, giving good initial estimates of x_0,

y_0, I_0, z_0 and ϕ. Following this fit, ϕ is also checked by eye, as the in-plane and out-of-plane orientation of the dipole can be visually estimated, as shown in Figure A1.3A-B. This is accomplished by visually comparing the model image (middle frame, Figure A1.2) to the experimental data (top frame, Figure A1.2). The rest of the guesses, lower boundaries and upper boundaries for each optimizable fit parameter are then set using the text entry boxes shown on the panel in Figure A1.2. The defocus guess is typically set to 0 μm for these studies, as the microscope was focused before image collection. In the cases where a 1-dipole fit (LM mode) is desired, R is locked at 1, and κ is locked at an arbitrary value. This is done for any variable by simply setting the initial guess, upper boundary, and lower boundary to the same value. For 3-dipole fits (LM, TM, OOP modes), the initial guesses for R and κ need to be set according to the predicted mode contributions of the nanostructure. It should be noted that even in the case of highly anisotropic particles such as gold nanorods, the 3-dipole model provides better fits to the data than the 1-dipole mode. In the studies presented in this document, the particles under investigation have very strong contributions from the LM mode, therefore initial guesses for R are typically set between 0.9-1 (depending on the R^2 of the starting model), with the κ guess starting at 0. The λ guess is set based on an estimate of the emission peak (*e.g.* from ensemble measurements). Finally, the θ guess is typically set to 90° when fitting most emission patterns, unless they show a strong out-of-plane tilt, as shown in Figure A1.3C-D. In the course of our research, we have not seen that setting the θ initial guess to 90° impacts the optimized fit model. For all fit frames after the initial frame, the initial guesses are taken from the fit estimates of the previous frame. After these parameters are set, the ROI should be assigned a name ("Mol. Name" control), and additional ROIs can be defined from the same image stack by selecting "View Data".

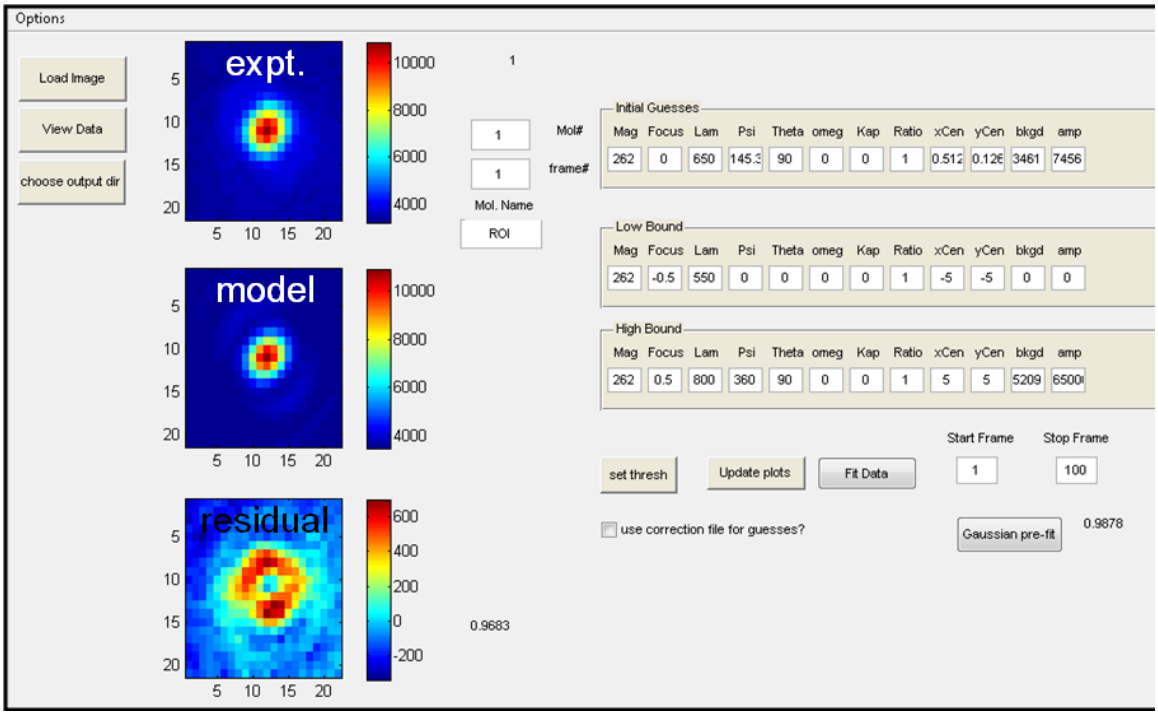

Figure A1.2. FitLauncherGUI.m control panel.

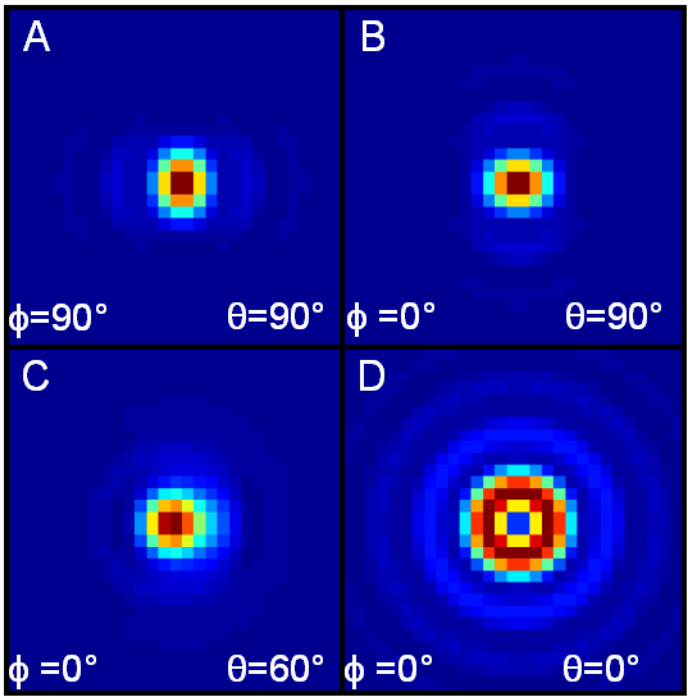

Figure A1.3. Calculated images showing emission from dipoles at different orientations. All images show 1-dipole models (R= 1).

Because most of the plasmonic nanostructures imaged in the dipole emission studies discussed in this document are all nearly planar, *i.e.* θ≈90°, it can often be difficult to assign a correct ϕ guess (ϕ_{guess}), due to the apparent symmetry of the emission pattern. As shown in Figure A1.4, the emission patterns of dipoles with θ values of 85° results in a slightly asymmetric image without a clear indication of whether ϕ_{guess} should be set below or above 180°. This causes problems in the fits because the patterns are not identical, and if the wrong ϕ_{guess} value is used, the fit will converge to a local minimum near the ϕ_{guess}, instead of rotating 180° to converge at ϕ_{guess}+180°. Typically when this happens, the fit estimate for θ will be at 90° for all fit frames, as this gives the best R^2 value when ϕ is off by 180°. In order to address this problem, each ROI needs to be fit using a ϕ_{guess} between 0° and 180° that appears to match the data, as well as ϕ_{guess} +180°.

This is carried out by the user by setting ϕ_{guess} for the ROI, then selecting "make duplicate region" from the "Options" menu. This creates a copy of the current ROI, including initial guesses and boundaries. In the copied ROI (be sure to assign it a unique name using "Mol. Name"), simply set the new ϕ_{guess} to ± 180° of the original guess. Once the fit has been carried out, the θ values from the two fits are compared, and the fit with θ values below 90° are chosen.

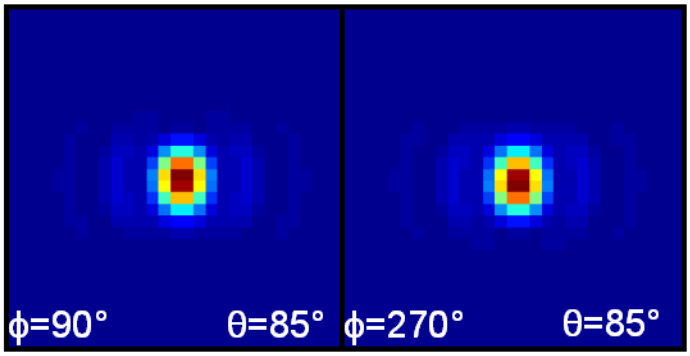

Figure A1.4. Theoretical images showing emission from nearly planar dipoles with ϕ values of 90° and 270°. Patterns are difficult to distinguish by eye. Both images are 1-dipole models (R=1)

In addition to the fit steps described previously, there are additional procedures that can reduce the amount of time that it takes to fit the data (the median fit time for a 1-dipole fit is between 5-10 minutes a frame, while a 3-dipole fit typically takes 10-20 minutes per frame). Because of this, only 10-20 data frames are fit at one time. This is accomplished through short data acquisitions, or selecting a subset of a larger acquisition, either sequentially or randomly, depending on the experiment. If a subset of frames needs to be fit, a contiguous series of frames can be fit by setting appropriate "Start Frame" and "Stop Frame" values. Next, it is important to make sure that the starting guesses for each optimization are as close as possible to their minimized values. For the first frame, this is accomplished by having the user adjust the initial guesses until the error between the fit

and the data is minimized (R^2 greater than 0.95 in many cases). For subsequent frames, initial guesses for frames in a stack are set as the optimized values of the previously fit frame, and the initial guesses for x_0 and y_0 are based on both the previous frame estimates and the stage drift correction data (check the "use correction file for guesses?" control). Once all initial guesses and boundaries are set, the fit can be run by clicking "Fit Data". Output data will go to the directory selected with "choose output dir" button.

Once the fitting of the data is complete, the data is checked first by examining the fit residuals (the difference between the experimental image and the fitted model). The residual image is visually inspected to check for signs of non-random patterns, which indicate that the fit model does not match the experimental data. In our experiments, we also checked that the optimized dipole orientation and λ values matched the experimentally determined structure and emission wavelength of our nanoparticle samples. Additionally, we also compare the centroid localization between the dipole and 2-D Gaussian models.

A1.4 Acknowledgement

I would like to acknowledge Prof. Jörg Enderlein for making his QDControl.m code available online, as this fitting program is based off of this model. The Create_Correction.m code was originally written by Prof. Kallie Willets, and updated by Karole Blythe.

A1.5 References

(1) Bartko, A. P.; Dickson, R. M. Imaging Three-Dimensional Single Molecule Orientations. *J. Phys. Chem. B* **1999**, *103*, 11237–11241.

(2) Bartko, A. P.; Dickson, R. M. Three-Dimensional Orientations of Polymer-Bound Single Molecules. *J. Phys. Chem. B* **1999**, *103*, 3053–3056.

(3) Hellen, E. H.; Axelrod, D. Fluorescence Emission at Dielectric and Metal-Film Interfaces. *J. Opt. Soc. Am. B* **1987**, *4*, 337–350.

(4) Dickson, R. M.; Norris, D. J.; Moerner, W. E. Simultaneous Imaging of Individual Molecules Aligned Both Parallel and Perpendicular to the Optic Axis. *Phys. Rev. Lett.* **1998**, *81*, 5322–5325.

(5) Enderlein, J.; Toprak, E.; Selvin, P. R. Polarization Effect on Position Accuracy of Fluorophore Localization. *Opt. Express* **2006**, *14*, 8111–8120.

(6) Enderlein, J. Imaging of Single Molecules http://www.joerg-enderlein.de/imagingOfSingleMolecules.html (accessed May 3, 2013).

(7) Patra, D.; Gregor, I.; Enderlein, J.; Sauer, M. Defocused Imaging of Quantum-Dot Angular Distribution of Radiation. *Appl. Phys. Lett.* **2005**, *87*, 101103–101103–3.

(8) Stranahan, S. M.; Titus, E. J.; Willets, K. A. SERS Orientational Imaging of Silver Nanoparticle Dimers. *J. Phys. Chem. Lett.* **2011**, *2*, 2711–2715.

Appendix 2: Atomic Force Microscope Mapping of Optically-Induced Forces around Plasmonic Nanoparticles

A2.1 Introduction

In optical trapping, optical forces are typically broken down into two types. The first type of optical force is known as radiation pressure, which is the force due to the momentum transfer of the photons to an object that is scattering or absorbing light. The other type of force is known as the gradient force, which is the main optical force responsible for trapping. This force is proportional to the electric field gradient of the trapping beam, such that stronger field gradients yield stronger optical trapping (more force).[1,2] Because of this field gradient dependence, optical trapping experiments are a natural match for plasmonic nanostructures.[3]

Plasmonically-assisted optical trapping has recently been investigated for use in techniques such as chemical sensing,[4] nano-manipulation,[5–7] and biological imaging[8,9] due to its many advantages over traditional lens-based methods.[3] The advantages are due to the strongly enhanced electric fields and field-gradients that can be generated at the surface of a plasmonic structure upon illumination. These fields can trap particles and molecules with just a fraction of the laser power needed in traditional optical traps.[7] Because this technique does not rely on far-field optics to focus the trap, it also is well suited for applications in "lab-on-a-chip" detection schemes, where analytes can be immobilized on plasmonic optical traps and then detected *via* plasmon enhanced spectroscopies.[9]

Another area of recent interest in this field is to determine how these strong optical forces may affect the molecule-nanoparticle interactions in surface-enhanced spectroscopy substrates such as those used for single-molecule surface-enhanced Raman scattering (SM-SERS). Due to the confined nature of the electric fields, particles that

support strong SERS enhancement should also yield strong optical trapping of molecules.[10,11] This is an interesting concept, as it could provide an explanation of how analyte molecules find their way to the "hot spots" that provide the enhancement necessary to observe SM-SERS.[12]

In order to understand and best take advantage of the strong trapping at plasmonic nanostructures, it is important to be able to map the optical forces around these structures with high spatial resolution. Due to the nanometric size scale of the plasmonic structures used in optical trapping and their even-smaller regions of field enhancement, traditional methods of mapping optical forces, such as those using microbead probes, may not provide adequate spatial resolution to give insight into the spatial distribution of the optical force.[13,14] To measure these forces with relevant spatial resolution, we have adapted techniques used by Kohoutek *et. al.* in order to map optical forces around nanoparticle structures.[15] In this technique, an atomic force microscope (AFM) is used to measure the optical forces around a nanostructure as it is exited by a coupled optical microscope system. We have modified this experiment such that it can be carried out on our combination total-internal reflection/atomic force microscope setup (TIR/AFM), which was described in Chapter 2. In this Appendix, we first show our attempts at mapping the evanescent field gradient generated by the TIR excitation of the microscope, which was performed as a test of the optical force mapping method. Next, we show experiments where we attempted to map optical forces around both a single gold nanoparticle and a gold nanoprism.

A2.2 Evanescent wave mapping

Prior to using the AFM optical force mapping technique on plasmonic nanoparticles, the optical force generated by the evanescent field of the TIR microscope was measured to determine the sensitivity of the AFM to optical forces, as well as

measure the optical force background due to the excitation from the microscope. The optical forces in this study originate from the evanescent field gradient of the TIR excitation, as given by Equation A2.1.[16,17]

$$I(z) = I_0 e^{-z/d} \tag{A2.1}$$

In this equation, the distance dependent intensity of the evanescent field is given as I, the intensity at the interface as I_0, the distance from the surface as z, and the characteristic decay length (or penetration depth) of the evanescent field as d. The penetration depth of the field is given below in Equation A2.2.

$$d = \frac{\lambda}{4\pi}\left(n_1^2 \sin^2\theta - n_2^2\right)^{-1/2} \tag{A2.2}$$

As shown above, d is a function of the wavelength of the totally-internally reflected light, the refractive indices at the TIR interface (n_1 and n_2, representing the refractive indicies of glass and air, respectively), and the angle of incidence of the light. This means that in a TIR microscope, the penetration depth of the field can be easily tuned by adjusting the incidence angle of the light. The expected optical trapping force associated with the evanescent field gradient can be estimated from the gradient force equation expressing the force on a point dipole, shown in Equation A2.3.[1]

$$F = \frac{1}{2}\alpha \nabla E^2 \tag{A2.3}$$

This equation gives the optical gradient force as a function of the polarizablitiy of the trapped particle (α), and the gradient of the square of the electric field (∇E^2). In the case of an AFM probe, the end of the probe is sufficiently small compared to the wavelength

of light that we feel comfortable utilizing Equation A2.3 to model the gradient force on the probe.

A brief schematic of the experimental setup for evanescent field force mapping is given below in Figure A2.1A, with a more detailed schematic of the system given in Chapter 2. In this setup, the AFM head is positioned over the laser focus of the TIR microscope, such that the AFM probe is in the center of the excitation field. The Si probes used for this study are made for contact mode imaging (NT-MDT CSG01), and have a small spring constant in order to be more sensitive to any optical forces present. An experiment is executed by first placing a clean glass slide in contact with the oil immersion objective to act as the TIR interface of the microscope and as a substrate to land the AFM probe on. Next, an isolation hood is placed on the AFM microscope setup and purged with dry N2 for several hours to dry out the sample and AFM probe; this prevents the typical adhesion seen between the probe and sample due to the water meniscus formed by ambient humidity levels.[18] To map the evanescent field, we run a standard AFM force *vs* distance curve with the AFM probe centered in the excitation field. In this process, the AFM tip starts in contact with the slide, is raised to a certain height from the surface, and is finally brought to the surface while the probe deflection is monitored. The optical forces acting on the AFM probe are detected by measuring the deflection of the AFM probe as it approaches the surface.

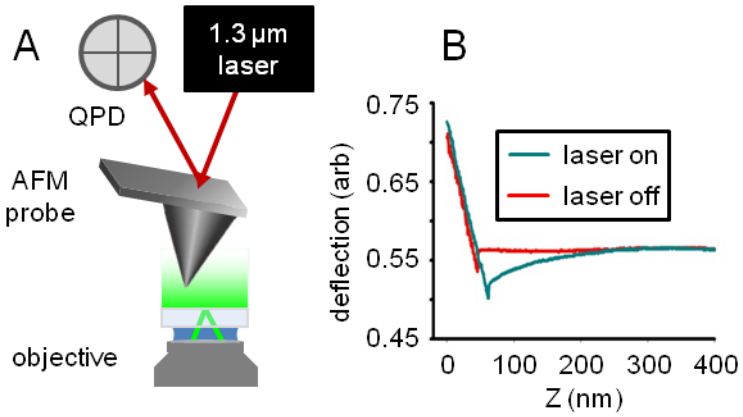

Figure A2.1 . (A) Block diagram of TIR optical force mapping setup. QPD: four-quadrant photodiode. (B) Plot of tip deflection versus AFM piezo Z-extension (zero is arbitrary) for laser-on and laser-off cases. Larger values of Z indicate that the probe is farther from the surface.

An example of a typical AFM contact mode approach curve collected with this experimental setup is shown in red (no laser illumination) in Figure A2.1B. In this type of approach curve, we can see that as the probe approaches the surface, it does not deflect until it reaches the attractive van der Waals force regime near the surface of the material and snaps into contact. When the experiment is repeated with the added illumination from the evanescent field, we see (Figure A2.1B) that the tip is negatively deflected indicating that it bends toward the surface as it approaches. If this effect is due to the optical gradient force, the force on the AFM probe (i.e. deflection) should track the derivative of the evanescent field decay (given in Equation A2.3). To test this relationship, we proceeded to fit the AFM approach curve data with Equation A2.4. This equation is based on Equation A2.3, where we have replaced ∇E^2 with $\nabla I(z)$, where $I(z)$ is taken from Equation A2.1.

$$DFL(z) = DFL_0 + \beta e^{-z/d_{fit}} \qquad \text{(A2.4)}$$

Here, *DFL(z)* indicates the height dependent deflection of the AFM probe, with DFL_0 representing the base-level deflection reading of the probe in free space. The DFL value is used here as it is proportional to the force on the cantilever, which can be calculated through the contact-region of the approach curve. The value β represents the exponential scaling term, which encompasses the AFM probe polarizability as well as force conversion factors. The penetration depth d_{fit} is the depth of the evanescent field as determined by the fit. If the data is well modeled by this curve, the force on the probe is likely due to the optical gradient force. When fitting approach curves with this function, we are careful to only include data outside the range of the van der Waals forces, so that surface interaction forces do not skew our results.

One problem that arises when fitting the AFM approach data to Equation A2.4 is that the only fit parameter that is both easy to check experimentally and meaningful is d_{fit}. While fitting the data to this model resulted in good R^2 values, the value of d_{fit} obtained from the model fit was too low. In order to understand why, we applied this fit to approach curves taken under different experimental conditions, as shown in Figure A2.2. The first relationship that we tested was the effect of laser power on the scaling factor (β) that is determined for the data from a fit to Equation A2.4. Here, we see a nearly linear relationship between β and the incident laser power used to excite the evanescent field, which matches our expectations. Next, we test the value of d_{fit} *vs* both the incident laser power and the measured penetration depth, shown in Figure A2.2B-C. In Figure A2.2B, we see that the value of d_{fit} changes significantly when the laser power is tuned over an order of magnitude for both p- and s-polarizations. Based on the force gradient of the evanescent field shown in Equation A2.4 and the fact that the penetration depth should not be affected by laser power (Equation A2.2), this result doesn't match the optical force gradient model that we have calculated for this system. We again see data that doesn't

match the expected trend in Figure A2.2C as we compare the d_{fit} values with those calculated from Equation A2.2 shown in blue.

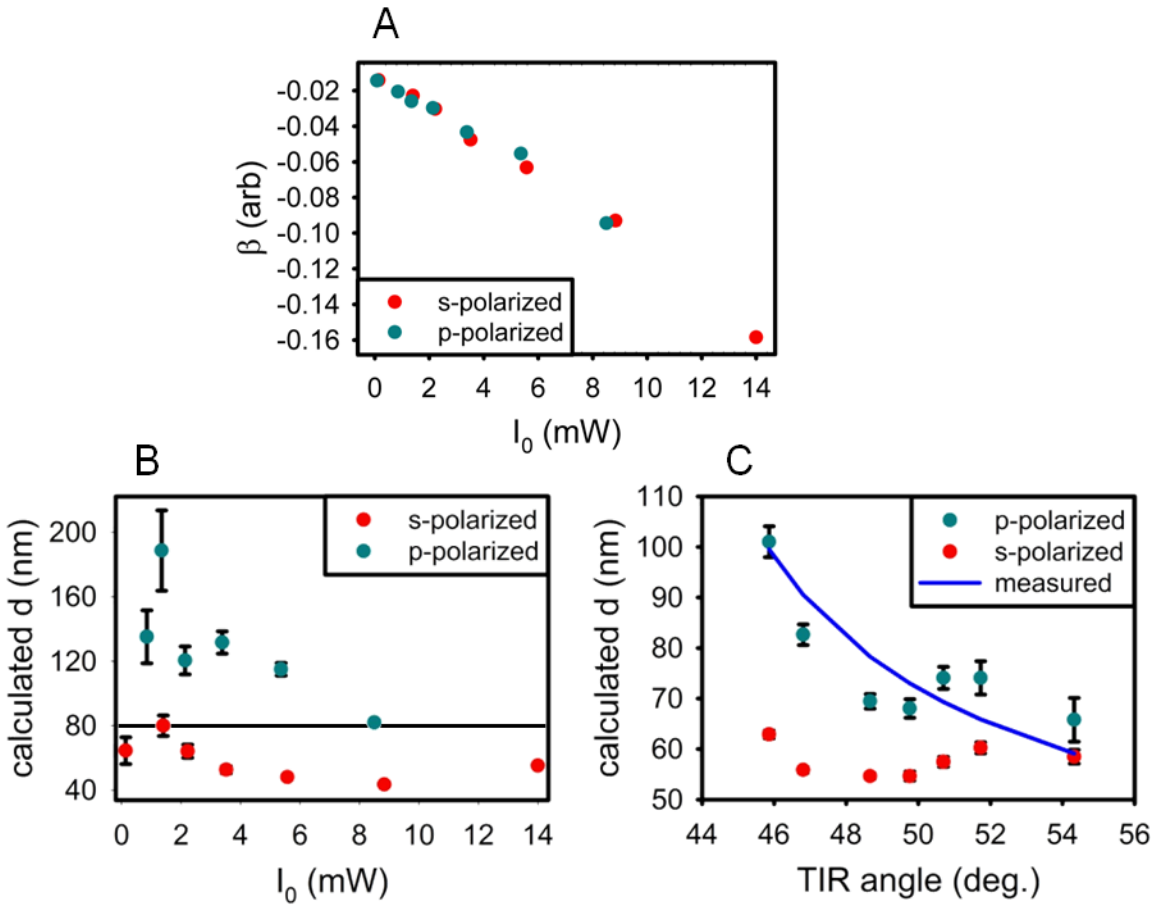

Figure A2.2. (A) Plot showing how the scaling factor described in Equation A2.4 scales with incident laser power for both p- and s-polarized excitation. (B) Data showing the relationship between the calculated penetration depth of the field based on an approach curve fit *vs* incident laser power. The penetration depth based on the measured TIR angle is shown with a black line. (C) Plot comparing the changes in penetration depth as calculated from the approach curve fits to the TIR angle. The blue line shows the penetration depth as calculated from Equation A2.2.

As can be seen from the fit-derived error bars, the experimental data is well fit by the model with higher error due to low force signals at lower powers. Understanding that this discrepancy is not just due to a poor fit, there are several other possibilities that could

explain the discrepancies between the data shown in Figure A2.2 and the model used to fit the data (Equation A2.4). One assumption made in the model is that the AFM probe is small compared to the wavelength of light generating the evanescent field. While this is true for the end of the AFM probe, which should have a 10-30 nm radius, it is still conical, meaning that as the probe nears the surface, a significantly larger portion of the probe is interacting with the evanescent field; this will also affect the probe's polarizability, which is not accounted for in the model. Another possible source of error is that the measured height of the probe is based on the z-piezo motion only, not the actual position of the probe. When the probe is attracted to the surface by the evanescent field, it causes the probe to bend towards the surface (by up to 10 nm), and this difference in probe height is not reflected in the z-piezo measurement. Additionally, radiation pressure could be playing a role in disrupting the model, or we could be dealing with additional problems due to the laser-heating of the silicon AFM probe.

A2.3 Mapping optically-induced forces around plasmonic nanoparticles

After our attempts to measure the optical force gradient induced by the evanescent field of the microscope, we attempted to measure forces around single plasmonic nanoparticles. Due to the confined, strongly enhanced fields at the nanoparticle surface, any optical forces present around the nanoparticles should be much stronger than those measured in the evanescent field in the previous section. To do this, we use a different AFM technique than in the previous section, which is modeled on the technique discussed in reference 15.[15] A block diagram of the AFM/microscope setup is shown below in Figure A2.3A. In this method, we switched to using the semi-contact mode of the AFM, where a stiffer, oscillating silicon tip (NT-MDT NSG30) is used to measure the topography of the sample. The laser excitation intensity of the sample is then modulated via an acousto-optic modulator (AOM), while we use a separate lock-in amplifier to

detect any deflection of the AFM cantilever at the laser modulation frequency. The frequency of the laser modulation is set to overlap with the second resonance frequency of the cantilever, as shown below in Figure A2.3B, which is done to enhance the force detection sensitivity.[19–21] When using this method, it is very important to ensure that the beam used to excite the sample is completely in TIR, as any non-evanescent light-leakage from the excitation beam could easily hit the QPD, giving spurious signals from the lock-in amplifier. Sample preparation for these experiments is similar to those described in Chapter 2.

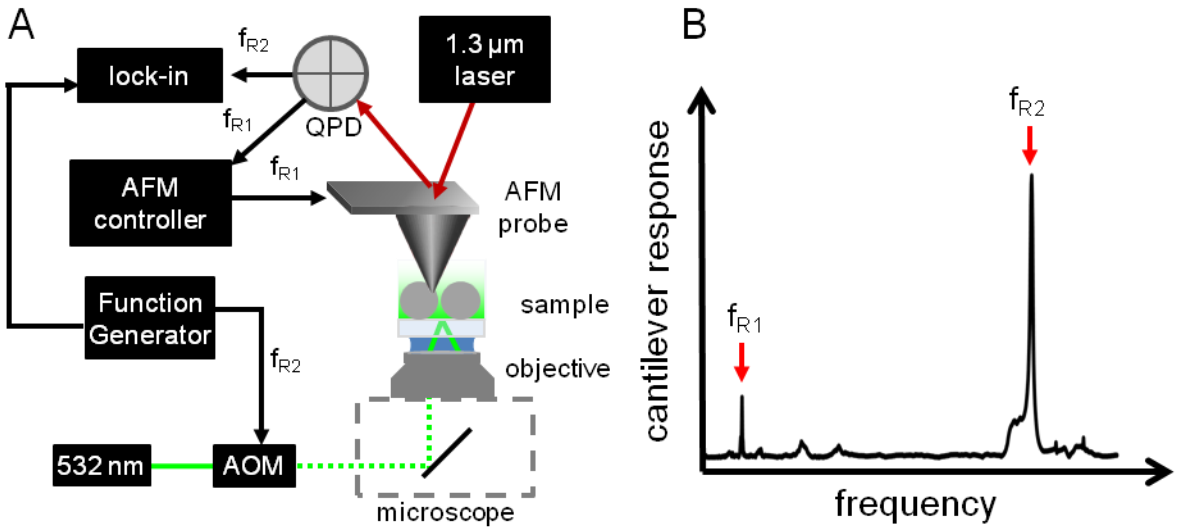

Figure A2.3. A) Block diagram of optical force mapping microscope. AOM: acousto-optic modulator, QPD: four-quadrant photodiode. B) Typical frequency response of a 40 N/m tapping mode AFM cantilever. The first and second resonance frequencies are indicated by the red arrows, and correspond to the frequencies used in A.

Figure A2.4 shows an example of the data collected from an experiment on a 70 nm gold nanosphere (topography shown in A2.4A, and darkfield scattering shown in A2.4G). The data shown in Figure A2.4B is the correlated optical force data from the

lock-in amplifier, taken with the laser off to check that there are no cantilever oscillations at the second resonance frequency (f_{R2}) as the probe is used to map the nanoparticle topography without laser excitation. Figures A2.4C-F show the cantilever phase at f_{R1} and its amplitude at f_{R2} during scans under modulated laser illumination. The phase measurements (panels C and E) show the oscillation phase of the AFM probe, which should be at 90° when there is no force acting on the probe (black line on colorbars in Figures A2.4C and E). This phase measurement indicates how close the probe is to the surface. As the probe gets close to the surface, it experiences the repulsive regime of the surface interaction forces, which shifts the phase towards 0°. When the tip is farther away from the surface but still in the attractive regime of the surface interaction forces, the phase shift will be above 90°.[22] These phase maps are collected at the same time as the optical force maps shown in Figure A2.4B, D and F are measured (shown in arbitrary units).

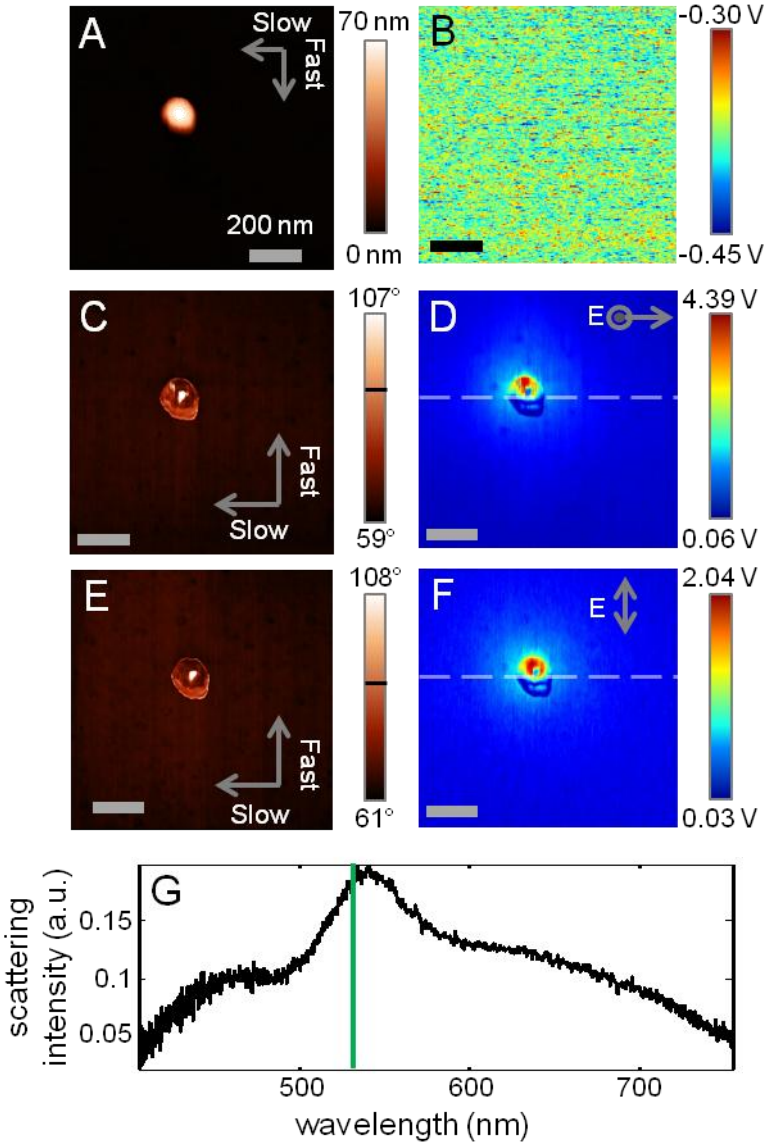

Figure A2.4. (A-B) AFM topography image (A) of single gold nanoparticle (AuNP) with (B) simultaneously detected force map collected at f_{R2}, without laser excitation. (C-D) AFM phase (C) and laser-induced force (D) images for p-polarized excitation. Arrows on phase image indicate scan direction. (E-F) AFM phase (E) and laser-induced force images for s-polarized excitation. Dashed lines indicate cross sections shown in Figure A2.5. (G) Darkfield scattering spectra of AuNP shown in (A) (green line indicates excitation wavelength).

Upon first inspection of the optical force maps shown in Figure A2.4, we notice several characteristics that do not match with how we expect optical forces should behave around nanoparticles. The first notable feature is that the AFM probe seems to be experiencing forces at distances over 200 nm away from the particle, which is unexpected due to the strongly confined field enhancement associated with plasmonic particles. This effect can be seen more clearly in the cross sections of the force maps of the particle shown in Figure A2.5, taken along the lines indicated in Figure A2.4D and F. These maps show a steady fall-off of optical force signal as the tip moves away from the particle. Additionally, the position of the field enhancement around the nanoparticle should change with different excitation polarizations,[23–25] which is again not reflected in the force measurements as seen in both the 2-D force map and cross-sectional data. In addition to these observations, we also see sudden dips in the force map data corresponding to positions on the nanoparticle where the cantilever phase spikes. These phase spikes are indicative of the probe coming far enough off of the surface to leave the repulsive regime of the surface-interaction forces. This causes dips in the force measurement because the tip may not be close enough to the particle to interact with the plasmonically enhanced electric fields. All of these data indicate that the AFM probe is mapping out forces that are occurring at the laser frequency and are optically mediated, but nothing measured matches the expectations of what optical forces should look like around these nanostructures.

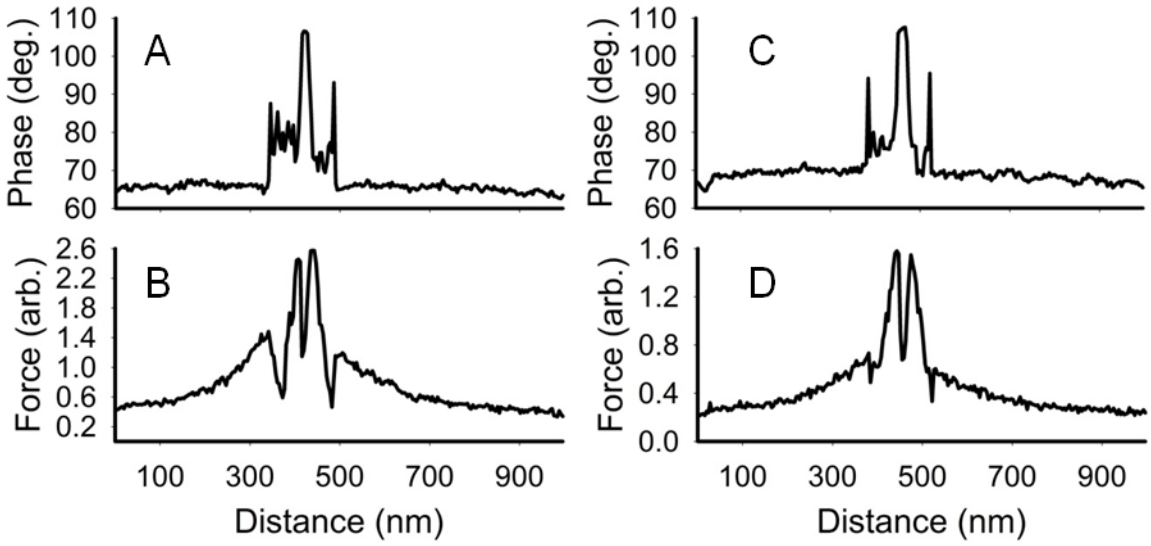

Figure A2.5. (A) AFM phase and B) optically induced force cross section for p-polarized excitation of particle shown in Figure A2.4C-D. Cross-section position is indicated in Figure A2.4D C) AFM phase and D) optically induced force cross section of s-polarized excitation of particle shown in Figure A2.4E-F. Cross section is indicated in Figure A2.4F.

In order to ensure that the effects seen in Figures A2.4-A2.5 were not all due to the shape of the nanoparticle used, we also collected optical force map data on a gold nanoprism, shown in Figure A2.6. Again, we see optical force maps with similar effects to what has been measured on the single nanosphere, even though the particle is excited well off-resonance (Figure A2.6G). The force maps in Figure A2.6D and A2.6F again show forces at the optical modulation frequency acting on the probe at distances too far away from the nanoprism for them to be the optical gradient force. Although these effects are still present, this structure has a much flatter topography, which makes scanning the structure without the probe losing contact much more likely and less prone to the topography/optical force signal convolution problem that was seen on the gold nanosphere.

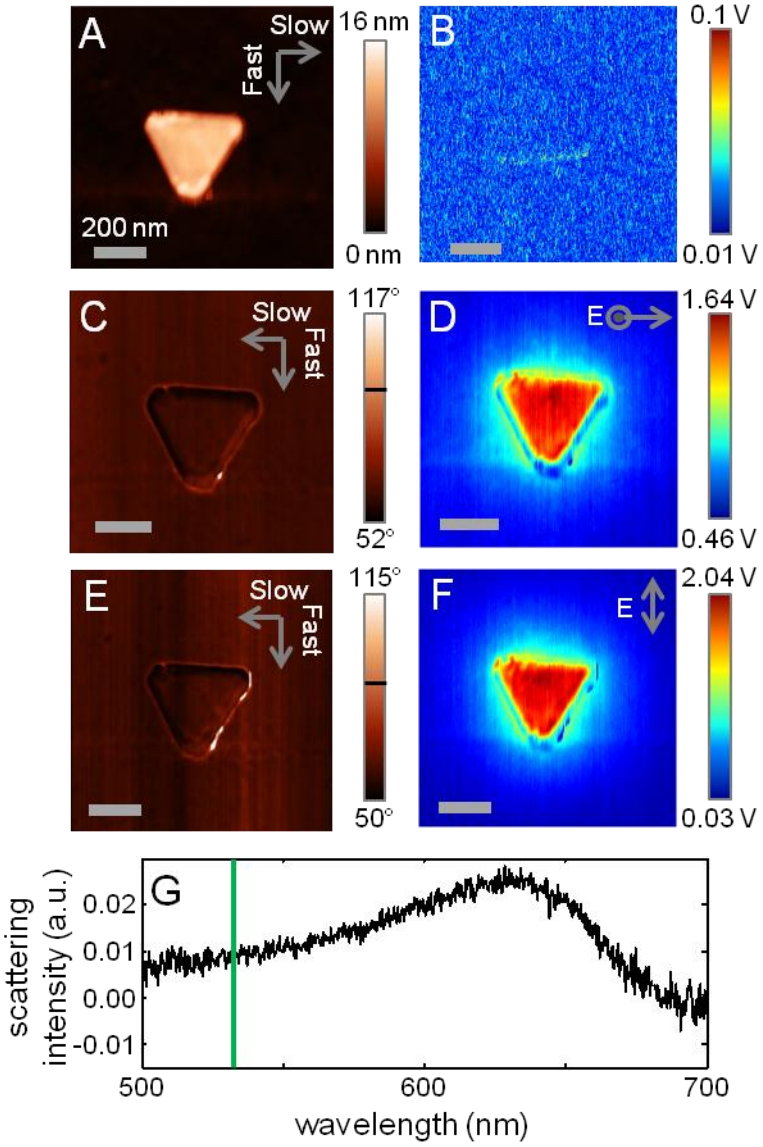

Figure A2.6. (A) AFM topography image of single gold nanoprism. (B) Simultaneously detected force map collected at f_{R2}, without laser excitation. (C & D) AFM phase (C) and laser-induced force (D) images for p-polarized excitation. Arrows on phase image indicate scan direction. (E & F) AFM phase (E) and laser-induced force images for s-polarized excitation (G) Darkfield scattering spectra of the nanoprism shown in (A) (green line indicates excitation wavelength).

A2.4. Conclusions

In the course of trying to map the optical forces around plasmonic nanoparticles using our combined TIR/AFM system, we have consistently seen excitation-mediated forces acting on the AFM probe that do not follow the expected models that govern the optical gradient force. Whether this is due to convolution between the electric field gradients associated with the evanescent field of the particle and the AFM probe or if there are forces other than the optical gradient force playing a role is unclear at this time. Other possible excitation-mediated effects that could be influencing this data include radiation pressure, thermal effects, or light-induced electrostatic effects such as surface photovoltage.[26,27] While we do not yet have a complete understanding of what forces are acting on the AFM probe, the AFM methods here are sensitive enough to detect these forces with high signal-to-noise while simultaneously mapping the topography of nanoparticles.

A2.5. Acknowledgements

I would like to acknowledge Beiyue Shao for assistance with all experiments presented in this appendix.

A2.6. References

(1) Svoboda, K.; Block, S. M. Biological Applications of Optical Forces. *Annu. Rev. Biophys. Biomol. Struct.* **1994**, *23*, 247–285.

(2) Dholakia, K.; Reece, P.; Gu, M. Optical Micromanipulation. *Chem. Soc. Rev.* **2007**, *37*, 42–55.

(3) Righini, M.; Girard, C.; Quidant, R. Light-Induced Manipulation with Surface Plasmons. *J. Opt. Pure Appl. Opt.* **2008**, *10*, 093001.

(4) Gelfand, R. M.; Bruderer, L.; Mohseni, H. Nanocavity Plasmonic Device for Ultrabroadband Single Molecule Sensing. *Opt. Lett.* **2009**, *34*, 1087.

(5) Berthelot, J.; Aćimović, S. S.; Juan, M. L.; Kreuzer, M. P.; Renger, J.; Quidant, R. Three-Dimensional Manipulation with Scanning near-Field Optical Nanotweezers. *Nat. Nanotechnol.* **2014**, *9*, 295–299.

(6) Righini, M.; Volpe, G.; Girard, C.; Petrov, D.; Quidant, R. Surface Plasmon Optical Tweezers: Tunable Optical Manipulation in the Femtonewton Range. *Phys. Rev. Lett.* **2008**, *100*, 186804.

(7) Juan, M. L.; Righini, M.; Quidant, R. Plasmon Nano-Optical Tweezers. *Nat. Photonics* **2011**, *5*, 349–356.

(8) Righini, M.; Ghenuche, P.; Cherukulappurath, S.; Myroshnychenko, V.; García de Abajo, F. J.; Quidant, R. Nano-Optical Trapping of Rayleigh Particles and Escherichia Coli Bacteria with Resonant Optical Antennas. *Nano Lett.* **2009**, *9*, 3387–3391.

(9) Huang, L.; Maerkl, S. J.; Martin, O. J. Integration of Plasmonic Trapping in a Microfluidic Environment. *Opt. Express* **2009**, *17*, 6018–6024.

(10) Xu, H.; Käll, M. Surface-Plasmon-Enhanced Optical Forces in Silver Nanoaggregates. *Phys. Rev. Lett.* **2002**, *89*, 246802.

(11) Miljković, V. D.; Pakizeh, T.; Sepulveda, B.; Johansson, P.; Käll, M. Optical Forces in Plasmonic Nanoparticle Dimers†. *J. Phys. Chem. C* **2010**, *114*, 7472–7479.

(12) Stranahan, S. M.; Willets, K. A. Super-Resolution Optical Imaging of Single-Molecule SERS Hot Spots. *Nano Lett.* **2010**, *10*, 3777–3784.

(13) Knöner, G.; Ratnapala, A.; Nieminen, T. A.; Vale, C. J.; Heckenberg, N. R.; Rubinsztein-Dunlop, H. Optical Force Field Mapping in Microdevices. *Lab. Chip* **2006**, *6*, 1545–1547.

(14) Volpe, G.; Quidant, R.; Badenes, G.; Petrov, D. Surface Plasmon Radiation Forces. *Phys. Rev. Lett.* **2006**, *96*, 238101.

(15) Kohoutek, J.; Dey, D.; Bonakdar, A.; Gelfand, R.; Sklar, A.; Memis, O. G.; Mohseni, H. Opto-Mechanical Force Mapping of Deep Subwavelength Plasmonic Modes. *Nano Lett.* **2011**, *11*, 3378–3382.

(16) Axelrod, D.; Burghardt, T. P.; Thompson, N. L. Total Internal Reflection Fluorescence. *Annu. Rev. Biophys. Bioeng.* **1984**, *13*, 247–268.

(17) McKee, K. J.; Smith, E. A. Development of a Scanning Angle Total Internal Reflection Raman Spectrometer. *Rev. Sci. Instrum.* **2010**, *81*, 043106.

(18) Garcia, R.; Martinez, R. V.; Martinez, J. Nano-Chemistry and Scanning Probe Nanolithographies. *Chem. Soc. Rev.* **2006**, *35*, 29–38.

(19) Rajapaksa, I.; Uenal, K.; Wickramasinghe, H. K. Image Force Microscopy of Molecular Resonance: A Microscope Principle. *Appl. Phys. Lett.* **2010**, *97*, 073121.

(20) Rajapaksa, I.; Wickramasinghe, H. K. Raman Spectroscopy and Microscopy Based on Mechanical Force Detection. *Appl. Phys. Lett.* **2011**, *99*, 161103.

(21) Garcia, R.; Herruzo, E. T. The Emergence of Multifrequency Force Microscopy. *Nat. Nanotechnol.* **2012**, *7*, 217–226.

(22) Noy, A.; Sanders, C. H.; Vezenov, D. V.; Wong, S. S.; Lieber, C. M. Chemically-Sensitive Imaging in Tapping Mode by Chemical Force Microscopy: Relationship between Phase Lag and Adhesion. *Langmuir* **1998**, *14*, 1508–1511.

(23) Halas, N. J.; Lal, S.; Chang, W.-S.; Link, S.; Nordlander, P. Plasmons in Strongly Coupled Metallic Nanostructures. *Chem. Rev.* **2011**, *111*, 3913–3961.

(24) Hao, E.; Schatz, G. C. Electromagnetic Fields around Silver Nanoparticles and Dimers. *J. Chem. Phys.* **2004**, *120*, 357–366.

(25) McMahon, J. M.; Li, S.; Ausman, L. K.; Schatz, G. C. Modeling the Effect of Small Gaps in Surface-Enhanced Raman Spectroscopy. *J. Phys. Chem. C* **2012**, *116*, 1627–1637.

(26) Weaver, J. M. R.; Wickramasinghe, H. K. Semiconductor Characterization by Scanning Force Microscope Surface Photovoltage Microscopy. *J. Vac. Sci. Technol. B* **1991**, *9*, 1562–1565.

(27) Abe, M.; Uchihashi, T.; Ohta, M.; Ueyama, H.; Sugawara, Y.; Morita, S. Detection Mechanism of an Optical Evanescent Field Using a Noncontact Mode Atomic Force Microscope with a Frequency Modulation Detection Method. *J. Vac. Sci. Technol. B* **1997**, *15*, 1512–1515.

References

Chapter 1

(1) Willets, K. A.; Van Duyne, R. P. Localized Surface Plasmon Resonance Spectroscopy and Sensing. *Annu. Rev. Phys. Chem.* **2007**, *58*, 267–297.

(2) Haes, A. J.; Haynes, C. L.; McFarland, A. D.; Schatz, G. C.; Van Duyne, R. P.; Zou, S. Plasmonic Materials for Surface-Enhanced Sensing and Spectroscopy. *MRS Bull.* **2005**, *30*, 368–375.

(3) Halas, N. J.; Lal, S.; Chang, W.-S.; Link, S.; Nordlander, P. Plasmons in Strongly Coupled Metallic Nanostructures. *Chem. Rev.* **2011**, *111*, 3913–3961.

(4) Stiles, P. L.; Dieringer, J. A.; Shah, N. C.; Van Duyne, R. P. Surface-Enhanced Raman Spectroscopy. *Annu. Rev. Anal. Chem.* **2008**, *1*, 601–626.

(5) Hao, E.; Schatz, G. C. Electromagnetic Fields around Silver Nanoparticles and Dimers. *J. Chem. Phys.* **2004**, *120*, 357–366.

(6) Aroca, R. F. Plasmon Enhanced Spectroscopy. *Phys. Chem. Chem. Phys.* **2013**, *15*, 5355–5363.

(7) Ausman, L. K.; Schatz, G. C. On the Importance of Incorporating Dipole Reradiation in the Modeling of Surface Enhanced Raman Scattering from Spheres. *J. Chem. Phys.* **2009**, *131*, 084708–084708–10.

(8) McMahon, J. M.; Li, S.; Ausman, L. K.; Schatz, G. C. Modeling the Effect of Small Gaps in Surface-Enhanced Raman Spectroscopy. *J. Phys. Chem. C* **2012**, *116*, 1627–1637.

(9) Kerker, M.; Wang, D.-S.; Chew, H. Surface Enhanced Raman Scattering (SERS) by Molecules Adsorbed at Spherical Particles: Errata. *Appl. Opt.* **1980**, *19*, 4159–4174.

(10) Jain, P. K.; Huang, X.; El-Sayed, I. H.; El-Sayed, M. A. Noble Metals on the Nanoscale: Optical and Photothermal Properties and Some Applications in Imaging, Sensing, Biology, and Medicine. *Acc. Chem. Res.* **2008**, *41*, 1578–1586.

(11) Lal, S.; Clare, S. E.; Halas, N. J. Nanoshell-Enabled Photothermal Cancer Therapy: Impending Clinical Impact. *Acc. Chem. Res.* **2008**, *41*, 1842–1851.

(12) Golightly, R. S.; Doering, W. E.; Natan, M. J. Surface-Enhanced Raman Spectroscopy and Homeland Security: A Perfect Match? *ACS Nano* **2009**, *3*, 2859–2869.

(13) Stranahan, S. M.; Willets, K. A. Super-Resolution Optical Imaging of Single-Molecule SERS Hot Spots. *Nano Lett.* **2010**, *10*, 3777–3784.

(14) Dieringer, J. A.; Lettan, R. B.; Scheidt, K. A.; Van Duyne, R. P. A Frequency Domain Existence Proof of Single-Molecule Surface-Enhanced Raman Spectroscopy. *J. Am. Chem. Soc.* **2007**, *129*, 16249–16256.

(15) Le Ru, E. C.; Meyer, M.; Etchegoin, P. G. Proof of Single-Molecule Sensitivity in Surface Enhanced Raman Scattering (SERS) by Means of a Two-Analyte Technique. *J. Phys. Chem. B* **2006**, *110*, 1944–1948.

(16) Michaels, A. M.; Nirmal, M.; Brus, L. E. Surface Enhanced Raman Spectroscopy of Individual Rhodamine 6G Molecules on Large Ag Nanocrystals. *J. Am. Chem. Soc.* **1999**, *121*, 9932–9939.

(17) Kneipp, K.; Wang, Y.; Kneipp, H.; Perelman, L. T.; Itzkan, I.; Dasari, R. R.; Feld, M. S. Single Molecule Detection Using Surface-Enhanced Raman Scattering (SERS). *Phys. Rev. Lett.* **1997**, *78*, 1667–1670.

(18) Nie, S.; Emory, S. R. Probing Single Molecules and Single Nanoparticles by Surface-Enhanced Raman Scattering. *Science* **1997**, *275*, 1102–1106.

(19) Camden, J. P.; Dieringer, J. A.; Wang, Y.; Masiello, D. J.; Marks, L. D.; Schatz, G. C.; Van Duyne, R. P. Probing the Structure of Single-Molecule Surface-Enhanced Raman Scattering Hot Spots. *J. Am. Chem. Soc.* **2008**, *130*, 12616–12617.

(20) Wustholz, K. L.; Henry, A.-I.; McMahon, J. M.; Freeman, R. G.; Valley, N.; Piotti, M. E.; Natan, M. J.; Schatz, G. C.; Duyne, R. P. V. Structure−Activity Relationships in Gold Nanoparticle Dimers and Trimers for Surface-Enhanced Raman Spectroscopy. *J. Am. Chem. Soc.* **2010**, *132*, 10903–10910.

(21) Michaels, A. M.; Jiang; Brus, L. Ag Nanocrystal Junctions as the Site for Surface-Enhanced Raman Scattering of Single Rhodamine 6G Molecules. *J. Phys. Chem. B* **2000**, *104*, 11965–11971.

(22) Kleinman, S. L.; Ringe, E.; Valley, N.; Wustholz, K. L.; Phillips, E.; Scheidt, K. A.; Schatz, G. C.; Van Duyne, R. P. Single-Molecule Surface-Enhanced Raman Spectroscopy of Crystal Violet Isotopologues: Theory and Experiment. *J. Am. Chem. Soc.* **2011**, *133*, 4115–4122.

(23) Gordon, M. P.; Ha, T.; Selvin, P. R. Single-Molecule High-Resolution Imaging with Photobleaching. *Proc. Natl. Acad. Sci. U. S. A.* **2004**, *101*, 6462–6465.

(24) Wang, Y.; Fruhwirth, G.; Cai, E.; Ng, T.; Selvin, P. R. 3D Super-Resolution Imaging with Blinking Quantum Dots. *Nano Lett.* **2013**.

(25) Yildiz, A.; Forkey, J. N.; McKinney, S. A.; Ha, T.; Goldman, Y. E.; Selvin, P. R. Myosin V Walks Hand-Over-Hand: Single Fluorophore Imaging with 1.5-Nm Localization. *Science* **2003**, *300*, 2061–2065.

(26) Rust, M. J.; Bates, M.; Zhuang, X. Sub-Diffraction-Limit Imaging by Stochastic Optical Reconstruction Microscopy (STORM). *Nat. Methods* **2006**, *3*, 793–796.

(27) Betzig, E.; Patterson, G. H.; Sougrat, R.; Lindwasser, O. W.; Olenych, S.; Bonifacino, J. S.; Davidson, M. W.; Lippincott-Schwartz, J.; Hess, H. F. Imaging Intracellular Fluorescent Proteins at Nanometer Resolution. *Science* **2006**, *313*, 1642–1645.

(28) Sagle, L. B.; Ruvuna, L. K.; Bingham, J. M.; Liu, C.; Cremer, P. S.; Van Duyne, R. P. Single Plasmonic Nanoparticle Tracking Studies of Solid Supported Bilayers with Ganglioside Lipids. *J. Am. Chem. Soc.* **2012**, *134*, 15832–15839.

(29) Gu, Y.; Sun, W.; Wang, G.; Fang, N. Single Particle Orientation and Rotation Tracking Discloses Distinctive Rotational Dynamics of Drug Delivery Vectors on Live Cell Membranes. *J. Am. Chem. Soc.* **2011**, *133*, 5720–5723.

(30) Gu, Y.; Wang, G.; Fang, N. Simultaneous Single-Particle Superlocalization and Rotational Tracking. *ACS Nano* **2013**, *7*, 1658–1665.

(31) Gu, Y.; Di, X.; Sun, W.; Wang, G.; Fang, N. Three-Dimensional Super-Localization and Tracking of Single Gold Nanoparticles in Cells. *Anal. Chem.* **2012**, *84*, 4111–4117.

(32) Marchuk, K.; Ha, J. W.; Fang, N. Three-Dimensional High-Resolution Rotational Tracking with Superlocalization Reveals Conformations of Surface-Bound Anisotropic Nanoparticles. *Nano Lett.* **2013**, *13*, 1245–1250.

(33) Blythe, K. L.; Mayer, K. M.; Weber, M. L.; Willets, K. A. Ground State Depletion Microscopy for Imaging Interactions between Gold Nanowires and Fluorophore-Labeled Ligands. *Phys. Chem. Chem. Phys.* **2013**, *15*, 4136–4145.

(34) Lin, H.; Centeno, S. P.; Su, L.; Kenens, B.; Rocha, S.; Sliwa, M.; Hofkens, J.; Uji-i, H. Mapping of Surface-Enhanced Fluorescence on Metal Nanoparticles Using Super-Resolution Photoactivation Localization Microscopy. *ChemPhysChem* **2012**, *13*, 973–981.

(35) Zhou, X.; Andoy, N. M.; Liu, G.; Choudhary, E.; Han, K.-S.; Shen, H.; Chen, P. Quantitative Super-Resolution Imaging Uncovers Reactivity Patterns on Single Nanocatalysts. *Nat. Nanotechnol.* **2012**, *7*, 237–241.

(36) Weber, M. L.; Willets, K. A. Correlated Super-Resolution Optical and Structural Studies of Surface-Enhanced Raman Scattering Hot Spots in Silver Colloid Aggregates. *J. Phys. Chem. Lett.* **2011**, *2*, 1766–1770.

(37) Weber, M. L.; Litz, J. P.; Masiello, D. J.; Willets, K. A. Super-Resolution Imaging Reveals a Difference between SERS and Luminescence Centroids. *ACS Nano* **2012**, *6*, 1839–1848.

(38) Titus, E. J.; Weber, M. L.; Stranahan, S. M.; Willets, K. A. Super-Resolution SERS Imaging beyond the Single-Molecule Limit: An Isotope-Edited Approach. *Nano Lett.* **2012**, *12*, 5103–5110.

(39) Willets, K. A.; Stranahan, S. M.; Weber, M. L. Shedding Light on Surface-Enhanced Raman Scattering Hot Spots through Single-Molecule Super-Resolution Imaging. *J. Phys. Chem. Lett.* **2012**, *3*, 1286–1294.

(40) Shegai, T.; Li, Z.; Dadosh, T.; Zhang, Z.; Xu, H.; Haran, G. Managing Light Polarization via Plasmon–Molecule Interactions Within an Asymmetric Metal Nanoparticle Trimer. *Proc. Natl. Acad. Sci.* **2008**, *105*, 16448–16453.

(41) Li, Z.; Shegai, T.; Haran, G.; Xu, H. Multiple-Particle Nanoantennas for Enormous Enhancement and Polarization Control of Light Emission. *ACS Nano* **2009**, *3*, 637–642.

(42) Shegai, T.; Brian, B.; Miljković, V. D.; Käll, M. Angular Distribution of Surface-Enhanced Raman Scattering from Individual Au Nanoparticle Aggregates. *ACS Nano* **2011**, *5*, 2036–2041.

Chapter 2

(1) Lee, P. C.; Meisel, D. Adsorption and Surface-Enhanced Raman of Dyes on Silver and Gold Sols. *J. Phys. Chem.* **1982**, *86*, 3391–3395.

(2) Stranahan, S. M.; Willets, K. A. Super-Resolution Optical Imaging of Single-Molecule SERS Hot Spots. *Nano Lett.* **2010**, *10*, 3777–3784.

(3) Weber, M. L.; Willets, K. A. Correlated Super-Resolution Optical and Structural Studies of Surface-Enhanced Raman Scattering Hot Spots in Silver Colloid Aggregates. *J. Phys. Chem. Lett.* **2011**, *2*, 1766–1770.

(4) Shegai, T.; Brian, B.; Miljković, V. D.; Käll, M. Angular Distribution of Surface-Enhanced Raman Scattering from Individual Au Nanoparticle Aggregates. *ACS Nano* **2011**, *5*, 2036–2041.

(5) Ming, T.; Zhao, L.; Yang, Z.; Chen, H.; Sun, L.; Wang, J.; Yan, C. Strong Polarization Dependence of Plasmon-Enhanced Fluorescence on Single Gold Nanorods. *Nano Lett.* **2009**, *9*, 3896–3903.

(6) Mayer, K. M.; Lee, S.; Liao, H.; Rostro, B. C.; Fuentes, A.; Scully, P. T.; Nehl, C. L.; Hafner, J. H. A Label-Free Immunoassay Based Upon Localized Surface Plasmon Resonance of Gold Nanorods. *ACS Nano* **2008**, *2*, 687–692.

(7) Kaplan-Ashiri, I.; Titus, E. J.; Willets, K. A. Subdiffraction-Limited Far-Field Raman Spectroscopy of Single Carbon Nanotubes: An Unenhanced Approach. *ACS Nano* **2011**, *5*, 1033–1041.

(8) Stranahan, S. M.; Titus, E. J.; Willets, K. A. SERS Orientational Imaging of Silver Nanoparticle Dimers. *J. Phys. Chem. Lett.* **2011**, *2*, 2711–2715.

(9) Gordon, M. P.; Ha, T.; Selvin, P. R. Single-Molecule High-Resolution Imaging with Photobleaching. *Proc. Natl. Acad. Sci. U. S. A.* **2004**, *101*, 6462–6465.

(10) Thompson, R. E.; Larson, D. R.; Webb, W. W. Precise Nanometer Localization Analysis for Individual Fluorescent Probes. *Biophys. J.* **2002**, *82*, 2775–2783.

Chapter 3

(1) Camden, J. P.; Dieringer, J. A.; Wang, Y.; Masiello, D. J.; Marks, L. D.; Schatz, G. C.; Van Duyne, R. P. Probing the Structure of Single-Molecule Surface-

Enhanced Raman Scattering Hot Spots. *J. Am. Chem. Soc.* **2008**, *130*, 12616–12617.

(2) Qian, X.-M.; Nie, S. M. Single-Molecule and Single-Nanoparticle SERS: From Fundamental Mechanisms to Biomedical Applications. *Chem. Soc. Rev.* **2008**, *37*, 912–920.

(3) Dieringer, J. A.; Lettan, R. B.; Scheidt, K. A.; Van Duyne, R. P. A Frequency Domain Existence Proof of Single-Molecule Surface-Enhanced Raman Spectroscopy. *J. Am. Chem. Soc.* **2007**, *129*, 16249–16256.

(4) Michaels, A. M.; Jiang; Brus, L. Ag Nanocrystal Junctions as the Site for Surface-Enhanced Raman Scattering of Single Rhodamine 6G Molecules. *J. Phys. Chem. B* **2000**, *104*, 11965–11971.

(5) Stranahan, S. M.; Willets, K. A. Super-Resolution Optical Imaging of Single-Molecule SERS Hot Spots. *Nano Lett.* **2010**, *10*, 3777–3784.

(6) Cang, H.; Labno, A.; Lu, C.; Yin, X.; Liu, M.; Gladden, C.; Liu, Y.; Zhang, X. Probing the Electromagnetic Field of a 15-Nanometre Hotspot by Single Molecule Imaging. *Nature* **2011**, *469*, 385–388.

(7) Weber, M. L.; Litz, J. P.; Masiello, D. J.; Willets, K. A. Super-Resolution Imaging Reveals a Difference between SERS and Luminescence Centroids. *ACS Nano* **2012**, *6*, 1839–1848.

(8) Weber, M. L.; Willets, K. A. Correlated Super-Resolution Optical and Structural Studies of Surface-Enhanced Raman Scattering Hot Spots in Silver Colloid Aggregates. *J. Phys. Chem. Lett.* **2011**, *2*, 1766–1770.

(9) Willets, K. A.; Stranahan, S. M.; Weber, M. L. Shedding Light on Surface-Enhanced Raman Scattering Hot Spots through Single-Molecule Super-Resolution Imaging. *J. Phys. Chem. Lett.* **2012**, *3*, 1286–1294.

(10) Thompson, R. E.; Larson, D. R.; Webb, W. W. Precise Nanometer Localization Analysis for Individual Fluorescent Probes. *Biophys. J.* **2002**, *82*, 2775–2783.

(11) Kerker, M.; Wang, D.-S.; Chew, H. Surface Enhanced Raman Scattering (SERS) by Molecules Adsorbed at Spherical Particles: Errata. *Appl. Opt.* **1980**, *19*, 4159–4174.

(12) Ausman, L. K.; Schatz, G. C. On the Importance of Incorporating Dipole Reradiation in the Modeling of Surface Enhanced Raman Scattering from Spheres. *J. Chem. Phys.* **2009**, *131*, 084708–084708–10.

(13) Weiss, A.; Haran, G. Time-Dependent Single-Molecule Raman Scattering as a Probe of Surface Dynamics. *J. Phys. Chem. B* **2001**, *105*, 12348–12354.

(14) Lee, P. C.; Meisel, D. Adsorption and Surface-Enhanced Raman of Dyes on Silver and Gold Sols. *J. Phys. Chem.* **1982**, *86*, 3391–3395.

(15) Stranahan, S. M.; Titus, E. J.; Willets, K. A. Discriminating Nanoparticle Dimers from Higher Order Aggregates through Wavelength-Dependent SERS Orientational Imaging. *ACS Nano* **2012**, *6*, 1806–1813.

(16) Yildiz, A.; Forkey, J. N.; McKinney, S. A.; Ha, T.; Goldman, Y. E.; Selvin, P. R. Myosin V Walks Hand-Over-Hand: Single Fluorophore Imaging with 1.5-Nm Localization. *Science* **2003**, *300*, 2061–2065.

(17) Andersen, P. C.; Jacobson, M. L.; Rowlen, K. L. Flashy Silver Nanoparticles. *J. Phys. Chem. B* **2004**, *108*, 2148–2153.

(18) Gordon, M. P.; Ha, T.; Selvin, P. R. Single-Molecule High-Resolution Imaging with Photobleaching. *Proc. Natl. Acad. Sci. U. S. A.* **2004**, *101*, 6462–6465.

(19) Borys, N. J.; Lupton, J. M. Surface-Enhanced Light Emission from Single Hot Spots in Tollens Reaction Silver Nanoparticle Films: Linear versus Nonlinear Optical Excitation. *J. Phys. Chem. C* **2011**, *115*, 13645–13659.

(20) Li, Z.; Shegai, T.; Haran, G.; Xu, H. Multiple-Particle Nanoantennas for Enormous Enhancement and Polarization Control of Light Emission. *ACS Nano* **2009**, *3*, 637–642.

(21) Shegai, T.; Li, Z.; Dadosh, T.; Zhang, Z.; Xu, H.; Haran, G. Managing Light Polarization via Plasmon–Molecule Interactions Within an Asymmetric Metal Nanoparticle Trimer. *Proc. Natl. Acad. Sci.* **2008**, *105*, 16448–16453.

(22) Fromm, D. P.; Sundaramurthy, A.; Kinkhabwala, A.; Schuck, P. J.; Kino, G. S.; Moerner, W. E. Exploring the Chemical Enhancement for Surface-Enhanced Raman Scattering with Au Bowtie Nanoantennas. *J. Chem. Phys.* **2006**, *124*, 061101.

(23) Barhoumi, A.; Zhang, D.; Halas, N. J. Correlation of Molecular Orientation and Packing Density in a dsDNA Self-Assembled Monolayer Observable with Surface-Enhanced Raman Spectroscopy. *J. Am. Chem. Soc.* **2008**, *130*, 14040–14041.

(24) Moskovits, M.; Suh, J. S. Surface Selection Rules for Surface-Enhanced Raman Spectroscopy: Calculations and Application to the Surface-Enhanced Raman Spectrum of Phthalazine on Silver. *J. Phys. Chem.* **1984**, *88*, 5526–5530.

(25) Papadopoulou, E.; Bell, S. E. J. Surface-Enhanced Raman Evidence of Protonation, Reorientation, and Ag+ Complexation of Deoxyadenosine and Deoxyadenosine-5′-Monophosphate (dAMP) on Ag and Au Surfaces. *J. Phys. Chem. C* **2011**, *115*, 14228–14235.

(26) Wang, Z.; Rothberg, L. J. Origins of Blinking in Single-Molecule Raman Spectroscopy. *J. Phys. Chem. B* **2005**, *109*, 3387–3391.

(27) Creighton, J. A. Surface Raman Electromagnetic Enhancement Factors for Molecules at the Surface of Small Isolated Metal Spheres: The Determination of

Adsorbate Orientation from Sers Relative Intensities. *Surf. Sci.* **1983**, *124*, 209–219.

(28) Rust, M. J.; Bates, M.; Zhuang, X. Sub-Diffraction-Limit Imaging by Stochastic Optical Reconstruction Microscopy (STORM). *Nat. Methods* **2006**, *3*, 793–796.

(29) Betzig, E.; Patterson, G. H.; Sougrat, R.; Lindwasser, O. W.; Olenych, S.; Bonifacino, J. S.; Davidson, M. W.; Lippincott-Schwartz, J.; Hess, H. F. Imaging Intracellular Fluorescent Proteins at Nanometer Resolution. *Science* **2006**, *313*, 1642–1645.

(30) Hallock, A. J.; Redmond, P. L.; Brus, L. E. Optical Forces between Metallic Particles. *Proc. Natl. Acad. Sci. U. S. A.* **2005**, *102*, 1280–1284.

(31) Xu, H.; Käll, M. Surface-Plasmon-Enhanced Optical Forces in Silver Nanoaggregates. *Phys. Rev. Lett.* **2002**, *89*, 246802.

(32) Mortensen, K. I.; Churchman, L. S.; Spudich, J. A.; Flyvbjerg, H. Optimized Localization Analysis for Single-Molecule Tracking and Super-Resolution Microscopy. *Nat. Methods* **2010**, *7*, 377–381.

(33) Stranahan, S. M.; Titus, E. J.; Willets, K. A. SERS Orientational Imaging of Silver Nanoparticle Dimers. *J. Phys. Chem. Lett.* **2011**, *2*, 2711–2715.

Chapter 4

(1) Stranahan, S. M.; Titus, E. J.; Willets, K. A. SERS Orientational Imaging of Silver Nanoparticle Dimers. *J. Phys. Chem. Lett.* **2011**, *2*, 2711–2715.

(2) Stranahan, S. M.; Titus, E. J.; Willets, K. A. Discriminating Nanoparticle Dimers from Higher Order Aggregates through Wavelength-Dependent SERS Orientational Imaging. *ACS Nano* **2012**, *6*, 1806–1813.

(3) Shegai, T.; Brian, B.; Miljković, V. D.; Käll, M. Angular Distribution of Surface-Enhanced Raman Scattering from Individual Au Nanoparticle Aggregates. *ACS Nano* **2011**, *5*, 2036–2041.

(4) Li, Z.; Shegai, T.; Haran, G.; Xu, H. Multiple-Particle Nanoantennas for Enormous Enhancement and Polarization Control of Light Emission. *ACS Nano* **2009**, *3*, 637–642.

(5) Bartko, A. P.; Dickson, R. M. Three-Dimensional Orientations of Polymer-Bound Single Molecules. *J. Phys. Chem. B* **1999**, *103*, 3053–3056.

(6) Bartko, A. P.; Dickson, R. M. Imaging Three-Dimensional Single Molecule Orientations. *J. Phys. Chem. B* **1999**, *103*, 11237–11241.

(7) Hellen, E. H.; Axelrod, D. Fluorescence Emission at Dielectric and Metal-Film Interfaces. *J. Opt. Soc. Am. B* **1987**, *4*, 337–350.

(8) Dickson, R. M.; Norris, D. J.; Moerner, W. E. Simultaneous Imaging of Individual Molecules Aligned Both Parallel and Perpendicular to the Optic Axis. *Phys. Rev. Lett.* **1998**, *81*, 5322–5325.

(9) Böhmer, M.; Enderlein, J. Orientation Imaging of Single Molecules by Wide-Field Epifluorescence Microscopy. *J. Opt. Soc. Am. B* **2003**, *20*, 554–559.

(10) Lieb, M. A.; Zavislan, J. M.; Novotny, L. Single-Molecule Orientations Determined by Direct Emission Pattern Imaging. *J. Opt. Soc. Am. B* **2004**, *21*, 1210–1215.

(11) Enderlein, J.; Toprak, E.; Selvin, P. R. Polarization Effect on Position Accuracy of Fluorophore Localization. *Opt. Express* **2006**, *14*, 8111–8120.

(12) Lew, M. D.; Backlund, M. P.; Moerner, W. E. Rotational Mobility of Single Molecules Affects Localization Accuracy in Super-Resolution Fluorescence Microscopy. *Nano Lett.* **2013**.

(13) Mortensen, K. I.; Churchman, L. S.; Spudich, J. A.; Flyvbjerg, H. Optimized Localization Analysis for Single-Molecule Tracking and Super-Resolution Microscopy. *Nat. Methods* **2010**, *7*, 377–381.

(14) Engelhardt, J.; Keller, J.; Hoyer, P.; Reuss, M.; Staudt, T.; Hell, S. W. Molecular Orientation Affects Localization Accuracy in Superresolution Far-Field Fluorescence Microscopy. *Nano Lett.* **2011**, *11*, 209–213.

(15) Fang, Y.; Chang, W.-S.; Willingham, B.; Swanglap, P.; Dominguez-Medina, S.; Link, S. Plasmon Emission Quantum Yield of Single Gold Nanorods as a Function of Aspect Ratio. *ACS Nano* **2012**, *6*, 7177–7184.

(16) Tcherniak, A.; Dominguez-Medina, S.; Chang, W.-S.; Swanglap, P.; Slaughter, L. S.; Landes, C. F.; Link, S. One-Photon Plasmon Luminescence and Its Application to Correlation Spectroscopy as a Probe for Rotational and Translational Dynamics of Gold Nanorods. *J. Phys. Chem. C* **2011**, *115*, 15938–15949.

(17) Yorulmaz, M.; Khatua, S.; Zijlstra, P.; Gaiduk, A.; Orrit, M. Luminescence Quantum Yield of Single Gold Nanorods. *Nano Lett.* **2012**, *12*, 4385–4391.

(18) Ausman, L. K.; Schatz, G. C. On the Importance of Incorporating Dipole Reradiation in the Modeling of Surface Enhanced Raman Scattering from Spheres. *J. Chem. Phys.* **2009**, *131*, 084708–084708–10.

(19) Shegai, T.; Li, Z.; Dadosh, T.; Zhang, Z.; Xu, H.; Haran, G. Managing Light Polarization via Plasmon–Molecule Interactions Within an Asymmetric Metal Nanoparticle Trimer. *Proc. Natl. Acad. Sci.* **2008**, *105*, 16448–16453.

(20) Xiao, L.; Qiao, Y.; He, Y.; Yeung, E. S. Three Dimensional Orientational Imaging of Nanoparticles with Darkfield Microscopy. *Anal. Chem.* **2010**, *82*, 5268–5274.

(21) Stranahan, S. M.; Willets, K. A. Super-Resolution Optical Imaging of Single-Molecule SERS Hot Spots. *Nano Lett.* **2010**, *10*, 3777–3784.

(22) Weber, M. L.; Willets, K. A. Correlated Super-Resolution Optical and Structural Studies of Surface-Enhanced Raman Scattering Hot Spots in Silver Colloid Aggregates. *J. Phys. Chem. Lett.* **2011**, *2*, 1766–1770.

(23) Weber, M. L.; Litz, J. P.; Masiello, D. J.; Willets, K. A. Super-Resolution Imaging Reveals a Difference between SERS and Luminescence Centroids. *ACS Nano* **2012**, *6*, 1839–1848.

(24) Motegi, T.; Nabika, H.; Niidome, Y.; Murakoshi, K. Observation of Defocus Images of a Single Metal Nanorod. *J. Phys. Chem. C* **2013**, *117*, 2535–2540.

(25) Ha, J. W.; Marchuk, K.; Fang, N. Focused Orientation and Position Imaging (FOPI) of Single Anisotropic Plasmonic Nanoparticles by Total Internal Reflection Scattering Microscopy. *Nano Lett.* **2012**, *12*, 4282–4288.

(26) Li, T.; Li, Q.; Xu, Y.; Chen, X.-J.; Dai, Q.-F.; Liu, H.; Lan, S.; Tie, S.; Wu, L.-J. Three-Dimensional Orientation Sensors by Defocused Imaging of Gold Nanorods through an Ordinary Wide-Field Microscope. *ACS Nano* **2012**, *6*, 1268–1277.

(27) Wackenhut, F.; Virgilio Failla, A.; Züchner, T.; Steiner, M.; Meixner, A. J. Three-Dimensional Photoluminescence Mapping and Emission Anisotropy of Single Gold Nanorods. *Appl. Phys. Lett.* **2012**, *100*, 263102–263102–4.

(28) Blythe, K. L.; Mayer, K. M.; Weber, M. L.; Willets, K. A. Ground State Depletion Microscopy for Imaging Interactions between Gold Nanowires and Fluorophore-Labeled Ligands. *Phys. Chem. Chem. Phys.* **2013**, *15*, 4136–4145.

(29) Lin, H.; Centeno, S. P.; Su, L.; Kenens, B.; Rocha, S.; Sliwa, M.; Hofkens, J.; Uji-i, H. Mapping of Surface-Enhanced Fluorescence on Metal Nanoparticles Using Super-Resolution Photoactivation Localization Microscopy. *ChemPhysChem* **2012**, *13*, 973–981.

(30) Zhou, X.; Andoy, N. M.; Liu, G.; Choudhary, E.; Han, K.-S.; Shen, H.; Chen, P. Quantitative Super-Resolution Imaging Uncovers Reactivity Patterns on Single Nanocatalysts. *Nat. Nanotechnol.* **2012**, *7*, 237–241.

(31) Cang, H.; Labno, A.; Lu, C.; Yin, X.; Liu, M.; Gladden, C.; Liu, Y.; Zhang, X. Probing the Electromagnetic Field of a 15-Nanometre Hotspot by Single Molecule Imaging. *Nature* **2011**, *469*, 385–388.

(32) Titus, E. J.; Weber, M. L.; Stranahan, S. M.; Willets, K. A. Super-Resolution SERS Imaging beyond the Single-Molecule Limit: An Isotope-Edited Approach. *Nano Lett.* **2012**, *12*, 5103–5110.

(33) Enderlein, J. Imaging of Single Molecules http://www.joerg-enderlein.de/imagingOfSingleMolecules.html (accessed May 3, 2013).

(34) Patra, D.; Gregor, I.; Enderlein, J.; Sauer, M. Defocused Imaging of Quantum-Dot Angular Distribution of Radiation. *Appl. Phys. Lett.* **2005**, *87*, 101103–101103–3.

(35) Patra, D.; Gregor, I.; Enderlein, J. Image Analysis of Defocused Single-Molecule Images for Three-Dimensional Molecule Orientation Studies. *J. Phys. Chem. A* **2004**, *108*, 6836–6841.

(36) Dulkeith, E.; Niedereichholz, T.; Klar, T. A.; Feldmann, J.; von Plessen, G.; Gittins, D. I.; Mayya, K. S.; Caruso, F. Plasmon Emission in Photoexcited Gold Nanoparticles. *Phys. Rev. B* **2004**, *70*, 205424.

(37) Varnavski, O. P.; Goodson, T.; Mohamed, M. B.; El-Sayed, M. A. Femtosecond Excitation Dynamics in Gold Nanospheres and Nanorods. *Phys. Rev. B* **2005**, *72*, 235405.

Chapter 5

(1) Titus, E. J.; Willets, K. A. Accuracy of Superlocalization Imaging Using Gaussian and Dipole Emission Point-Spread Functions for Modeling Gold Nanorod Luminescence. *ACS Nano* **2013**, *7*, 6258–6267.

(2) Fang, Y.; Chang, W.-S.; Willingham, B.; Swanglap, P.; Dominguez-Medina, S.; Link, S. Plasmon Emission Quantum Yield of Single Gold Nanorods as a Function of Aspect Ratio. *ACS Nano* **2012**, *6*, 7177–7184.

(3) Yorulmaz, M.; Khatua, S.; Zijlstra, P.; Gaiduk, A.; Orrit, M. Luminescence Quantum Yield of Single Gold Nanorods. *Nano Lett.* **2012**, *12*, 4385–4391.

(4) Li, Z.; Shegai, T.; Haran, G.; Xu, H. Multiple-Particle Nanoantennas for Enormous Enhancement and Polarization Control of Light Emission. *ACS Nano* **2009**, *3*, 637–642.

(5) Shegai, T.; Li, Z.; Dadosh, T.; Zhang, Z.; Xu, H.; Haran, G. Managing Light Polarization via Plasmon–Molecule Interactions Within an Asymmetric Metal Nanoparticle Trimer. *Proc. Natl. Acad. Sci.* **2008**, *105*, 16448–16453.

(6) Stranahan, S. M.; Titus, E. J.; Willets, K. A. SERS Orientational Imaging of Silver Nanoparticle Dimers. *J. Phys. Chem. Lett.* **2011**, *2*, 2711–2715.

(7) Shegai, T.; Brian, B.; Miljković, V. D.; Käll, M. Angular Distribution of Surface-Enhanced Raman Scattering from Individual Au Nanoparticle Aggregates. *ACS Nano* **2011**, *5*, 2036–2041.

(8) Ausman, L. K.; Schatz, G. C. On the Importance of Incorporating Dipole Reradiation in the Modeling of Surface Enhanced Raman Scattering from Spheres. *J. Chem. Phys.* **2009**, *131*, 084708–084708–10.

(9) Stranahan, S. M.; Willets, K. A. Super-Resolution Optical Imaging of Single-Molecule SERS Hot Spots. *Nano Lett.* **2010**, *10*, 3777–3784.

(10) Titus, E. J.; Weber, M. L.; Stranahan, S. M.; Willets, K. A. Super-Resolution SERS Imaging beyond the Single-Molecule Limit: An Isotope-Edited Approach. *Nano Lett.* **2012**, *12*, 5103–5110.

(11) Weber, M. L.; Willets, K. A. Correlated Super-Resolution Optical and Structural Studies of Surface-Enhanced Raman Scattering Hot Spots in Silver Colloid Aggregates. *J. Phys. Chem. Lett.* **2011**, *2*, 1766–1770.

(12) Enderlein, J. Imaging of Single Molecules http://www.joerg-enderlein.de/imagingOfSingleMolecules.html (accessed May 3, 2013).

(13) Dieringer, J. A.; Lettan, R. B.; Scheidt, K. A.; Van Duyne, R. P. A Frequency Domain Existence Proof of Single-Molecule Surface-Enhanced Raman Spectroscopy. *J. Am. Chem. Soc.* **2007**, *129*, 16249–16256.

(14) Nie, S.; Emory, S. R. Probing Single Molecules and Single Nanoparticles by Surface-Enhanced Raman Scattering. *Science* **1997**, *275*, 1102–1106.

(15) Bartko, A. P.; Dickson, R. M. Three-Dimensional Orientations of Polymer-Bound Single Molecules. *J. Phys. Chem. B* **1999**, *103*, 3053–3056.

(16) Bartko, A. P.; Dickson, R. M. Imaging Three-Dimensional Single Molecule Orientations. *J. Phys. Chem. B* **1999**, *103*, 11237–11241.

(17) Hellen, E. H.; Axelrod, D. Fluorescence Emission at Dielectric and Metal-Film Interfaces. *J. Opt. Soc. Am. B* **1987**, *4*, 337–350.

(18) Hao, E.; Schatz, G. C. Electromagnetic Fields around Silver Nanoparticles and Dimers. *J. Chem. Phys.* **2004**, *120*, 357–366.

(19) Halas, N. J.; Lal, S.; Chang, W.-S.; Link, S.; Nordlander, P. Plasmons in Strongly Coupled Metallic Nanostructures. *Chem. Rev.* **2011**, *111*, 3913–3961.

(20) Enderlein, J.; Toprak, E.; Selvin, P. R. Polarization Effect on Position Accuracy of Fluorophore Localization. *Opt. Express* **2006**, *14*, 8111–8120.

(21) Engelhardt, J.; Keller, J.; Hoyer, P.; Reuss, M.; Staudt, T.; Hell, S. W. Molecular Orientation Affects Localization Accuracy in Superresolution Far-Field Fluorescence Microscopy. *Nano Lett.* **2011**, *11*, 209–213.

(22) Lew, M. D.; Backlund, M. P.; Moerner, W. E. Rotational Mobility of Single Molecules Affects Localization Accuracy in Super-Resolution Fluorescence Microscopy. *Nano Lett.* **2013**.

(23) Stranahan, S. M.; Titus, E. J.; Willets, K. A. Discriminating Nanoparticle Dimers from Higher Order Aggregates through Wavelength-Dependent SERS Orientational Imaging. *ACS Nano* **2012**, *6*, 1806–1813.

(24) Weber, M. L.; Litz, J. P.; Masiello, D. J.; Willets, K. A. Super-Resolution Imaging Reveals a Difference between SERS and Luminescence Centroids. *ACS Nano* **2012**, *6*, 1839–1848.

(25) Oubre, C.; Nordlander, P. Optical Properties of Metallodielectric Nanostructures Calculated Using the Finite Difference Time Domain Method. *J. Phys. Chem. B* **2004**, *108*, 17740–17747.

Chapter 6

(1) Alonso-Gonzalez, P.; Schnell, M.; Sarriugarte, P.; Sobhani, H.; Wu, C.; Arju, N.; Khanikaev, A.; Golmar, F.; Albella, P.; Arzubiaga, L.; *et al.* Real-Space Mapping of Fano Interference in Plasmonic Metamolecules. *Nano Lett.* **2011**, *11*, 3922–3926.

(2) Hillenbrand, R.; Keilmann, F.; Hanarp, P.; Sutherland, D. S.; Aizpurua, J. Coherent Imaging of Nanoscale Plasmon Patterns with a Carbon Nanotube Optical Probe. *Appl. Phys. Lett.* **2003**, *83*, 368–370.

(3) Rang, M.; Jones, A. C.; Zhou, F.; Li, Z.-Y.; Wiley, B. J.; Xia, Y.; Raschke, M. B. Optical Near-Field Mapping of Plasmonic Nanoprisms. *Nano Lett.* **2008**, *8*, 3357–3363.

(4) Michaels, A. M.; Jiang; Brus, L. Ag Nanocrystal Junctions as the Site for Surface-Enhanced Raman Scattering of Single Rhodamine 6G Molecules. *J. Phys. Chem. B* **2000**, *104*, 11965–11971.

(5) Stranahan, S. M.; Titus, E. J.; Willets, K. A. SERS Orientational Imaging of Silver Nanoparticle Dimers. *J. Phys. Chem. Lett.* **2011**, *2*, 2711–2715.

(6) Weber, M. L.; Willets, K. A. Correlated Super-Resolution Optical and Structural Studies of Surface-Enhanced Raman Scattering Hot Spots in Silver Colloid Aggregates. *J. Phys. Chem. Lett.* **2011**, *2*, 1766–1770.

(7) Camden, J. P.; Dieringer, J. A.; Wang, Y.; Masiello, D. J.; Marks, L. D.; Schatz, G. C.; Van Duyne, R. P. Probing the Structure of Single-Molecule Surface-Enhanced Raman Scattering Hot Spots. *J. Am. Chem. Soc.* **2008**, *130*, 12616–12617.

(8) Peica, N.; Thomsen, C.; Maultzsch, J. Tip-Enhanced Raman Scattering along a Single Wall Carbon Nanotubes Bundle. *Phys. Status Solidi B* **2010**, *247*, 2818–2822.

(9) Yano, T.; Verma, P.; Saito, Y.; Ichimura, T.; Kawata, S. Pressure-Assisted Tip-Enhanced Raman Imaging at a Resolution of a Few Nanometres. *Nat. Photonics* **2009**, *3*, 473–477.

(10) Woolley, A. T.; Cheung, C. L.; Hafner, J. H.; Lieber, C. M. Structural Biology with Carbon Nanotube AFM Probes. *Chem. Biol.* **2000**, *7*, R193–R204.

(11) Wade, L. A.; Shapiro, I. R.; Ma, Z.; Quake, S. R.; Collier, C. P. Correlating AFM Probe Morphology to Image Resolution for Single-Wall Carbon Nanotube Tips. *Nano Lett.* **2004**, *4*, 725–731.

(12) Wilson, N. R.; Macpherson, J. V. Carbon Nanotube Tips for Atomic Force Microscopy. *Nat. Nanotechnol.* **2009**, *4*, 483–491.

(13) Kaplan-Ashiri, I.; Titus, E. J.; Willets, K. A. In Situ Chemical Functionalization of a Single Carbon Nanotube Functionalized AFM Tip Using a Correlated Optical and Atomic Force Microscope. *MRS Online Proc. Libr.* **2011**, *1318*, null–null.

(14) Yu, M.-F.; Lourie, O.; Dyer, M. J.; Moloni, K.; Kelly, T. F.; Ruoff, R. S. Strength and Breaking Mechanism of Multiwalled Carbon Nanotubes Under Tensile Load. *Science* **2000**, *287*, 637–640.

(15) Stiles, R. L.; Willets, K. A.; Sherry, L. J.; Roden, J. M.; Van Duyne, R. P. Investigating Tip−Nanoparticle Interactions in Spatially Correlated Total Internal Reflection Plasmon Spectroscopy and Atomic Force Microscopy. *J. Phys. Chem. C* **2008**, *112*, 11696–11701.

(16) Axelrod, D.; Burghardt, T. P.; Thompson, N. L. Total Internal Reflection Fluorescence. *Annu. Rev. Biophys. Bioeng.* **1984**, *13*, 247–268.

(17) McKee, K. J.; Smith, E. A. Development of a Scanning Angle Total Internal Reflection Raman Spectrometer. *Rev. Sci. Instrum.* **2010**, *81*, 043106.

(18) Mattheyses, A. L.; Axelrod, D. Direct Measurement of the Evanescent Field Profile Produced by Objective-Based Total Internal Reflection Fluorescence. *J. Biomed. Opt.* **2006**, *11*, 014006–014006–7.

(19) Dresselhaus, M. S.; Dresselhaus, G.; Saito, R.; Jorio, A. Raman Spectroscopy of Carbon Nanotubes. *Phys. Rep.* **2005**, *409*, 47–99.

(20) Dresselhaus, M. S. NT10: Recent Advances in Carbon Nanotube Science and Applications. *ACS Nano* **2010**, *4*, 4344–4349.

(21) Dresselhaus, M. S.; Jorio, A.; Hofmann, M.; Dresselhaus, G.; Saito, R. Perspectives on Carbon Nanotubes and Graphene Raman Spectroscopy. *Nano Lett.* **2010**, *10*, 751–758.

(22) Jorio, A.; Pimenta, M. A.; Filho, A. G. S.; Saito, R.; Dresselhaus, G.; Dresselhaus, M. S. Characterizing Carbon Nanotube Samples with Resonance Raman Scattering. *New J. Phys.* **2003**, *5*, 139.

(23) Maejima, K.; Suzuki, O.; Uchida, T.; Aoki, N.; Tachibana, M.; Ishibashi, K.; Ochiai, Y. Raman and Transport Studies in Multi-Walled Carbon Nanotubes. *J. Phys. Conf. Ser.* **2006**, *38*, 33.

(24) Minati, L.; Speranza, G.; Bernagozzi, I.; Torrengo, S.; Toniutti, L.; Rossi, B.; Ferrari, M.; Chiasera, A. Investigation on the Electronic and Optical Properties of Short Oxidized Multiwalled Carbon Nanotubes. *J. Phys. Chem. C* **2010**, *114*, 11068–11073.

(25) Hao, E.; Schatz, G. C. Electromagnetic Fields around Silver Nanoparticles and Dimers. *J. Chem. Phys.* **2004**, *120*, 357–366.

(26) Halas, N. J.; Lal, S.; Chang, W.-S.; Link, S.; Nordlander, P. Plasmons in Strongly Coupled Metallic Nanostructures. *Chem. Rev.* **2011**, *111*, 3913–3961.

(27) Duesberg, G. S.; Loa, I.; Burghard, M.; Syassen, K.; Roth, S. Polarized Raman Spectroscopy on Isolated Single-Wall Carbon Nanotubes. *Phys. Rev. Lett.* **2000**, *85*, 5436–5439.

(28) Garcia, R.; Martinez, R. V.; Martinez, J. Nano-Chemistry and Scanning Probe Nanolithographies. *Chem. Soc. Rev.* **2006**, *35*, 29–38.

(29) Stranahan, S. M.; Willets, K. A. Super-Resolution Optical Imaging of Single-Molecule SERS Hot Spots. *Nano Lett.* **2010**, *10*, 3777–3784.

(30) Kneipp, K.; Wang, Y.; Kneipp, H.; Perelman, L. T.; Itzkan, I.; Dasari, R. R.; Feld, M. S. Single Molecule Detection Using Surface-Enhanced Raman Scattering (SERS). *Phys. Rev. Lett.* **1997**, *78*, 1667–1670.

(31) Pieczonka, N. P. W.; Aroca, R. F. Inherent Complexities of Trace Detection by Surface-Enhanced Raman Scattering. *ChemPhysChem* **2005**, *6*, 2473–2484.

(32) Link, S.; Burda, C.; Nikoobakht, B.; El-Sayed, M. A. How Long Does It Take to Melt a Gold Nanorod?: A Femtosecond Pump–probe Absorption Spectroscopic Study. *Chem. Phys. Lett.* **1999**, *315*, 12–18.

Appendix 1

(1) Bartko, A. P.; Dickson, R. M. Imaging Three-Dimensional Single Molecule Orientations. *J. Phys. Chem. B* **1999**, *103*, 11237–11241.

(2) Bartko, A. P.; Dickson, R. M. Three-Dimensional Orientations of Polymer-Bound Single Molecules. *J. Phys. Chem. B* **1999**, *103*, 3053–3056.

(3) Hellen, E. H.; Axelrod, D. Fluorescence Emission at Dielectric and Metal-Film Interfaces. *J. Opt. Soc. Am. B* **1987**, *4*, 337–350.

(4) Dickson, R. M.; Norris, D. J.; Moerner, W. E. Simultaneous Imaging of Individual Molecules Aligned Both Parallel and Perpendicular to the Optic Axis. *Phys. Rev. Lett.* **1998**, *81*, 5322–5325.

(5) Enderlein, J.; Toprak, E.; Selvin, P. R. Polarization Effect on Position Accuracy of Fluorophore Localization. *Opt. Express* **2006**, *14*, 8111–8120.

(6) Enderlein, J. Imaging of Single Molecules http://www.joerg-enderlein.de/imagingOfSingleMolecules.html (accessed May 3, 2013).

(7) Patra, D.; Gregor, I.; Enderlein, J.; Sauer, M. Defocused Imaging of Quantum-Dot Angular Distribution of Radiation. *Appl. Phys. Lett.* **2005**, *87*, 101103–101103–3.

(8) Stranahan, S. M.; Titus, E. J.; Willets, K. A. SERS Orientational Imaging of Silver Nanoparticle Dimers. *J. Phys. Chem. Lett.* **2011**, *2*, 2711–2715.

Appendix 2

(1) Svoboda, K.; Block, S. M. Biological Applications of Optical Forces. *Annu. Rev. Biophys. Biomol. Struct.* **1994**, *23*, 247–285.

(2) Dholakia, K.; Reece, P.; Gu, M. Optical Micromanipulation. *Chem. Soc. Rev.* **2007**, *37*, 42–55.

(3) Righini, M.; Girard, C.; Quidant, R. Light-Induced Manipulation with Surface Plasmons. *J. Opt. Pure Appl. Opt.* **2008**, *10*, 093001.

(4) Gelfand, R. M.; Bruderer, L.; Mohseni, H. Nanocavity Plasmonic Device for Ultrabroadband Single Molecule Sensing. *Opt. Lett.* **2009**, *34*, 1087.

(5) Berthelot, J.; Aćimović, S. S.; Juan, M. L.; Kreuzer, M. P.; Renger, J.; Quidant, R. Three-Dimensional Manipulation with Scanning near-Field Optical Nanotweezers. *Nat. Nanotechnol.* **2014**, *9*, 295–299.

(6) Righini, M.; Volpe, G.; Girard, C.; Petrov, D.; Quidant, R. Surface Plasmon Optical Tweezers: Tunable Optical Manipulation in the Femtonewton Range. *Phys. Rev. Lett.* **2008**, *100*, 186804.

(7) Juan, M. L.; Righini, M.; Quidant, R. Plasmon Nano-Optical Tweezers. *Nat. Photonics* **2011**, *5*, 349–356.

(8) Righini, M.; Ghenuche, P.; Cherukulappurath, S.; Myroshnychenko, V.; García de Abajo, F. J.; Quidant, R. Nano-Optical Trapping of Rayleigh Particles and Escherichia Coli Bacteria with Resonant Optical Antennas. *Nano Lett.* **2009**, *9*, 3387–3391.

(9) Huang, L.; Maerkl, S. J.; Martin, O. J. Integration of Plasmonic Trapping in a Microfluidic Environment. *Opt. Express* **2009**, *17*, 6018–6024.

(10) Xu, H.; Käll, M. Surface-Plasmon-Enhanced Optical Forces in Silver Nanoaggregates. *Phys. Rev. Lett.* **2002**, *89*, 246802.

(11) Miljković, V. D.; Pakizeh, T.; Sepulveda, B.; Johansson, P.; Käll, M. Optical Forces in Plasmonic Nanoparticle Dimers†. *J. Phys. Chem. C* **2010**, *114*, 7472–7479.

(12) Stranahan, S. M.; Willets, K. A. Super-Resolution Optical Imaging of Single-Molecule SERS Hot Spots. *Nano Lett.* **2010**, *10*, 3777–3784.

(13) Knöner, G.; Ratnapala, A.; Nieminen, T. A.; Vale, C. J.; Heckenberg, N. R.; Rubinsztein-Dunlop, H. Optical Force Field Mapping in Microdevices. *Lab. Chip* **2006**, *6*, 1545–1547.

(14) Volpe, G.; Quidant, R.; Badenes, G.; Petrov, D. Surface Plasmon Radiation Forces. *Phys. Rev. Lett.* **2006**, *96*, 238101.

(15) Kohoutek, J.; Dey, D.; Bonakdar, A.; Gelfand, R.; Sklar, A.; Memis, O. G.; Mohseni, H. Opto-Mechanical Force Mapping of Deep Subwavelength Plasmonic Modes. *Nano Lett.* **2011**, *11*, 3378–3382.

(16) Axelrod, D.; Burghardt, T. P.; Thompson, N. L. Total Internal Reflection Fluorescence. *Annu. Rev. Biophys. Bioeng.* **1984**, *13*, 247–268.

(17) McKee, K. J.; Smith, E. A. Development of a Scanning Angle Total Internal Reflection Raman Spectrometer. *Rev. Sci. Instrum.* **2010**, *81*, 043106.

(18) Garcia, R.; Martinez, R. V.; Martinez, J. Nano-Chemistry and Scanning Probe Nanolithographies. *Chem. Soc. Rev.* **2006**, *35*, 29–38.

(19) Rajapaksa, I.; Uenal, K.; Wickramasinghe, H. K. Image Force Microscopy of Molecular Resonance: A Microscope Principle. *Appl. Phys. Lett.* **2010**, *97*, 073121.

(20) Rajapaksa, I.; Wickramasinghe, H. K. Raman Spectroscopy and Microscopy Based on Mechanical Force Detection. *Appl. Phys. Lett.* **2011**, *99*, 161103.

(21) Garcia, R.; Herruzo, E. T. The Emergence of Multifrequency Force Microscopy. *Nat. Nanotechnol.* **2012**, *7*, 217–226.

(22) Noy, A.; Sanders, C. H.; Vezenov, D. V.; Wong, S. S.; Lieber, C. M. Chemically-Sensitive Imaging in Tapping Mode by Chemical Force Microscopy: Relationship between Phase Lag and Adhesion. *Langmuir* **1998**, *14*, 1508–1511.

(23) Halas, N. J.; Lal, S.; Chang, W.-S.; Link, S.; Nordlander, P. Plasmons in Strongly Coupled Metallic Nanostructures. *Chem. Rev.* **2011**, *111*, 3913–3961.

(24) Hao, E.; Schatz, G. C. Electromagnetic Fields around Silver Nanoparticles and Dimers. *J. Chem. Phys.* **2004**, *120*, 357–366.

(25) McMahon, J. M.; Li, S.; Ausman, L. K.; Schatz, G. C. Modeling the Effect of Small Gaps in Surface-Enhanced Raman Spectroscopy. *J. Phys. Chem. C* **2012**, *116*, 1627–1637.

(26) Weaver, J. M. R.; Wickramasinghe, H. K. Semiconductor Characterization by Scanning Force Microscope Surface Photovoltage Microscopy. *J. Vac. Sci. Technol. B* **1991**, *9*, 1562–1565.

(27) Abe, M.; Uchihashi, T.; Ohta, M.; Ueyama, H.; Sugawara, Y.; Morita, S. Detection Mechanism of an Optical Evanescent Field Using a Noncontact Mode Atomic Force Microscope with a Frequency Modulation Detection Method. *J. Vac. Sci. Technol. B* **1997**, *15*, 1512–1515.